SPATIALLY RESOLVED STUDY OF THE MOLECULAR ISOTOPOLOGUE ^{13}CO IN NEARBY GALAXIES

BY

YIXIAN CAO

DISSERTATION

Submitted in partial fulfillment of the requirements
for the degree of Doctor of Philosophy in Astronomy
in the Graduate College of the
University of Illinois at Urbana-Champaign, 2018

Urbana, Illinois

Doctoral Committee:

Professor Tony Wong, Chair
Professor Leslie W. Looney
Professor Athol J. Kemball
Assistant Professor Xin Liu

Abstract

Observations of ^{13}CO are indispensable for probing physical conditions in the molecular interstellar medium (ISM) where the most commonly used ^{12}CO emission often saturates, at the cost of weaker emission that is difficult to observe. The line intensity ratio $^{12}\mathrm{CO}(J = 1 \rightarrow 0)/\ ^{13}\mathrm{CO}(J = 1 \rightarrow 0)$ (hereafter $\mathcal{R}$) can be used to trace variations in optical depths determined by the physical conditions, although it can also be influenced by chemical processes. In this thesis, I investigate the ^{13}CO emission and the line ratio $\mathcal{R}$ on kiloparsec (kpc) scales for a wide variety of galaxies: 11 galaxies from the CARMA STING survey and 42 galaxies from the CARMA EDGE survey. Using the combination of millimeter-wave interferometry and rich existing auxiliary data for these surveys, I study the molecular gas properties in relation to the stellar population and other ISM components within galaxies and to the global parameters of the galaxies.

Among our sample, we find that the $\mathcal{R}$ values are higher in the interacting galaxies in the isolated galaxies. However, we do not find a strong dependence of $\mathcal{R}$ on global properties such as galaxy type, stellar mass, inclination, or size of the host galaxy. On kilosparsec-scales, lower $\mathcal{R}$ values are usually found in regions with weaker ^{12}CO. We attribute this apparent trend to a bias against measuring large values when ^{12}CO is weak. Limiting our analysis to the ^{12}CO-bright regions that are less biased, we do not find that $\mathcal{R}$ correlates with the galactocentric distance, velocity dispersion of the gas, or the star formation rate (SFR) measured from 24 μm intensity for galaxies in the STING sample. For the EDGE sample, with available IFU optical spectroscopic data at the same resolution, we investigate the relation between $\mathcal{R}$ and local stellar and ionized gas properties, such as the instantaneous SFR from Hα emission, gas phase metallicity derived from optical strong line diagnostics, and star formation histories resulting from spectral modeling. For the ^{12}CO-bright regions, we find that in isolated galaxies, $\mathcal{R}$ slightly decreases with stellar mass surface density and increases with gas metallicity. On the other hand, there is no significant

correlation between $\mathcal{R}$ and line width, stellar metallicity, star formation history, SFR, or dust extinction. We also obtain azimuthally averaged $\mathcal{R}$ of our sample by stacking multiple ^{13}CO and ^{12}CO spectra in each radial bin. Roughly half of the galaxies show increased stacked $\mathcal{R}$ with galactocentric radius, suggesting that a greater fraction of diffuse or less abundant gas contributes to the molecular gas at large radii in general.

We conclude that changes in isotopic abundance due to chemical processes or nucleosynthesis do not play a dominant role in $\mathcal{R}$ variations on kpc scales. The resolved $\mathcal{R}$ is also insensitive to temperature and velocity dispersion. A changing gas density that impacts the opacity and $\mathcal{R}$ could account for the general trends we observe on kpc scales. Detailed diagnostics of the properties of molecular ISM will be provided by future high resolution, multi-line molecular observations.

To my parents

Table of Contents

List of Tables

List of Figures

List of Abbreviations

FoV	Field-of-view.
GMC	Giant molecular clouds.
IR	Infrared.
ISM	Interstellar medium.
LTE	Local thermodynamic equilibrium.
LVG	Large velocity gradient.
SFR	Star formation rate.
S/N	Signal-to-noise ratio.

List of Symbols

F_{12}	^{12}CO($J = 1 \rightarrow 0$) integrated flux.
F_{13}	^{13}CO($J = 1 \rightarrow 0$) integrated flux.
I_{12}	^{12}CO($J = 1 \rightarrow 0$) integrated intensity.
I_{13}	^{13}CO($J = 1 \rightarrow 0$) integrated intensity.
$n_{\mathrm{H_2}}$	Volume density of molecular gas.
P_0	: Probability of the null hypothesis of no correlation.
r	Galactocentric radius.
$\mathcal{R}$	^{12}CO($J = 1 \rightarrow 0$) to ^{13}CO($J = 1 \rightarrow 0$) line intensity ratio.
r_{21}	^{12}CO($J = 2 \rightarrow 1$) to ^{12}CO($J = 1 \rightarrow 0$) line intensity ratio.
R_{25}	Semimajor axis of isophotal diameter of a galaxy.
r_s	Spearman's rank correlation coefficient.
T_{k}	Kinetic temperature of molecular gas.

Chapter 1

Introduction

1.1 Molecular Gas in Nearby Galaxies

Molecular gas is one of the major components of the interstellar medium (ISM), and it plays a critical role in galaxy evolution serving as the fuel for star formation in galaxies. Detailed observations of the molecular gas reveals that star formation occurs exclusively in giant molecular clouds (GMCs) in the Milky Way and nearby galaxies. Observations in the local universe show that the global star formation rate (SFR) averaged over the entire galaxy correlate with the surface density of the total (atomic and molecular) gas (Kennicutt, 1998). Studies using high resolution data on (sub)-kpc scales reveal that the local SFR better correlates with the surface density of molecular gas than the total gas (e.g. Wong & Blitz, 2002; Bigiel et al., 2008; Kennicutt & Evans, 2012). The correlation between SFR and molecular gas suggests that the molecular ISM properties are important to the star formation process on both local and galactic scales. Because of the central role of star formation in galaxy formation and evolution, understanding physical conditions of molecular gas and how they regulate the star formation locally and globally is of great importance.

Nearby galaxies provide the opportunity to study a wide variety of galaxies with different global properties, while being close to resolve the local details within each galaxy. The global properties of galaxies are determined by large scale physical processes involved in galaxy formation and evolution, such as gas accretion on the disks and galaxy interactions. Investigating how the molecular gas depends on the global properties may give useful insights into the effects of large scale processes on molecular gas and star formation. At the same time, statistical relations between the resolved, local properties obtained by nearby surveys with high resolution can reveal mechanisms that control the star formation activity on kpc scales. Therefore, studying the molecular gas for a large sample of nearby galaxies helps link the evolution of entire galaxies to the underlying physics of how star

forms from molecular gas on local scales.

1.2 ^{13}CO Emission and the Line Ratio $\mathcal{R}$

Because the molecular hydrogen (H_2) has no permanent dipole moment, it cannot be directly observed in the cold molecular ISM ($T_{\rm k} \sim 10$ K). The most commonly used tracer of molecular gas in nearby galaxies is the ^{12}CO($J = 1 \rightarrow 0$) transition. ^{12}CO$J = 1 \rightarrow 0$) can be easily excited and thermalized under conditions typical of cold molecular gas ($T_{\rm k} \sim 10$ K and $n_{\rm H_2} \gtrsim 100$ cm^{-3}), and thus can be more easily observed than other species. However, ^{12}CO is abundant and the high opacity of ^{12}CO($J = 1 \rightarrow 0$) hampers probing of the physical conditions of the molecular gas.

The isotopologue ^{13}CO is typically $40 - 80$ times less abundant than ^{12}CO in normal, spiral galaxies. Being optically thin in most environments, ^{13}CO is a more faithful tracer of the molecular gas column density. Under local thermodynamic equilibrium (LTE), the column density of ^{13}CO can be calculated using the following equation,

$$N(^{13}\mathrm{CO}) = 3 \times 10^{14} \left(\frac{I_{13}(\mathrm{K\ km/s})}{1 - \exp(-5.3/T_k(\mathrm{K}))} \right), \tag{1.1}$$

where I_{13} is the integrated intensity of ^{13}CO, and $T_{\rm k}$ is the kinetic temperature (Wilson et al., 2009). Assuming ^{12}CO and ^{13}CO originate from the same volume, since $T_{\rm ex} = T_k$ under LTE, the kinetic temperature can be derived from the optically thick I_{12}. Assuming a constant isotopic abundance [^{13}CO/H_2], the column density of molecular gas will be obtained from I_{12} and I_{13}.

It is often useful to define a ^{12}CO($J = 1 \rightarrow 0$) to ^{13}CO($J = 1 \rightarrow 0$) flux or intensity ratio $\mathcal{R}$ for the comparisons of the two lines. Under LTE assumption, $\mathcal{R}$ is proportional to the inverse of ^{13}CO opacity $\tau(^{13}\mathrm{CO})$. The optical depth of the CO $J \rightarrow J - 1$ transition is

$$\tau_J = \frac{8\pi^3}{3h} \mu^2 \frac{J}{g_J} (e^{h\mu_J/kT_{\rm ex}} - 1) \frac{N_J}{\Delta v}, \tag{1.2}$$

where $T_{\rm ex}$, N_J, and $g_J = 2J + 1$ are the excitation temperature, the column density, and the statistical weight in the upper level J respectively; Δv is the line width; μ is the dipole moment; and h and k are the Planck and Boltzmann constants. Under LTE, $T_{\rm ex} = T_k$, and $\tau(^{13}\mathrm{CO}) \propto$

$(N/\Delta v)/T_k^2$. Higher temperature, larger line widths or lower gas column density can reduce the gas opacity and elevate the $\mathcal{R}$ value.

Besides the changes in the molecular gas opacity due to different underlying physical conditions, several mechanisms that lead to changes in the fractional abundance [^{12}CO/^{13}CO] can also cause the variations in $\mathcal{R}$. In regions with strong UV radiation, the less abundant ^{13}CO is less self-shielded than the more abundant ^{12}CO; the isotope-selective photodissociation leads to higher ^{12}CO to ^{13}CO fractional abundance, elevating the $\mathcal{R}$ value. In addition, chemical fractionation towards ^{13}CO at $\lesssim 35$ K can change the isotope abundance (Watson et al., 1976):

$$^{13}\mathrm{C}^{+} + ^{12}\,\mathrm{CO} \rightarrow ^{12}\,\mathrm{C}^{+} + ^{13}\,\mathrm{CO} + \Delta \mathrm{E}_{35\mathrm{K}}. \tag{1.3}$$

Moreover, ^{12}C and ^{13}C is also related to the nucleosynthetic history: ^{13}C is produced mainly in the AGB phase of intermediate-mass stars and accumulates slowly as a galaxy evolves, while ^{12}C is produced by all stars through various mass loss mechanisms (Henkel & Mauersberger, 1993; Prantzos et al., 1996).

1.3 Motivations for This Work

Despite the complications in interpreting $\mathcal{R}$ variations, the optically thin ^{13}CO emission and $\mathcal{R}$ are indispensable for probing physical conditions in the molecular ISM where ^{12}CO emission often saturates. Nearby galaxy studies of ^{13}CO focus more on $\mathcal{R}$, and often use the unusual $\mathcal{R}$ value as an indicator of unusual underlying gas properties or chemical abundance. A large number of nearby galaxies have global, unresolved $\mathcal{R}$ measured over the entire galaxy from single dish observations (e.g. Aalto et al., 1995; Vila-Vilaro et al., 2015). The major shortcoming of unresolved single dish $\mathcal{R}$ studies is that ^{12}CO and ^{13}CO emission can originate from different parts of the galaxy; the differences in beam filling factors of ^{12}CO and ^{13}CO add additional uncertainty in interpreting $\mathcal{R}$ and its dependence on gas properties. Meanwhile, the resolution of single dish extragalactic ^{13}CO surveys is not adequate to capture spatial variations within galaxies.

Spatially resolved observations of ^{13}CO could improve investigation of the possible gas property variations and $\mathcal{R}$. However, due to the weakness of ^{13}CO emission and the low brightness sensi-

tivities of interferometers compared to the single dish telescopes, there are only a small number of galaxies studied with high resolution interferometric mapping of ^{13}CO (e.g. Meier & Turner, 2004; Aalto et al., 2010; König et al., 2016; Sliwa et al., 2017). These mapping studies show spatial variations of $\mathcal{R}$ on (sub-)kpc scales within a galaxy. However, only a limited range of environment can be probed within each galaxy; it will be difficult to identify correlations between $\mathcal{R}$ and the local properties as inferred from the unresolved results. These individual studies are also difficult to compare with each other systematically.

In this thesis, I investigate the ^{13}CO emission and the line ratio $\mathcal{R}$ on kiloparsec scales for a wide variety of galaxies to address the molecular gas conditions in relation to the stellar population and other ISM components within galaxies and to the global parameters among different galaxies. $^{13}\mathrm{CO}(1-0)$ observations are from two high-resolution interferometric ^{12}CO extragalactic surveys: the CARMA STING survey (Rahman et al., 2011, 2012) and the EDGE survey (Bolatto et al., 2017). In Chapter 2, I present the ^{13}CO mapping survey of 12 nearby galaxies from the CARMA STING survey. Both the dependence of $\mathcal{R}$ on global properties and resolved properties are examined in this study. This project provides the first careful and systematic study of the resolved $^{12}\mathrm{CO}/^{13}\mathrm{CO}$ ratio in nearby galaxies. In Chapter 3, we extend the study of spatially resolved I_{13} and $\mathcal{R}$ on kpc scales to a larger sample of galaxies from the EDGE CALIFA survey. By combining the optical IFU data with the the CO observation at matched resolution, we study $\mathcal{R}$ in relation to the properties of stellar and ionized gas for a wide variety of galaxies. Chapter 4 presents $^{12}\mathrm{CO}(J=2\rightarrow1)$ observations for two galaxies from STING, NGC 4254 and NGC 5713, with matched resolution to estimate the physical conditions using $\mathcal{R}$ and $^{12}\mathrm{CO}(J=1\rightarrow0)/\ ^{12}\mathrm{CO}(J=2\rightarrow1)$ (r_{21}). The summary of the prospects for future observations are presented in Chapter 5.

Chapter 2

Spatially Resolved ^{13}CO in Nearby Galaxies from CARMA STING[1]

We present a ^{13}CO($J = 1 \rightarrow 0$) mapping survey of 12 nearby galaxies from the CARMA STING sample. The line intensity ratio $\mathcal{R} \equiv I[^{12}\mathrm{CO}(J = 1 \rightarrow 0)]/I[^{13}\mathrm{CO}(J = 1 \rightarrow 0)]$ is derived to study the variations in molecular gas properties. For 11 galaxies where it can be measured with high significance, the spatially resolved $\mathcal{R}$ on (sub-)kpc scales varies by up to a factor of 3–5 within a galaxy. Lower $\mathcal{R}$ values are usually found in regions with weaker ^{12}CO. We attribute this apparent trend to a bias against measuring large $\mathcal{R}$ values when ^{12}CO is weak. Limiting our analysis to the ^{12}CO bright regions that are less biased, we do not find $\mathcal{R}$ on (sub-)kpc scales correlate with galactocentric distance, velocity dispersion or the star formation rate. The lack of correlation between SFR and $\mathcal{R}$ indicates that the CO optical depth is not sensitive to stellar energy input, or that any such sensitivity is easily masked by other factors. Extending the analysis to all regions with ^{12}CO emission by spectral stacking, we find that 5 out of 11 galaxies show higher stacked $\mathcal{R}$ for galactocentric radii of $\gtrsim 1$ kpc and $\Sigma_{\mathrm{SFR}} \lesssim 0.1$ M$_\odot$ yr^{-1}kpc^{-2}, which could result from a greater contribution from diffuse gas. Moreover, significant galaxy-to-galaxy variations are found in $\mathcal{R}$, but the global $\mathcal{R}$ does not strongly depend on dust temperature, inclination, or metallicity of the galaxy.

2.1 Introduction

Molecular gas is one of the major components of the interstellar medium, and its mass is closely correlated to the rate of star formation both on galactic scales (e.g. Kennicutt, 1998; Gao & Solomon, 2004; Evans et al., 2006) and (sub-)kpc scales within galaxies (e.g. Wong & Blitz, 2002;

[1]This Chapter is published in Cao et al. (2017).

Bigiel et al., 2008; Rahman et al., 2012; Leroy et al., 2013). The most commonly used tracer of molecular gas in nearby galaxies is the ^{12}CO($J = 1 \rightarrow 0$) transition. The column density and mass of molecular gas is often estimated from the ^{12}CO($J = 1 \rightarrow 0$) line intensity (I_{12}) by multiplying by a standard ^{12}CO-to-H_2 conversion factor $X_{\rm CO} \equiv N(H_2)/I_{12} = 2 \times 10^{20}$ cm^{-2}(K km s^{-1})$^{-1}$ (Young & Scoville, 1982; Thronson & Shull, 1990; Bolatto et al., 2013). However, because ^{12}CO is abundant and its low level transitions are often optically thick, I_{12} is only an approximate tracer of column density, and the $X_{\rm CO}$ factor can vary depending on different underlying physical conditions in the molecular gas.

^{13}CO, as a much less abundant ($\sim 1/40$ of ^{12}CO in the Milky Way) isotopologue, is optically thin in most environments, and can be combined with ^{12}CO observations to get further information on physical conditions in the molecular gas. Under local thermodynamic equilibrium (LTE), assuming ^{12}CO and ^{13}CO share the same excitation temperature and originate from the same volume, the opacity of the ^{13}CO emission can be derived from the ^{12}CO and ^{13}CO intensities, for optically thick ^{12}CO that fills the telescope beam. In Milky Way studies of well resolved giant molecular clouds (GMCs), assumptions of LTE and thin to moderately thick ^{13}CO are used to derive the molecular column density and mass (e.g. Goldsmith et al., 2008; Roman-Duval et al., 2016). More generally, in non-LTE situations, the isotopic line ratio is no longer a simple tracer of opacity and is dependent on the kinetic temperature T_k, the density $n(H_2)$, the ^{12}CO column density per unit velocity interval $N(^{12}{\rm CO})/\Delta v$, and the isotopic abundance ratio $[^{12}{\rm CO}]/[^{13}{\rm CO}]$; with only one optically thick and one optically thin line it is only feasible to constrain $n(H_2)$ and $N(^{12}{\rm CO})/\Delta v$ by adopting values for T_k and $[^{12}{\rm CO}]/[^{13}{\rm CO}]$ (e.g., Hirota et al., 2010).

It is often useful to define a ^{12}CO to ^{13}CO flux or intensity ratio $\mathcal{R}$, $\mathcal{R} \equiv I_{12}/I_{13}$, to characterize differences between the two types of emission. Under LTE and optically thin ^{13}CO assumptions,

$$\mathcal{R} \sim \frac{1}{\tau(^{13}{\rm CO})} \sim \frac{[^{12}{\rm CO}]}{[^{13}{\rm CO}]} \frac{1}{\tau(^{12}{\rm CO})} \tag{2.1}$$

Explanations for different values of $\mathcal{R}$ fall into two categories: changes in the molecular gas opacity due to different underlying physical conditions, or variations in the fractional abundance $[^{12}{\rm CO}/^{13}{\rm CO}]$. Generally, higher temperature, larger line widths or lower gas column density can reduce the gas opacity and elevate the $\mathcal{R}$ value. The relative isotopic abundance of ^{12}CO to

^{13}CO can be affected by several different processes. In strong interstellar radiation fields, the less abundant ^{13}CO is more vulnerable to the photodissociation than ^{12}CO, so the ^{12}CO to ^{13}CO fractional abundance will increase and elevate the $\mathcal{R}$ value. Another process that may change the isotope abundance is chemical fractionation towards ^{13}CO at $\lesssim$ 35 K (Watson et al., 1976). Furthermore, chemical evolution of ^{12}C and ^{13}C through galactic nucleosynthesis can also play an important role in determining $\mathcal{R}$ (Henkel & Mauersberger, 1993; Prantzos et al., 1996).

Early studies of ^{13}CO in nearby galaxies used single dishes to derive the flux ratio of ^{12}CO to ^{13}CO of a galaxy, and found that $\mathcal{R}$ values are very high (> 20) in (U)LIRGs which host strong starbursts (e.g. Aalto et al., 1991; Casoli et al., 1992), while $\mathcal{R}$ in normal galaxies typically ranges from 5 to 15 (e.g. Young & Sanders, 1986; Sage & Isbell, 1991; Aalto et al., 1995; Paglione et al., 2001). $\mathcal{R}$ shows weak correlations with the infrared(IR) color F_{60}/F_{100} (Aalto et al., 1991; Crocker et al., 2012) and the star formation rate surface density (Davis, 2014). One explanation of these weak correlations is that the ^{12}CO opacity is reduced when feedback from active star formation heats the interstellar medium (ISM) and increases the velocity dispersion of gas (Crocker et al., 2012; Davis, 2014). However, no strong correlation between $\mathcal{R}$ and galaxy properties has been found, with studies that have surveyed a considerable number of normal galaxies revealing a large scatter in $\mathcal{R}$ (Aalto et al., 1995; Vila-Vilaro et al., 2015).

There are also a handful of nearby galaxies that have been imaged in ^{13}CO using interferometers (e.g. Turner & Hurt, 1992; Rosolowsky & Blitz, 2005; Meier & Turner, 2004; Aalto et al., 2010; König et al., 2016). These mapping studies show spatial variations of $\mathcal{R}$ on (sub-)kpc scales within a galaxy; the typical value of $\mathcal{R}$ is ~ 6 in galaxy disks, similar to that in Milky Way disk clouds (Polk et al., 1988; Roman-Duval et al., 2016). Abnormally high $\mathcal{R}$ and steep $\mathcal{R}$ gradients are often found in extreme environments such as the nuclei of starbursts (Aalto et al., 2010), or in places where dynamic evolution of gas structures may take place (Hüttemeister et al., 2000; Meier & Turner, 2004). However, spatially resolved ^{13}CO studies usually focus on a single galaxy; whether and how resolved $\mathcal{R}$ changes in response to local environmental conditions remains unclear. A survey of spatially resolved ^{13}CO combining multiple galaxies can be used to extend the range of local environments investigated. Furthermore, galaxy-to-galaxy differences can also contribute to systematic differences in $\mathcal{R}$. Therefore, such a resolved survey can be used to study the effects of

both local environments and global galaxy properties on $\mathcal{R}$.

In this paper, we study $\mathcal{R}$ by comparing the ^{12}CO and ^{13}CO emission over a diverse sample of galaxies from the CARMA STING survey. We present the observational data in Section **??**. We describe our measurement of the ^{13}CO intensity and $\mathcal{R}$ in Section 2.3, as well as the possible bias resulting from limited sensitivity. In Section 2.4, we investigate the dependence of spatially resolved $\mathcal{R}$ on local line width, galactocentric distance, and star formation rate in each galaxy, and the correlations between global $\mathcal{R}$ and galaxy properties in the sample. We discuss the implications and limitations of this work in Section 2.5.

2.2 Sample and Data Reduction

The CARMA Survey Toward Infrared-bright Nearby Galaxies (STING) is a interferometric survey of 23 normal galaxies. The sample galaxies are selected from from the IRAS Revised Bright Galaxy Survey (Sanders et al., 2003), with $\delta > -20°$, moderate inclination ($i < 75°$) , and distance < 45 Mpc. The sample has a wide range of stellar mass and star formation activity. The STING ^{12}CO data have been studied by Rahman et al. (2011, 2012) and Wong et al. (2013).

Observations were carried from 2008 to 2010 using the C, D, and E configurations of CARMA, utilizing both 6m and 10m diameter antennas, and yielding a typical synthesized beam of $\sim 3'' - 5''$ (corresponding to scales of $\sim 100 - 700$ pc). Simultaneous ^{12}CO and ^{13}CO observations were only possible for datasets beginning in mid-2008, due to early limitations in the IF bandwidth. Furthermore, in several galaxies (NGC 337, 2976, 3486, 3949, 5371) the ^{13}CO line was not confidently detected. Thus we focus in this paper on the 12 galaxies listed in Table 2.1. We note that equal integration time was spent on ^{12}CO and ^{13}CO, so the signal-to-noise ratio (S/N) for the ^{13}CO maps is generally poorer because of the relative weakness of the line.

Data reduction was performed using the MIRIAD package (Sault et al., 1995), which applies linelength corrections, passband and phase calibration, and flux density bootstrapping using a planet or bright quasar. Imaging and deconvolution were performed using the MIRIAD tasks INVERT and MOSSDI with Briggs' "robust" parameter set to 0.5. The ^{12}CO and ^{13}CO cubes were then convolved and re-sampled to a common spatial grid and angular resolution before undertaking further analysis. The grid size is $1''$, and the angular resolution is the larger of the ^{12}CO and ^{13}CO

cubes' resolution. The FWHM major and minor axes of the common resolution Gaussian beam are listed for each galaxy in Table 2.2.

Table 2.1. Basic galaxy properties of the STING sample

Galaxy	R.A.[a]	Dec.[a]	Distance[b]	i	P.A.	i, P.A.[c]	R_{25} [d]	log(O/H)	Metal.[e]	Morph. [a]
	(J2000)	(J2000)	(Mpc)	(°)	(°)	Ref.	(″)	+12	Ref.	class
NGC0772	$01^h59^m19^s.6$	$+19°00'27''.1$	30.2	37	315	1	217.3	8.87 ± 0.13	1	Sb
NGC1569	$04^h30^m49^s.1$	$+64°50'52''.6$	2.5	63	112	2	108.9	8.13 ± 0.12	2	IB
NGC1637	$04^h41^m28^s.2$	$-02°51'28''.7$	9.8	39	213	1	119.5	8.80 ± 0.34	3	Sc
NGC3147	$10^h16^m53^s.7$	$+73°24'02''.7$	40.9	32	147	3	116.7	9.02 ± 0.36	4	Sbc
NGC3198	$10^h19^m55^s.0$	$+45°32'58''.6$	14.0	72	215	4	255.3	8.62 ± 0.28	5	Sc
NGC3593	$11^h14^m37^s.0$	$+12°49'03''.6$	5.5	67	90	1	157.4	8.29 ± 0.26	4	S0-a
NGC4254	$12^h18^m49^s.6$	$+14°24'59''.4$	15.6	31	69	5	161.1	8.79 ± 0.34	5	Sc
NGC4273	$12^h19^m56^s.1$	$+05°20'36''.0$	36.6	61	189	1	70.3	9.14 ± 0.20	6	Sc
NGC4536	$12^h34^m27^s.1$	$+02°11'17''.3$	14.7	68	301	6	227.6	8.61 ± 0.40	5	SABb
NGC4654	$12^h43^m56^s.6$	$+13°07'36''.0$	16.1	62	125	6	146.9	8.83 ± 0.27	7	SABcd
NGC5713	$14^h40^m11^s.5$	$-00°17'20''.3$	21.4	33	203	7	82.7	8.64 ± 0.40	4	SABb
NGC6951	$20^h37^m14^s.1$	$+66°06'20''.3$	23.3	46	138	8	116.7	8.99 ± 0.36	4	SABb

[a] From NED.

[b] Weighted average from NED of redshift-independent distances.

[c] References for i and P.A. (1) Axis ratio and position angle are from K_s (LGA/2MASS isophotoal) on NED Diameters page, in homogenized units. Inclination is derived from the axis ratio using Hubble's (1926) formula with intrinsic flattening of 0.11. (2) Mühle et al. (2005); (3) Epinat et al. (2008); (4) de Blok et al. (2008); (5) Dicaire et al. (2008); (6) Chemin et al. (2006); (7) Daigle et al. (2006); (8) Haan et al. (2009).

[d] Semi major axis from RC3 in arcsec, from NED Diameters page, homogenized units.

[e] References of metallicity. (1) Anderson et al. (2010); (2) Engelbracht et al. (2008); (3) van Zee et al. (1998); (4) Calculated from absolute B magnitude using $L - Z$ relations by Moustakas et al. (2010); (5) Characteristic values from Table 9 in Moustakas et al. (2010); (6) Prieto et al. (2008); (7)

2.3 ^{13}CO Measurements

2.3.1 Integrated intensity

We calculated the velocity-integrated intensity by summing the individual channels from the three-dimensional data cube after applying a blanking mask. To generate the blanking mask, the ^{12}CO cube is smoothed such that the beam FWHM becomes twice its original value. Regions with emission greater than $4\sigma_{\rm ch}$ in two adjacent channels of the smoothed cube are used as the core mask, where $\sigma_{\rm ch}$ is the noise in each individual channel. Then the mask is expanded to contain all regions with emission greater than $3\sigma_{\rm ch}$ that are connected in position or velocity space with

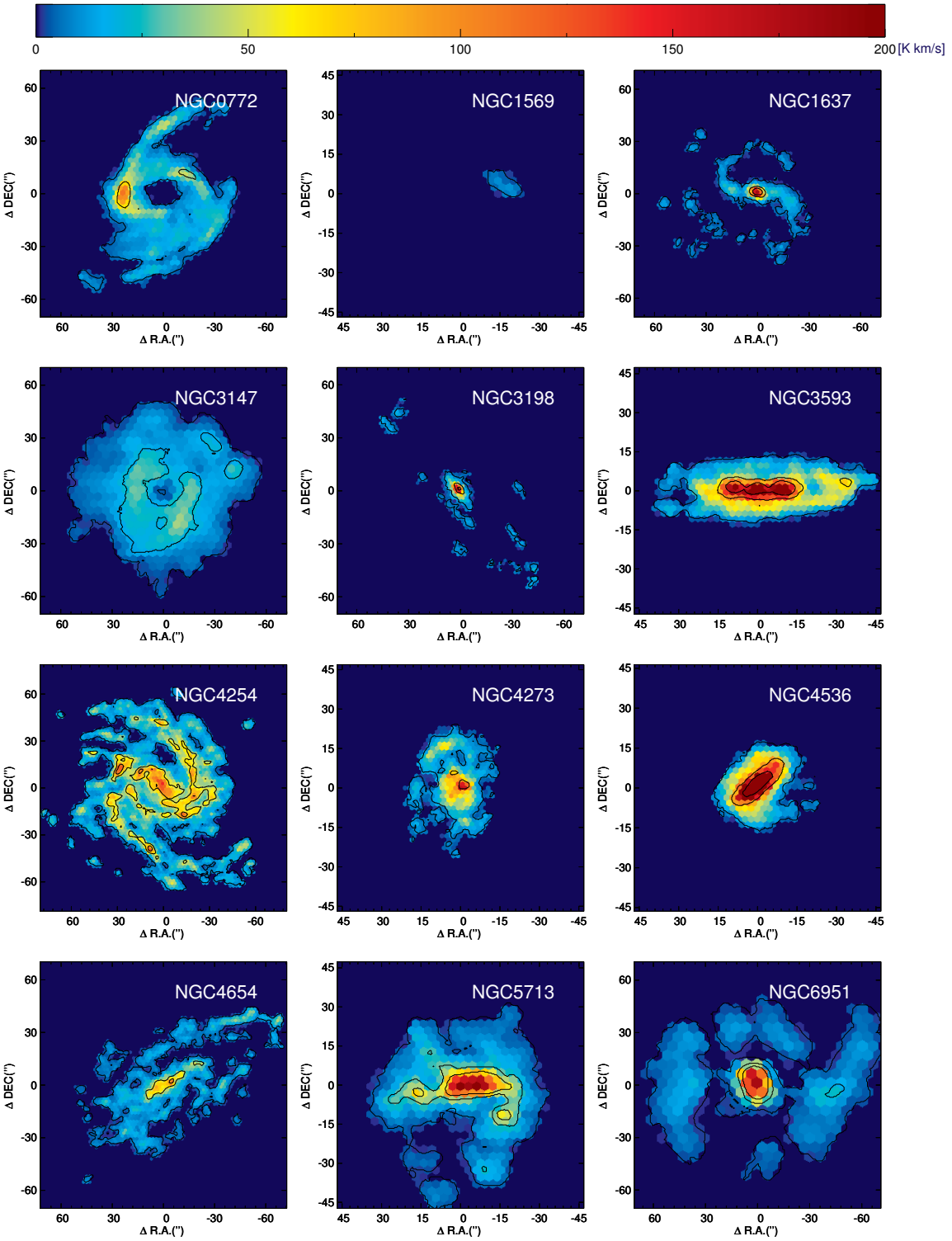

Figure 2.1. ^{12}CO($J = 1 \rightarrow 0$) integrated intensity maps of the 12 STING galaxies with ^{12}CO($J = 1 \rightarrow 0$) detected. The maps are resampled to hexagonal grids described in Section 2.3.1. The contours show S/N of ^{12}CO($J = 1 \rightarrow 0$) at the levels of $[3, 21, 39]$.

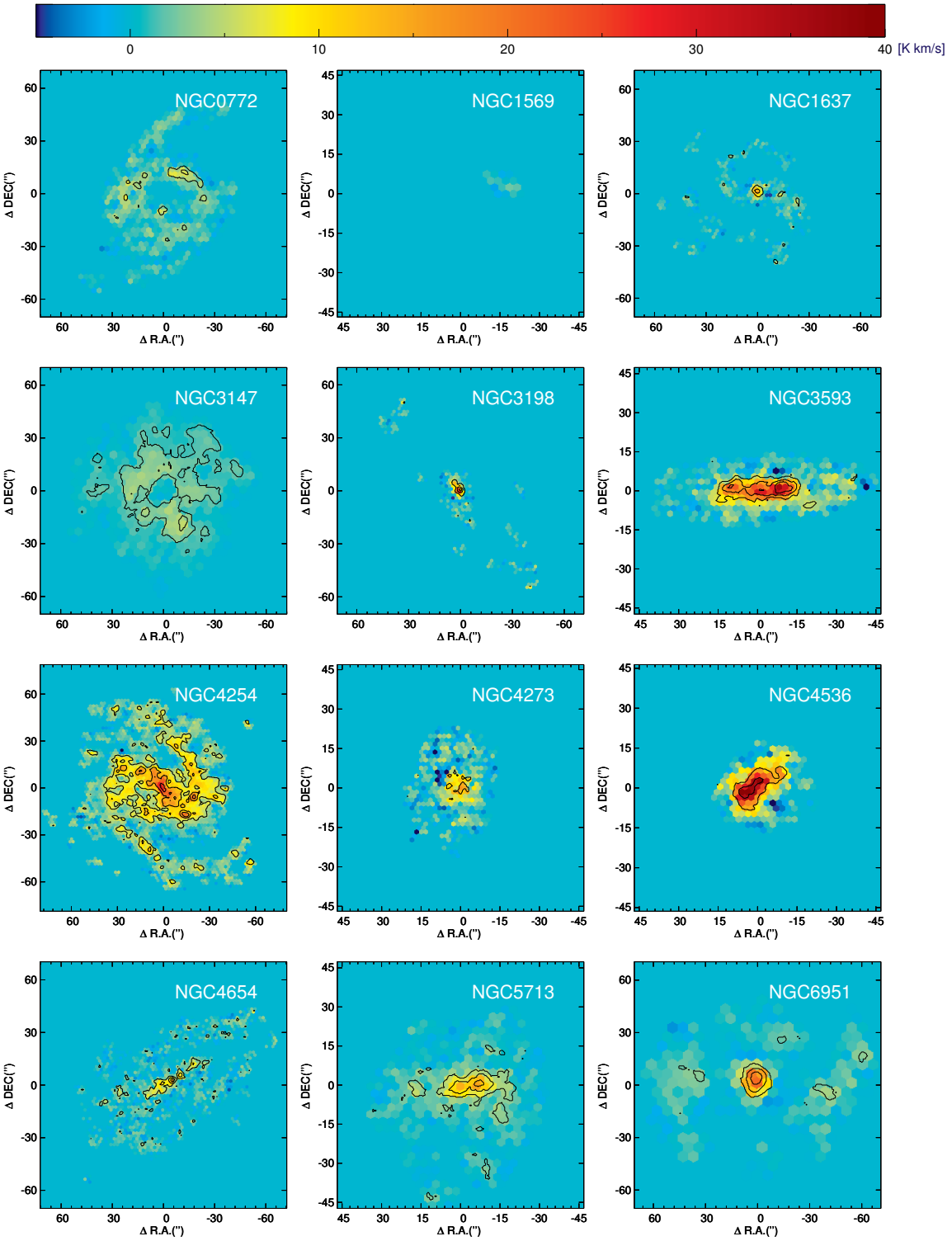

Figure 2.2. ^{13}CO($J = 1 \rightarrow 0$) integrated intensity maps of the 12 galaxies, using same masks as in Figure 2.1. Contours show S/N of ^{13}CO($J = 1 \rightarrow 0$) at the levels of $[3, 6, 9]$.

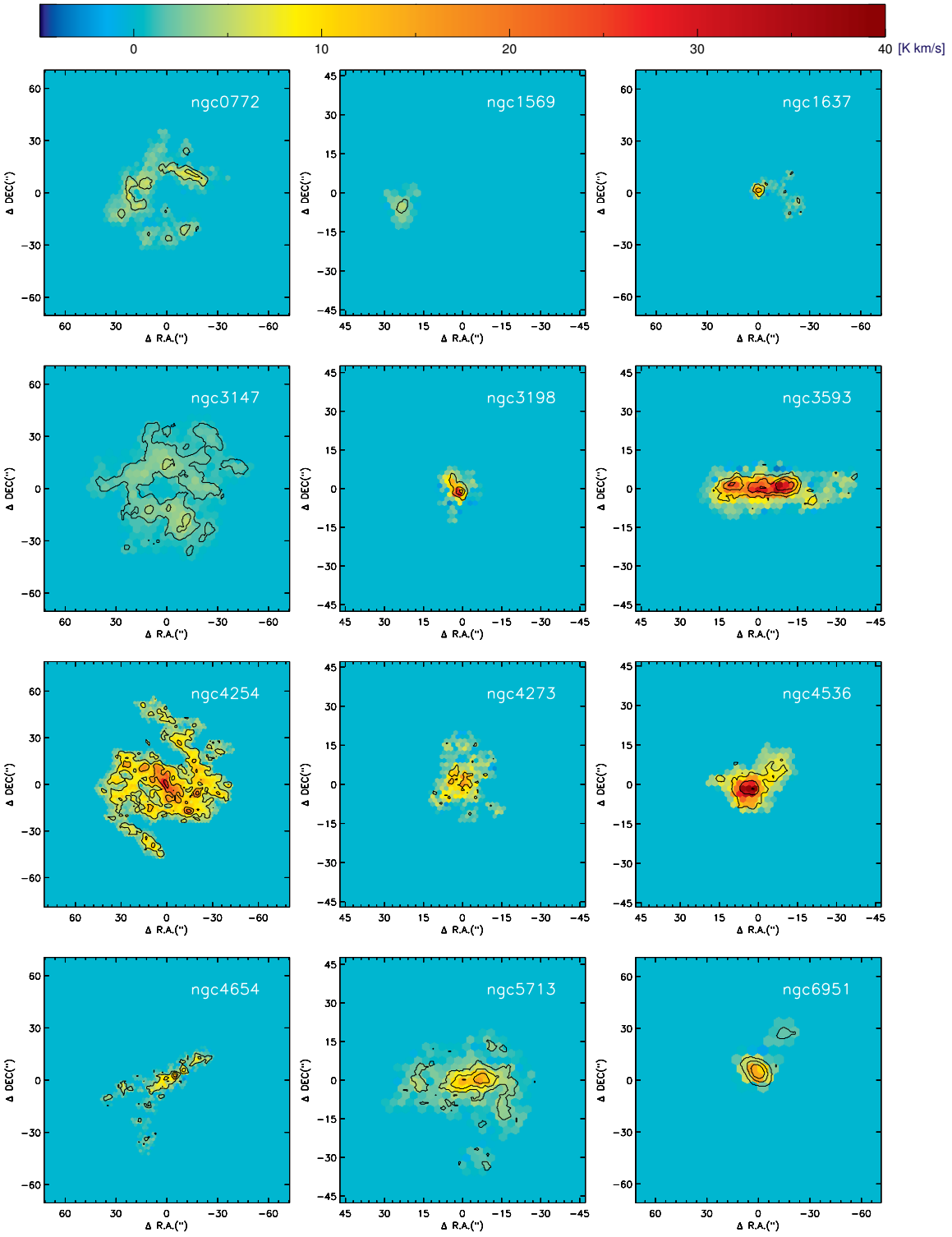

Figure 2.3. ^{13}CO($J = 1 \rightarrow 0$) integrated intensity maps of the 12 galaxies, using ^{13}CO masks (M13). Contours show S/N of ^{13}CO($J = 1 \rightarrow 0$) at the levels of $[3, 6, 9]$.

the core mask. The same ^{12}CO mask (which we call M12) is used for generating both ^{12}CO and ^{13}CO intensity maps for each galaxy, based on the assumption that the much weaker ^{13}CO emission should be confined to regions where ^{12}CO is detected.

We generate hexagonal sampling grids with sampling points spaced by $\sqrt{3/8}$ times the FWHM of the major axis of the synthesized beam, such that the area of two hexagons equals one beam area approximately. Each hexagon is assigned the intensity and other spatially resolved properties of the $1''$ pixel nearest to its center. The ^{12}CO and ^{13}CO intensity maps based on such grids are shown in Figure 2.1 and Figure 2.2. Generally, ^{13}CO maps show similar morphological characteristics to their ^{12}CO counterparts. However, because of the relatively weaker emission and low S/N of ^{13}CO compared to ^{12}CO, ^{13}CO detections are mostly confined in regions with bright ^{12}CO. Further away from the galactic center when ^{12}CO drops, ^{13}CO only appears in a few spots and looks much clumpier.

For comparison, we also generated the ^{13}CO intensity map from an independent blanking mask based on the ^{13}CO data cube (referred as M13) for each galaxy in our sample. The mask was generated by degrading the angular resolution of ^{13}CO cube by a factor of 3, and smoothing the spectra by a Gaussian function with FWHM of 3 times the channel width. The mask core had a clip level of 4σ and was extended to adjacent regions or channels with emission greater than 2σ. These intensity maps were also resampled onto the half-beam hexagonal grids and shown in Figure 2.3.

The ^{13}CO intensity maps from M13 have similar morphological characteristics with those from M12 (Figure 2.2). The similarities of the intensities resulting from the two masks where ^{13}CO are strong suggest that the ^{12}CO masks M12 are suitable for the ^{13}CO imaging. Some subtle differences result from the inclusion of noise from the ^{13}CO cube when using the M12 masks; the ^{13}CO maps generated by applying the M13 masks contain only positive emission, whereas the M12 masks sometimes enclose noisy regions with negative values from the ^{13}CO data cubes, reducing the integrated intensity. In addition, the M12 masks pick up regions with faint ^{13}CO emission extending into the spiral arms which cannot be detected using the M13 masks. We adopt the results obtained with the M12 masks for the resolved ^{13}CO intensity in this study.

To reduce the largely oversampled data from the original images with $1''$ pixels, further analysis

of resolved intensities throughout this study are based on the hexagonal grids shown in the maps, which we hereafter refer to as "half-beams". However, fluxes are measured using the original, heavily oversampled maps (see Sections 2.3.2 and 2.3.3.1). We divide the half-beams into three groups based on their ^{12}CO and ^{13}CO intensities: the ^{13}CO-detections have both ^{12}CO intensity I_{12} and ^{12}CO intensity I_{13} detected with S/N > 3, the ^{12}CO-only-detections have I_{12} detected with S/N > 3 but I_{13} under the detection threshold of 3, and the ^{12}CO-non-detections have S/N of I_{12} below 3. Note that we use the ^{12}CO derived mask M12 for obtaining I_{12}, and because ^{12}CO has higher S/N than ^{13}CO, the union of the ^{13}CO-detections and ^{12}CO-only-detections includes all of the half-beams that have I_{12} detected with S/N > 3.

For each of the half-beams, the error in integrated intensity was calculated by multiplying the square root of the sum of $\sigma_{\rm ch}^2$ within the velocity range of the mask by the width of the channel. The mean 1σ noise levels of I_{12} (represented as $\langle\sigma_{12}\rangle$) and ^{13}CO (as $\langle\sigma_{13}\rangle$) over the entire maps are listed in Table 2.2. For the ^{13}CO integrated intensity, we also calculate the mean 1σ noise levels of the ^{13}CO-detections ($\langle\sigma_{13}\rangle_{\rm Det}$). Note that $\langle\sigma_{13}\rangle_{\rm Det}$ is larger than $\langle\sigma_{13}\rangle$ in each galaxy, reflecting the larger velocity width of the M12 mask in regions where ^{13}CO is detected. In the last two columns of Table 2.2, we list the numbers of half-beams with S/N > 3 for both ^{13}CO and ^{12}CO respectively. The former is the number of the ^{13}CO-detections we defined, and the later counts both the ^{13}CO-detections and the ^{12}CO-only-detections.

2.3.2 Flux spectra

For each channel, we sum the line intensity over the extent of the mask in the channel to obtain the line flux. The noise of flux of each channel is calculated by taking the square root of the sum of $\sigma_{\rm ch}$ over the extent of mask in the channel. Figure 2.4 shows the ^{12}CO and ^{13}CO flux spectra of each galaxy with the same M12 mask applied, as well as the ^{13}CO flux spectra with the M13 mask applied for comparison (red histogram). The ^{13}CO spectra are scaled by a factor of 5 for easier viewing. The ^{13}CO emission fluxes derived using the M13 masks are similar to those using the M12 masks for channels where the line is detected with high significance. This confirms the reality of the ^{13}CO detections and indicates that they are not an artifact of the masking procedure. On the other hand, the tendency of the $^{13}{\rm CO}_{\rm M12}$ spectrum to recover more flux than the $^{13}{\rm CO}_{\rm M13}$

Table 2.2. Mapping properties of the sample galaxies from STING

Galaxy	$\theta_{\rm maj} \times \theta_{\rm min}$ [a] ($'' \times ''$)	Mean noise levels (K km s^{-1})			Number of half-beams detected with S/N > 3 in	
		$\langle\sigma_{13}\rangle_{\rm Det}$ [b]	$\langle\sigma_{13}\rangle$ [c]	$\langle\sigma_{12}\rangle$ [d]	^{13}CO [e]	^{12}CO [f]
NGC0772	5.00×5.00	1.31	1.25	2.21	19	537
NGC1569	4.71×4.31	...	0.84	1.22	0	12
NGC1637	3.48×3.17	1.61	1.16	1.73	18	345
NGC3147	7.50×7.50	0.66	0.56	0.80	102	420
NGC3198	3.18×2.82	2.50	1.67	2.48	15	160
NGC3593	3.87×3.68	2.85	2.06	3.07	52	312
NGC4254	3.34×2.74	2.05	1.85	2.35	665	2244
NGC4273	2.87×2.73	3.49	2.16	3.46	13	298
NGC4536	3.86×3.46	5.35	3.57	4.01	32	158
NGC4654	3.10×2.90	1.33	1.05	1.68	84	1121
NGC5713	5.07×4.64	1.24	0.87	1.25	42	348
NGC6951	9.96×8.53	1.72	0.92	0.82	12	224

[a] FWHM of the major and minor axes of the common Gaussian beam obtained after convolution of both the ^{12}CO and ^{13}CO cubes.

[b] Mean 1σ noise of I_{13} for the ^{13}CO-detections in the M12 mask.

[c] Mean 1σ noise of I_{13} for the entire M12 mask.

[d] Mean 1σ noise of I_{12} for the entire M12 mask.

[e] Number of half-beams detected in ^{13}CO with S/N > 3, i.e. the ^{13}CO-detections defined in Section 2.3.1.

[f] Number of half-beams detected in ^{12}CO with S/N > 3, i.e. union of the ^{13}CO-detections and the ^{12}CO-only-detections defined in in Section 2.3.1.

spectrum underscores the value of using the ^{12}CO mask as a constraint in cases where the ^{13}CO emission is weak. For NGC 1569, 3593 and 4273, there are a few channels with apparent ^{13}CO detections (using the M13 mask) but not corresponding ^{12}CO emission. Such detections of ^{13}CO emission outside the M12 mask occur near the edge of the field of view, where the primary beam corrections are large, and are thus likely to be spurious.

We obtain velocity-integrated line fluxes by multiplying the sum of channel fluxes the width of the channel. We present the integrated fluxes of ^{13}CO and ^{12}CO with the M12 masks in columns (2) and (4) in Table 2.3. The error on the velocity-integrated line flux is calculated by multiplying the square root of the sum of the noise of flux squared by the width of the channel. For comparing the ^{13}CO fluxes resulting from different masks, we also provide the velocity-integrated ^{13}CO fluxes measured in the M13 masks in column (3) of Table 2.3. ^{13}CO integrated fluxes using M12 and

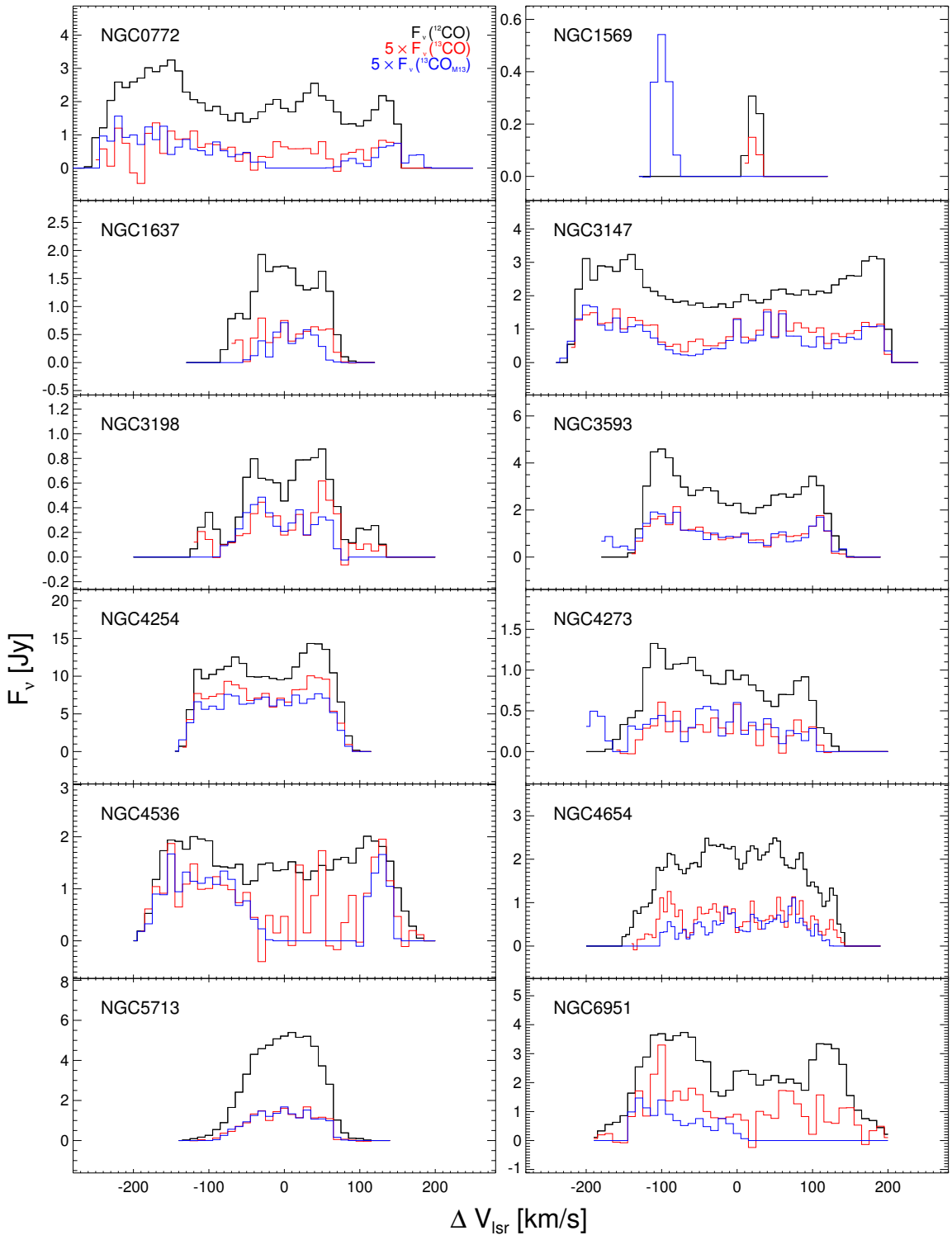

Figure 2.4. Total flux spectra plotted as a function of offset from the systematic velocity. Black lines show the total flux of ^{12}CO. Blue lines show the ^{13}CO flux spectra with the same ^{12}CO mask (M12), and the red lines are the ^{13}CO flux spectra obtained using the ^{13}CO mask (M13). See text for the detailed description of the masks. The ^{13}CO fluxes are scaled by a factor of 5 for clarity.

M13 are similar except for NGC 1569 and NGC 6951. As shown in Figure 2.4 some significant half-beams were detected in M13 but not M12 for NGC 1569, resulting in more flux using M13 than M12; in NGC 6951, low S/N of ^{13}CO per channel results in less integrated flux measured in the M13 mask than M12. We adopt the results obtained with the M12 masks for all subsequent analysis in this study.

As the interferometer may filter out flux distributed on large scales, our data may have underestimated the total flux. We use single-dish $^{12}\mathrm{CO}(J = 2 \rightarrow 1)$ observations available for some galaxies in the sample to compare with our interferometer data. The single-dish data used are part of the HERA CO Line Extragalactic Survey (HERACLES) (Leroy et al., 2009) using the Institut de Radio Astronomie Millimetrique (IRAM) 30m telescope. The 2.6 km s^{-1} velocity channels of the single-dish data were regridded to match the interferometer data cube. Fluxes measured within a circular aperture of radius 60″ centered on the nucleus were used for the comparison. The resulting single-dish fluxes were divided by a factor of 4 to obtain the equivalent $^{12}\mathrm{CO}(J = 1 \rightarrow 0)$ flux, by assuming the peak brightness temperature is approximately the same for the $^{12}\mathrm{CO}(J = 1 \rightarrow 0)$ and $^{12}\mathrm{CO}(J = 2 \rightarrow 1)$ transitions.

In Figure 2.5, we show comparisons between the flux spectra of the masked $^{12}\mathrm{CO}(J = 1 \rightarrow 0)$ from our interferometer observations and the equivalent $^{12}\mathrm{CO}(J = 1 \rightarrow 0)$ derived from the $^{12}\mathrm{CO}(J = 2 \rightarrow 1)$ single-dish data. In the four galaxies we compared, the interferometer flux spectra have similar characteristics to the single-dish spectra. Typically, the interferometer recovers more than 80% of the single dish flux in the majority of channels except for NGC 3198. In NGC 3198, the typical ratio of interferometer flux to single dish flux is 0.55. In NGC 4536, for a few channels within ± 50 km s^{-1} of the LSR velocity, the flux recovery of CARMA is $10 - 20\%$ lower than for the other channels. This is consistent with a more extended distribution of molecular gas near the minor axis of the galaxy which the interferometer is less sensitive to. The higher $^{12}\mathrm{CO}(J = 2 \rightarrow 1)$ flux could also be due to a steep density gradient or higher temperature in the center of NGC 4536. We will discuss the possible impact of incomplete flux recovery on our results in Section 2.5.

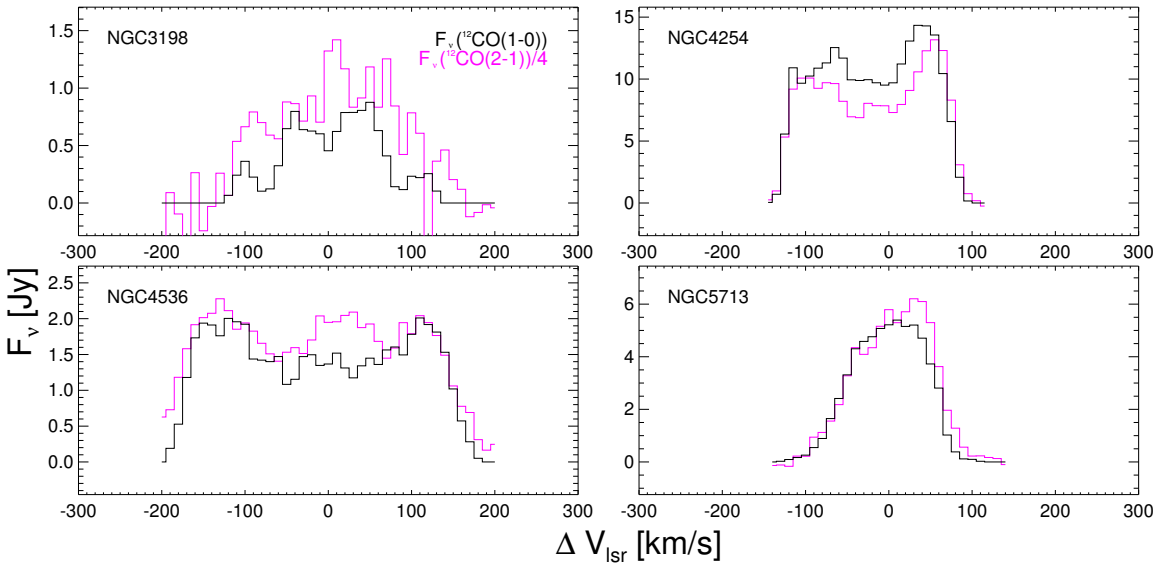

Figure 2.5. CARMA and IRAM total flux spectra comparison. Black lines show the total flux of ^{12}CO($1 \rightarrow 0$) using the M12 mask; magenta lines show the equivalent ^{12}CO($1 \rightarrow 0$) flux derived from 1/4 of the total flux of ^{12}CO($2 \rightarrow 1$) by HERACLES.

2.3.3 Line ratios

2.3.3.1 Flux ratios

For each galaxy, we calculate a ^{12}CO-to-^{13}CO flux ratio, $F(^{12}\mathrm{CO})/F(^{13}\mathrm{CO})$, by directly taking the ratio of ^{12}CO and ^{13}CO integrated fluxes in columns (4) and (2) of Table 2.3. The resulting flux ratios are presented in column (5) of Table 2.3. As the integrated lines fluxes are obtained by summing up all the line emission over the extent of the M12 mask, these flux ratios are comparable to ratios of unresolved line intensities taken at much lower resolutions by single dishes. Our flux ratios range from 7 to 18, with a typical value around 10. These values are consistent with flux ratios measured in unresolved studies for normal galaxies (Aalto et al., 1991, 1995; Eckart et al., 1990; Sage & Isbell, 1991; Young & Sanders, 1986; Vila-Vilaro et al., 2015). No extremely high values (> 20) are found in our sample due to the sample selection: most of the reported $\mathcal{R} > 20$ values are from luminous mergers (Casoli et al., 1992; Aalto et al., 1991, 2010), which are not present in our sample.

Table 2.3. Fluxes and line ratios of the STING sample

Galaxy	$F(^{13}\mathrm{CO})$ (Jy km s^{-1})	$F(^{13}\mathrm{CO}_{\mathrm{M13}})$ [a] (Jy km s^{-1})	$F(^{12}\mathrm{CO})$ (Jy km s^{-1})	$\frac{F(^{12}\mathrm{CO})}{F(^{13}\mathrm{CO})}$	$\langle\mathcal{R}\rangle$
(1)	(2)	(3)	(4)	(5)	(6)
NGC0772	45.45 ± 3.81	39.31 ± 2.21	816.51 ± 4.85	17.97 ± 1.51	7.63 ± 2.58
NGC1569	0.56 ± 0.39	2.69 ± 0.61	6.26 ± 0.61	11.10 ± 7.71	...
NGC1637	13.78 ± 1.62	8.22 ± 0.86	201.34 ± 2.54	14.61 ± 1.73	11.10 ± 3.03
NGC3147	81.21 ± 3.31	69.06 ± 2.52	946.14 ± 4.82	11.65 ± 0.48	7.82 ± 1.65
NGC3198	11.13 ± 1.44	8.62 ± 1.04	112.02 ± 2.23	10.06 ± 1.32	7.03 ± 2.07
NGC3593	57.63 ± 3.21	62.90 ± 2.92	732.03 ± 4.93	12.70 ± 0.71	8.04 ± 1.28
NGC4254	316.19 ± 4.95	268.62 ± 3.76	2279.52 ± 6.83	7.21 ± 0.11	5.30 ± 1.58
NGC4273	13.97 ± 1.98	19.13 ± 1.50	229.05 ± 3.17	16.40 ± 2.34	7.54 ± 2.31
NGC4536	54.61 ± 3.98	40.43 ± 2.26	525.67 ± 4.49	9.63 ± 0.71	7.56 ± 2.16
NGC4654	33.69 ± 2.01	21.61 ± 1.01	498.27 ± 3.40	14.79 ± 0.89	7.41 ± 2.31
NGC5713	34.05 ± 2.39	33.53 ± 1.83	619.37 ± 3.57	18.19 ± 1.28	13.98 ± 2.90
NGC6951	73.46 ± 7.41	23.57 ± 2.57	828.35 ± 7.31	11.28 ± 1.14	8.65 ± 1.58

[a]Integrated flux from ^{13}CO intensity maps using the M13 mask.

2.3.3.2 Intensity ratio maps

We generated spatially resolved $\mathcal{R}$ maps for each galaxy from the velocity-integrated intensity maps of ^{12}CO and ^{13}CO. The uncertainty in $\mathcal{R}$ at each half-beam was calculated by propagating the uncertainties in the ^{12}CO and ^{13}CO intensities. Figure 2.6 shows maps of the line ratio $\mathcal{R}$, where measured with $> 3\sigma$ significance, for all of the sample galaxies. The black contours in Figure 2.6 indicate the distribution of ^{12}CO emission. Within galaxies, $\mathcal{R}$ in individual half-beams varies by a factor of 3 to 5 across the disk, mostly ranging from 5 to 15. The typical values are consistent with previous $\mathcal{R}$ measurements of spiral galaxies on similar scales (e.g. Hirota et al., 2010; Pety et al., 2013).

Within our detection limit, comparing to studies with similar sensitivities, we do not have reliable $\mathcal{R}$ measurements higher than 30 as reported by some previous studies near starbursting regions (Hüttemeister et al., 2000; Aalto et al., 2010). Nor did we find dramatic variations of $\mathcal{R}$ within each galaxy, while spatial variations in $\mathcal{R}$ of more than a factor of 3 over scales of 1 kpc are seen in some starbursting galaxies (Hüttemeister et al., 2000; Aalto et al., 2010; Meier & Turner, 2004). The rather moderate $\mathcal{R}$ values and their limited variations are partly because

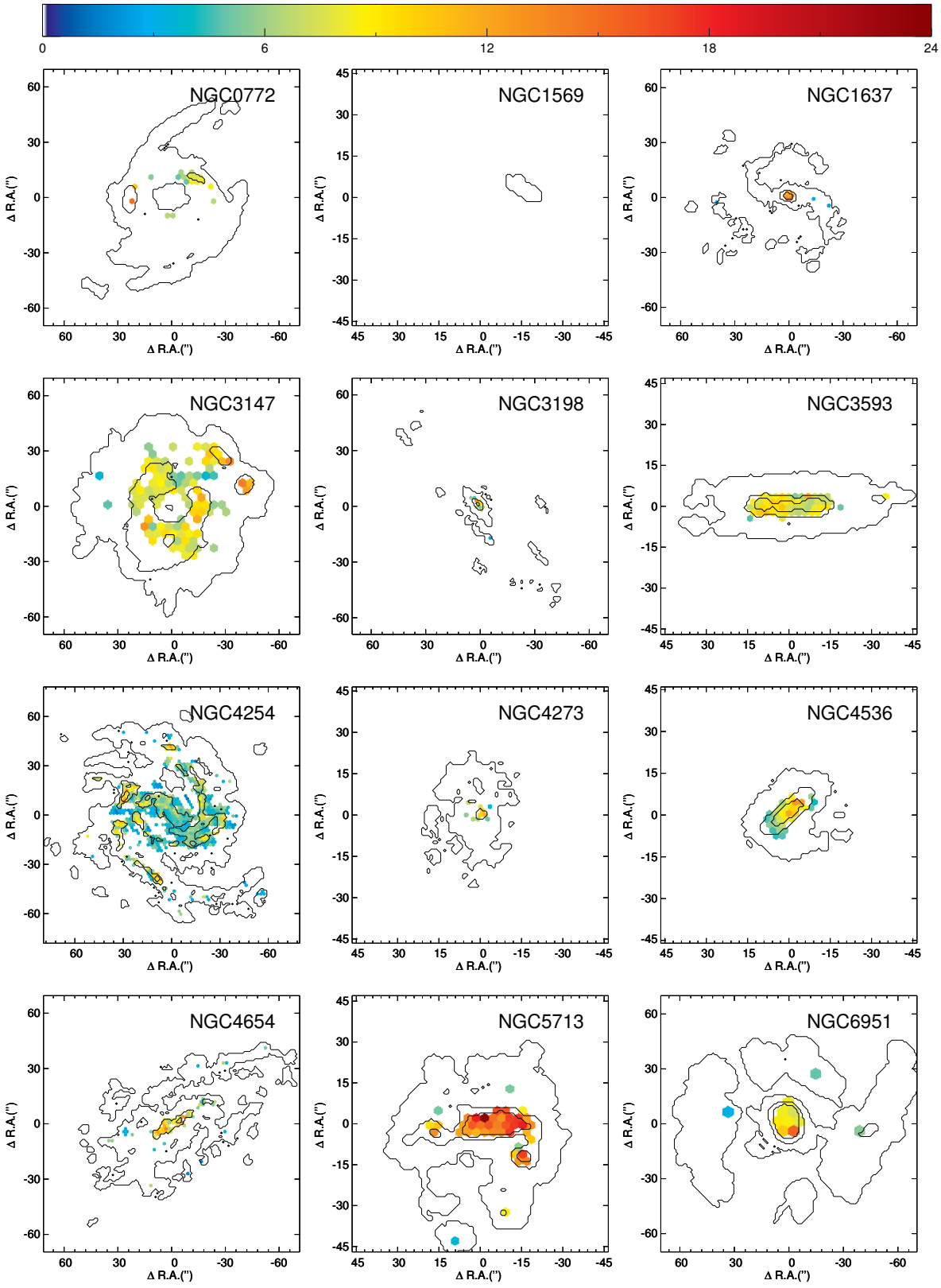

Figure 2.6. Maps of the ^{12}CO to ^{13}CO intensity ratio, $\mathcal{R}$, derived from ^{13}CO and ^{12}CO using the smoothed ^{12}CO mask (M12). Only half-beams with $\mathcal{R}$ detected at S/N > 3 are shown here. Black contours show ^{12}CO intensity with contour levels of $[3, 21, 39]$ times the ^{12}CO $\sigma_{\rm rms}$.

our galaxy sample does not include luminous mergers or starbursting galaxies, in which higher $\mathcal{R}$ and strong spatial variations in physical properties have been reported. On the other hand, our limited sensitivity to ^{13}CO emission confines the reliable $\mathcal{R}$ measurements to regions with stronger I_{13}, while regions with high $\mathcal{R}$ but weaker I_{13} might not appear in the $\mathcal{R}$ map. Moreover, our typical resolution of several hundred parsecs may smear out abnormal values of $\mathcal{R}$, and also make it difficult to identify rapid changes in $\mathcal{R}$ or gas properties that occur on scales of less than 100 pc (Meier & Turner, 2004).

2.3.3.3 Weighted mean ratios

Based on the resolved $\mathcal{R}$ maps, we computed a mean value for the intensity ratio in a galaxy, $\langle\mathcal{R}\rangle$, by taking the mean of resolved $\mathcal{R}$ for the ^{13}CO-detections weighted by their corresponding ^{13}CO intensities:

$$\langle\mathcal{R}\rangle = \frac{\sum_{i=1}^{\mathrm{Det}} I_{13,i}\mathcal{R}_i}{\sum_{i=1}^{\mathrm{Det}} I_{13,i}} = \frac{\sum_{i=1}^{\mathrm{Det}} I_{12,i}}{\sum_{i=1}^{\mathrm{Det}} I_{13,i}} \tag{2.2}$$

where i is a half-beam in the set of ^{13}CO-detections. The ^{13}CO intensity weighted mean $\mathcal{R}$, $\langle\mathcal{R}\rangle$, is thus the ratio of ^{12}CO and ^{13}CO fluxes for the ^{13}CO-detections. The $\langle\mathcal{R}\rangle$ value and the weighted standard deviation for each galaxy are listed in column (6) of Table 2.3. These $\langle\mathcal{R}\rangle$ values range between 5.3 ± 1.58 for NGC 4254 and 13.98 ± 2.9 for NGC 5713, with a typical value of $\sim$ 7–9. These values are similar to typical line ratios measured on (sub)-kpc scales (e.g. Paglione et al., 2001; Hirota et al., 2010; Wilson & Walker, 1994).

In Figure 2.7, we show a comparison between the weighted mean ratio $\langle\mathcal{R}\rangle$ and the flux ratio $F(^{12}\mathrm{CO})/F(^{13}\mathrm{CO})$ obtained in Section 2.3.3.1. The flux ratio of a galaxy is larger than the weighted mean $\langle\mathcal{R}\rangle$, because total flux ratios are calculated over all regions within the aperture, while $\langle\mathcal{R}\rangle$ is the flux ratio for the ^{13}CO-detections which have brighter ^{13}CO emission and are likely biased to lower $\mathcal{R}$ ratios. We consider this bias in greater detail in the following section.

2.3.4 Detection bias

In Figure 2.6, the resolved $\mathcal{R}$ measurements are available for much fewer regions than those with ^{12}CO-detections, leaving large numbers of half-beams within the ^{12}CO contours blank. For a half-

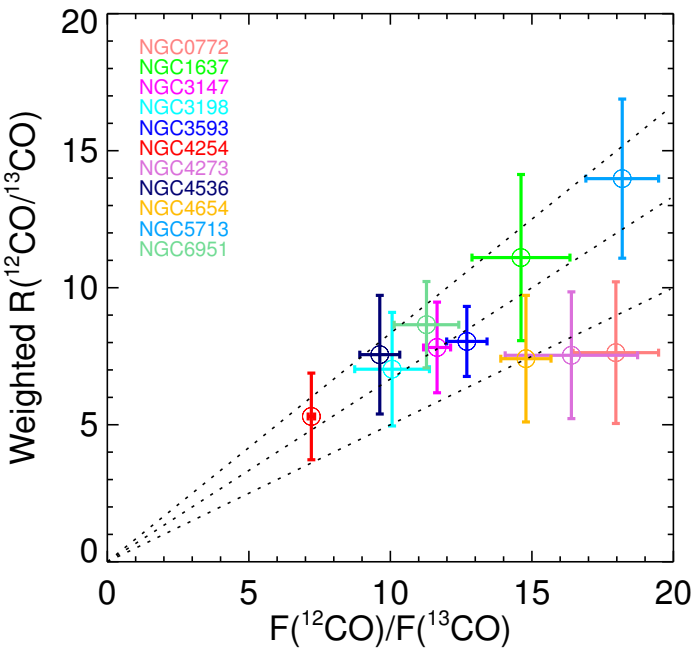

Figure 2.7. Weighted mean $\mathcal{R}$ as a function of integrated flux ratio $F(^{12}\mathrm{CO})/F(^{13}\mathrm{CO})$. Each colored point represents a galaxy from STING. The vertical error bars show the weighted standard deviation of $\mathcal{R}$, and the horizontal error bars show the uncertainty of $F(^{12}\mathrm{CO})/F(^{13}\mathrm{CO})$. The dashed lines show scaling factors of 1, 2 and 3 from the top to the bottom.

beam to be measured in $\mathcal{R}$, the typical S/N of ^{13}CO needs to be larger than 4; this threshold will select ^{12}CO-detections with S/N$(I_{12}) > 3\mathcal{R}$, as the typical $\sigma_{12} \sim 1.2\sigma_{13}$. Given LTE assumptions with T_k = 10 K, $[^{12}\mathrm{CO}]/[^{13}\mathrm{CO}]$= 40, and $\mathcal{R}\sim$ 8, the ^{12}CO-detections only require $N_{\mathrm{H_2}} > 3 \times 10^{20}\,\mathrm{cm}^{-2}$, while the $\mathcal{R}$ measurements require column densities 8 times larger. Moreover, the detection threshold also implies that the measured $\mathcal{R}$ has an upper limit of S/N$(I_{12})/3$, which can be quite restrictive in cases of low S/N. For a sample consisting mostly of ^{12}CO-detections without $\mathcal{R}$ detections, the resolved $\mathcal{R}$ are biased to lower values and should not be used to infer the mean or median $\mathcal{R}$ of the sample.

To quantify how the bias of $\mathcal{R}$ due to the limited detection threshold could affect our data, we show values of I_{12} and I_{13} of the resolved $\mathcal{R}$ measurements for each of the galaxies in Figure 2.8. Solid dots show individual half-beams with $\mathcal{R}$ measurements, and open circles show the mean value in each bin. Error bars on the circles show the 1σ scatter of the data. We further divide these mean values in two categories according to the detection fractions of the corresponding bin, defined as the ratio of the number of $\mathcal{R}$ detections to the number of ^{12}CO-detections. Red symbols represent

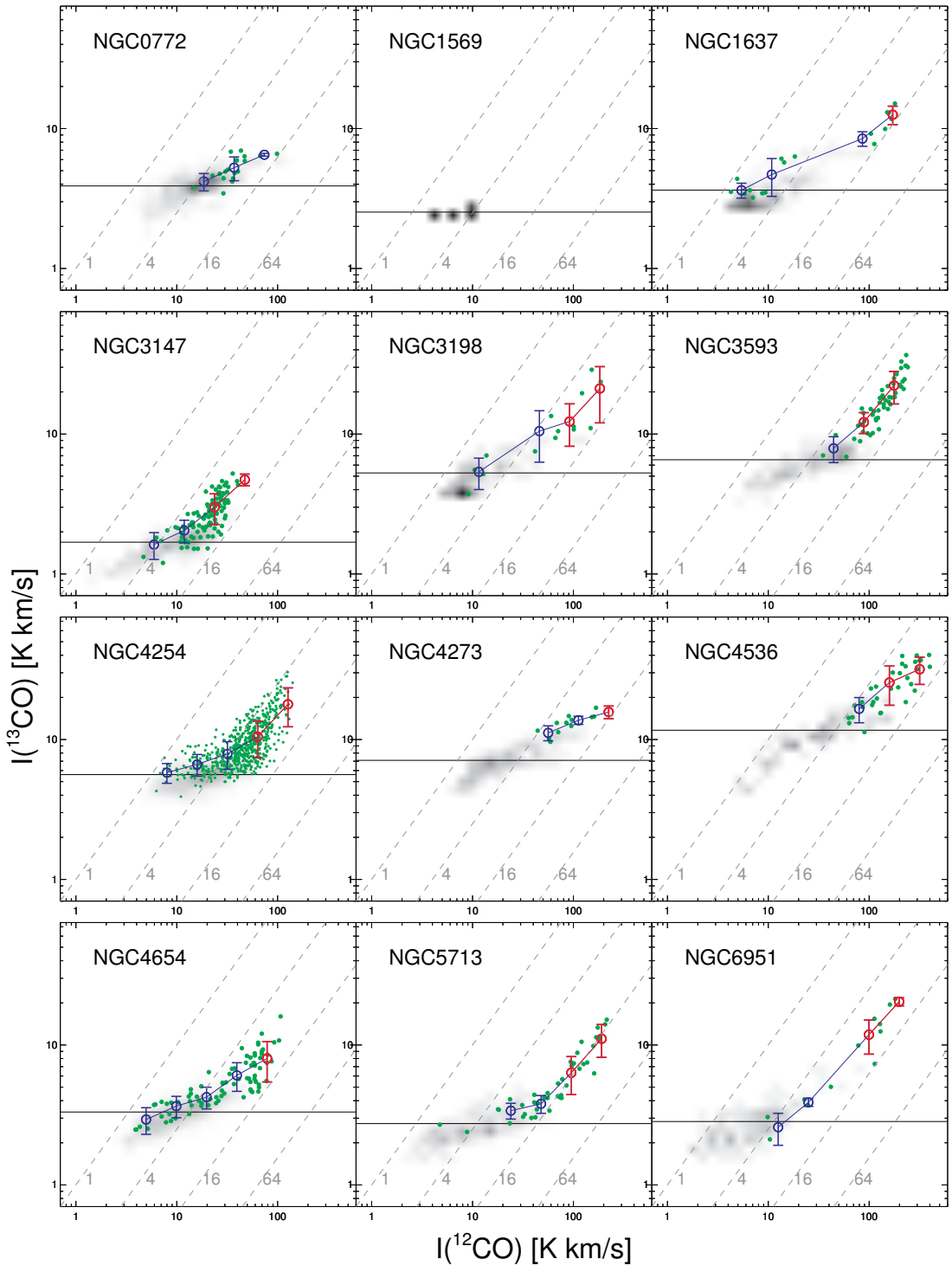

Figure 2.8. Intensity of the ^{13}CO emission as a function of the ^{12}CO emission of each galaxy. Green dots are the half-beams with ^{13}CO detections. Gray scales show the distribution of upper limits of ^{13}CO in the regions with ^{12}CO S/N$>$ 3 but without detectable ^{13}CO emission. All intensities are sampled onto half-beams defined in Section 2.3.1. The linked circles show the mean I_{13} value for ^{13}CO detections in each I_{12} bin, with red symbols representing the bins in which the number of ^{13}CO detections is more than 50% of all the half-beams. The error bars on the circles show the 1σ scatter. The horizontal solid line is the typical threshold of $3\sigma_{13}$, and the dashed lines show constant $\mathcal{R}$ of 1, 4, 16 and 64.

those with detection fraction greater than 50%, and blue ones show the bins with detection fraction below 50%. The horizontal solid line in each panel shows the detection threshold set by $3\sigma_{13}$; for simplicity, we use the typical value of σ_{13} of the galaxy from column 3 of Table 2.2. The gray shaded region show the upper limits of I_{13} inferred from $3\sigma_{13}$ for those half-beams below the detection threshold. For reference, we plot constant $\mathcal{R}$ values in the figure as dashed lines; $\mathcal{R}$ increases from the top left to the bottom right.

For the half-beams with resolved measurements, there appears a clear trend that the $\mathcal{R}$ are lower at the fainter end of I_{12}. However, the upper limit of $\mathcal{R}$, set by the detection threshold of $3\sigma_{13}$, also increases with I_{12} as S/N of I_{12} increases; the lower $\mathcal{R}$ measured in the low I_{12} regime could result from a selection effect as higher $\mathcal{R}$ values are not measurable.

To derive an estimate of $\mathcal{R}$ for the bins with a large fraction of half-beams below the detection threshold, we need to improve the S/N of ^{13}CO. In the following, we will first use spectral stacking to estimate the average ^{13}CO intensity for these bins. A toy model is then developed to provide one possible explanation of the distribution of I_{13} shown in our data.

2.3.4.1 Stacked line ratios

To compensate for the relatively low S/N of ^{13}CO which introduces a detection bias on resolved $\mathcal{R}$, we stack spectra of a number of half-beams to estimate their average line intensities and line ratios. By stacking spectra for N beams, we are able to increase the S/N of ^{13}CO by a factor of $\sqrt{N}$ and expand our analysis to a larger dynamic range. Only ^{12}CO-detections are used for stacking as their velocities can be well measured from ^{12}CO. The ^{12}CO and ^{13}CO spectra of each half-beam are shifted to a common velocity using its I_{12}-weighted mean velocity, and stacked with others based on physical properties such as galactic radii and SFRs. We fit both stacked spectral lines by Gaussian profiles to derive the integrated intensities. We use profile fitting because it does not require a predefined signal window for integration, and it can better extract the line emission rather than baseline structure. For each stacked ^{13}CO spectrum detected with peak S/N above 3, the stacked line ratio is calculated by taking the ratio of stacked integrated ^{12}CO and ^{13}CO intensities. When the stacked ^{13}CO intensity's peak S/N is below 3, the uncertainty of integrated ^{13}CO is calculated by integrating the channel noise over the FWHM of the stacked ^{12}CO. We use

3 times this uncertainty as the upper limit of ^{13}CO to derive the lower limit of stacked $\mathcal{R}$.

We first investigate the stacked line ratio as a function of I_{12}. We use logarithmic bins of I_{12} with a step of 0.3 dex. If two adjacent bins both have stacked I_{12} with S/N < 3, we merge them into one. Bin merging continues, in the direction of decreasing S/N, until the lower limit of $\mathcal{R}$ exceeds 10, the stacked line ratio has S/N > 3, or there are no more bins to merge. Figure 2.9 show the stacked spectra of NGC 4654 in I_{12} bins. The resulting stacked line ratios or their lower limits as a function of I_{12} are shown in Figure 2.10. The black circles show stacked $\mathcal{R}$ in each bin of ^{12}CO. The stacked $\mathcal{R}$ does not always increase with I_{12}, unlike the case for the resolved $\mathcal{R}$ of ^{13}CO-detections. In the bins with weaker I_{12} and a large fraction of ^{13}CO non-detections (corresponding lower limits are shown in gray scale), stacked $\mathcal{R}$ are higher than the individual ^{13}CO-detections; for these bins the ^{13}CO-detections are likely a biased sample from the overall population in the bin. The apparent increasing trend of resolved $\mathcal{R}$ with I_{12} seen in Figure 2.8 is mainly due to this detection bias in the lower I_{12} bins.

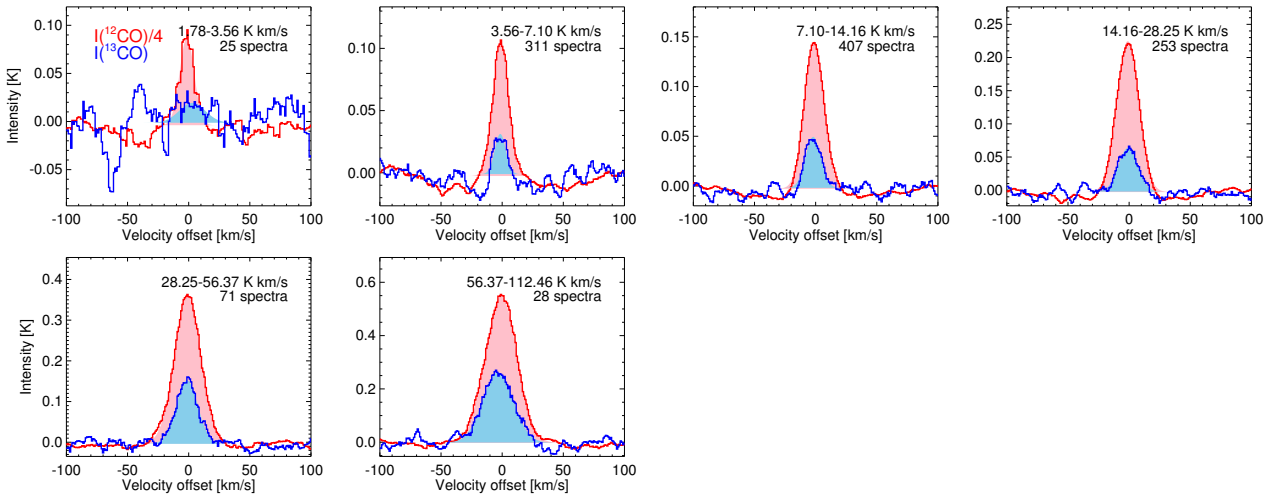

Figure 2.9. Stacked spectra of NGC 4654. The ranges of I_{12} bin and the numbers of the spectra used in the stacking are shown in the upper right corner of each panel. The blue lines are the ^{13}CO spectra and the red lines are the ^{12}CO spectra scaled by a factor of 5. The red and blue shaded regions show the Gaussian fitted integrated fluxes of ^{12}CO and ^{13}CO used for the stacked line ratios.

On the other hand, for the bins with stronger I_{12} and high detection fraction, resolved $\mathcal{R}$ are less biased and the stacked ratios are similar to the mean values. Filled color dots in each panel show the resolved $\mathcal{R}$ in bins for which detection fraction is more than 50% (the bins shown in red symbols in Figure 2.8). For these half-beams, the resolved $\mathcal{R}$ is less biased and does not strongly

depend on I_{12}.

2.3.4.2 A toy model

In nearby galaxies, I_{12} is measured on a much larger scale than a single GMC, so that brighter I_{12} in a beam also means more clouds are included; the scatter in $\mathcal{R}$ could decrease with I_{12} by averaging more clouds in a telescope beam. If all the resolved $\mathcal{R}$ detected consist of GMCs with similar properties and $\mathcal{R}$, it is possible that the dependence of resolved $\mathcal{R}$ on I_{12} results from applying detection thresholds on $\mathcal{R}$ with decreasing scatter. We have developed a simple model as described below to test this possibility.

We divide the molecular gas in a galaxy into small scale parcels ("cloudlets") each emitting the same amount of ^{12}CO ($I_{12}^{\rm cl}$), so the I_{12} we measure in a half-beam is a proxy for the number of cloudlets in it. We assume that the ^{13}CO emission of each cloudlet ($I_{13}^{\rm cl}$) in the galaxy is drawn from the same probability distribution and is independent of other cloudlets. We use $I_{12}^{\rm cl}$ and $I_{13}^{\rm cl}$ to represent the ^{12}CO and ^{13}CO intensities of a single cloudlet, as opposed to other quantities without an upper index representing measurements over a half-beam. The inverse of $\mathcal{R}$ is then the average of $I_{13}^{\rm cl}/I_{12}^{\rm cl}$ over all the cloudlets in a half-beam:

$$\frac{1}{\mathcal{R}} = \frac{\sum_{i=1}^{N} I_{13}^{\rm cl}}{N I_{12}^{\rm cl}} = \frac{\langle I_{13}^{\rm cl} \rangle}{I_{12}^{\rm cl}} = \left\langle \frac{1}{\mathcal{R}^{\rm cl}} \right\rangle, \tag{2.3}$$

where $\mathcal{R}$ is the line ratio for a half-beam, N is the number of cloudlets in the half-beam, and $\mathcal{R}^{\rm cl}$ is the ratio of a single cloudlet. For independent and identically distributed $1/\mathcal{R}^{\rm cl}$ ($I_{13}^{\rm cl}/I_{12}^{\rm cl}$), $1/\mathcal{R}$ of a half-beam, as the average value of $1/\mathcal{R}^{\rm cl}$ for the N cloudlets in it, will have the same expectation as $1/\mathcal{R}^{\rm cl}$ and remain constant throughout the galaxy. Meanwhile, the variance of $1/\mathcal{R}$ for a half-beam will be the variance of $1/\mathcal{R}^{\rm cl}$ divided by the number of cloudlets N the half-beam contains. To implement the model and compare it with the data, we logarithmically binned all the half-beams with ^{12}CO S/N > 3 detections according to their I_{12}. We choose the bin with the highest ^{12}CO intensity as the reference bin, because ^{13}CO measurements in that bin are the least biased by sensitivity. We measured the mean and variance of $1/\mathcal{R}$ in the reference bin as $I_{13,\rm ref}/I_{12,\rm ref}(1/\mathcal{R}_{\rm ref})$ and $S_{\rm ref}^2$. For half-beams with a given I_{12}, the expectation and variance of

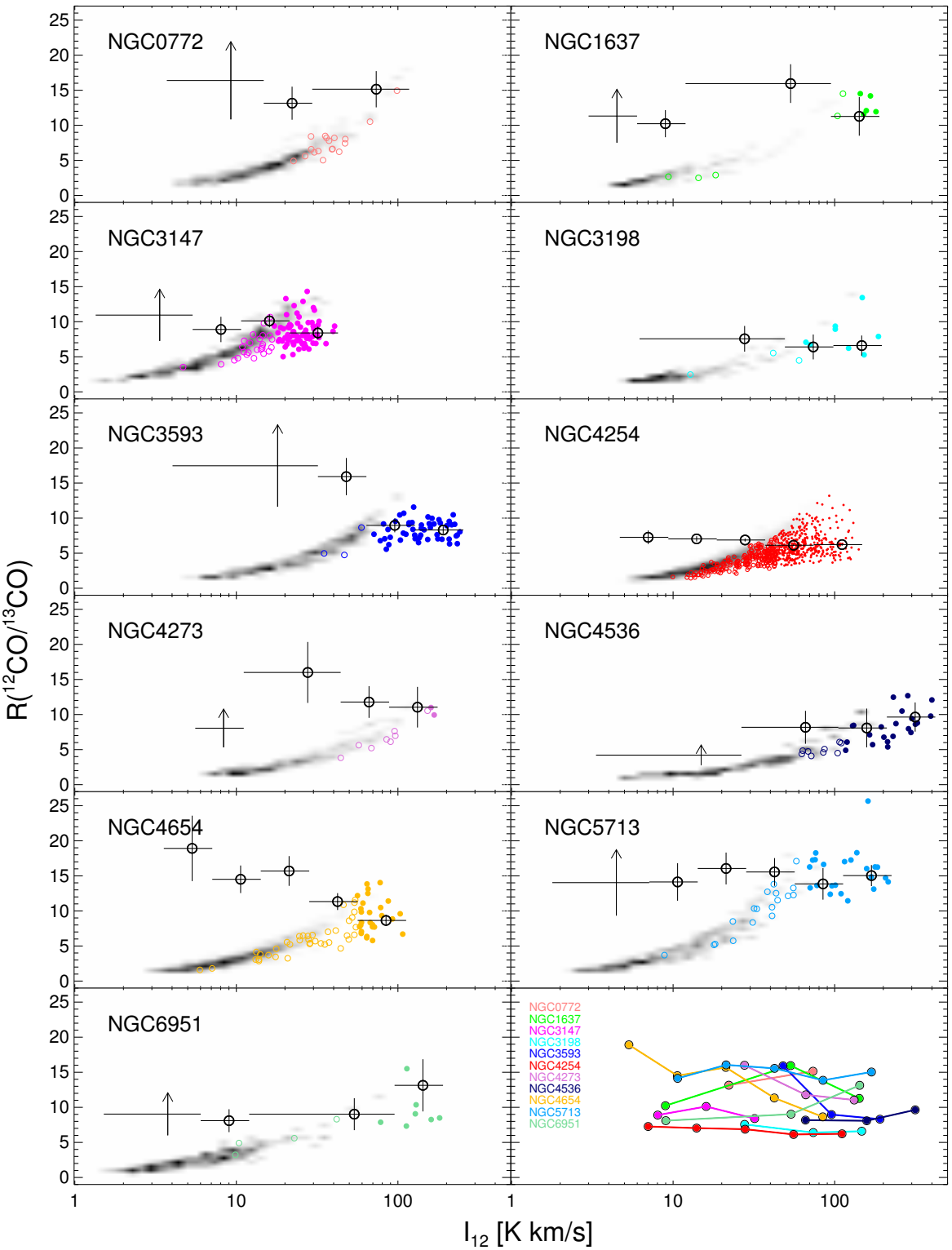

Figure 2.10. Resolved and stacked $\mathcal{R}$ as a function of I_{12}. The first 11 panels show the results for each individual galaxy, excluding NGC 1569. Small colored circles show the ratios for individual half-beams with $\mathcal{R}$ detected; the filled ones show the half-beams in I_{12} bins with detection fraction greater than 50%, and the open ones show the half-beams in I_{12} bins with lower detection fraction. The gray scales show the distribution of $\mathcal{R}_{\rm min} = I_{12}/3\sigma_{13}$ for half-beams with ^{12}CO detected but $\mathcal{R}$ not detected. The black large circles and arrows are the stacked $\mathcal{R}$ and lower limits in each I_{12} bin respectively; the horizontal error bars reflect the bin size, and the vertical error bars show their uncertainties. The last panel is a summary plot showing stacked $\mathcal{R}$ with different colors representing different galaxies.

$1/\mathcal{R}$ are:

$$E\left[\frac{1}{\mathcal{R}}\right] = \frac{I_{13,\mathrm{ref}}}{I_{12,\mathrm{ref}}} = \frac{1}{\mathcal{R}_{\mathrm{ref}}}, \tag{2.4}$$

$$\mathrm{Var}\left[\frac{1}{\mathcal{R}}\right] = S^2_{\mathrm{ref}} \frac{I_{12,\mathrm{ref}}}{I_{12}}. \tag{2.5}$$

Moreover, by the central limit theorem, I_{13}/I_{12} of a half-beam, as the mean of a number of independent $1/\mathcal{R}_{\mathrm{cl}}$, will tend to be normally distributed if the half-beam contains a sufficiently large number of cloudlets. Besides the intrinsic scatter of $1/\mathcal{R}$ assumed by the toy model, we also include measurement uncertainties using typical values of σ_{13} of the galaxy from column 3 of Table 2.2 into the toy model. In our approach, we model the half-beams in NGC 4254 only if they have I_{12} above a lower limit of 20 K km s^{-1}, which corresponds to approximately 500 cloudlets each with a typical mass of 10^4 $M_\odot$ using a standard CO-to-H_2 conversion factor of $X_{\mathrm{CO}} = 2 \times 10^{20}$ cm^{-2}(K km s^{-1})$^{-1}$. Aside from the deviation from a normal distribution due to the small number of cloudlets, for half-beams with I_{12} under the limit of 20 K km s^{-1}, measurement errors in I_{12} introduce an additional source of scatter in $1/\mathcal{R}$ that is not included in the model. Therefore, we only model the distribution of $1/\mathcal{R}$ for each single half-beam with $I_{12} > 20$ K km s^{-1}, including both ^{13}CO detections and non-detections.

In Figure 2.11, we show the results of such an approach for NGC 4254 for illustration. NGC 4254 has the largest number of ^{13}CO-detections in our sample of galaxies, providing the most data points for estimating the statistical properties of the reference bin ($1/\mathcal{R}$ and S_{ref}) used in the model. The upper panel shows I_{13} as a function of I_{12}. The gray points are the measured I_{13} detected where both ^{12}CO and ^{13}CO have S/N > 3. The black square symbol shows the reference I_{12} bin ($I_{12,\mathrm{ref}}$) in which we measure $I_{13,\mathrm{ref}}/I_{12,\mathrm{ref}}$ and S_{ref}, with the vertical error bar showing the standard deviation of I_{13} and the horizontal error bar showing the I_{12} bin size. The other 2 bins with all the half-beams detected in ^{13}CO are shown as black filled circles. All these bins show similar mean $\mathcal{R}$ to the constant mean value of $\mathcal{R}$ indicated by the dashed line in the plot. We use a black dotted line to show the detection threshold of $3\sigma_{13}$. The red shaded band spans the 1σ distribution of the I_{13} we expect in the model. By comparison, we use a blue shaded band to show the 1σ distribution of I_{13} when only including the measurement uncertainty into the constant $\mathcal{R}$ without intrinsic scatter.

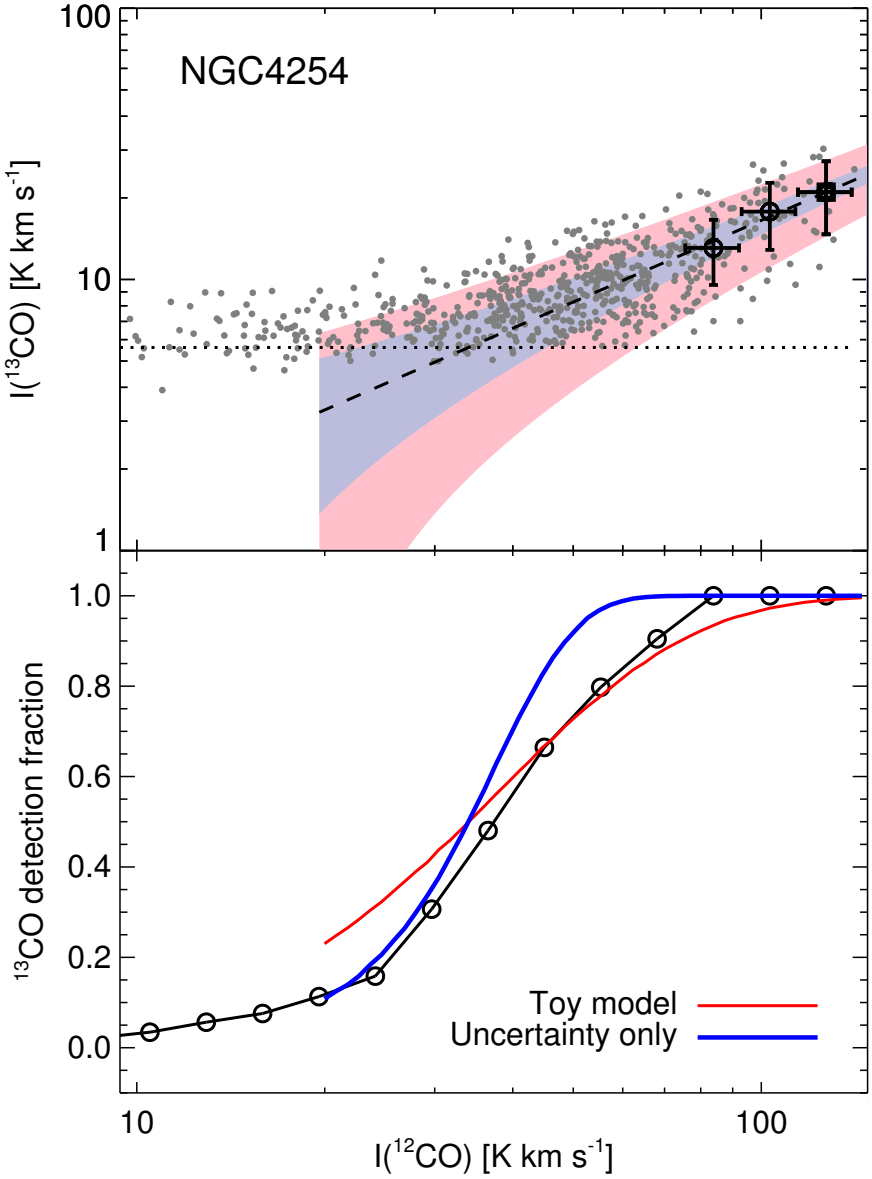

Figure 2.11. Comparison of the observed I_{13} and its detection fraction in NGC 4254 with a toy model. *Upper panel*: I_{13} as a function of I_{12}. The gray points show half-beams with I_{13} detected above $3\sigma_{13}$. The black square symbol shows the mean I_{13} of the reference bin chosen for measuring $1/\mathcal{R}_{\rm ref}$ and $S_{\rm ref}$, and the black filled circles with error bars show I_{13} of the other 2 bins in which all the half-beams are detected in both ^{13}CO and ^{12}CO; horizontal and vertical error bars on these symbols show the width and standard deviation of each bin respectively. The dashed line shows the constant $\mathcal{R}$ assumed by the model. The dotted black line shows the detection threshold set by 3 times the mean sensitivity of ^{13}CO. The red shaded band shows the range of standard deviation of the toy model, and the blue shaded band shows the measurement uncertainty of I_{13} assuming a constant $\mathcal{R}$. *Lower panel*: Detection fraction of ^{13}CO as a function of I_{12}. The circles show detection fractions of ^{13}CO with S/N > 3 from observation. The red line shows the detection fractions predicted by the toy model, and the blue line shows the detection fractions obtained by assuming the scatter on $\mathcal{R}$ is entirely from the measurement uncertainty.

In the high I_{12} regime, the distribution of the detected I_{13} looks very similar to the prediction of the toy model. In the low I_{12} regime, the detected I_{13} values are located at the upper end of the modeled distribution. Although individually these detections seem to deviate from the average I_{13} of the model shown as the dashed line, their distribution is still close to the 1σ envelope of the modeled distribution. In contrast, the measurement uncertainty shown in the blue band is smaller than the observed scatter measured in the three bins with highest I_{12}, and many of the individual detections with lower I_{12} are also outside of the envelope. Including measurement uncertainty only does not reproduce the observed I_{13} distribution very well.

For each I_{12} bin, we further compare the observed ^{13}CO detection fraction with the fraction of ^{13}CO measurements predicted by the model to be above the detection threshold. The black circles in the lower panel are the detection fractions from the data with S/N > 3. The red solid line shows the detection fraction of the model by setting a detection threshold of $3\sigma_{13}$, i.e. the fraction of modeled ^{13}CO above the dotted line in the upper panel. The detection fraction calculated for constant $\mathcal{R}$ with measurement uncertainties is shown in blue. As the figure shows, the toy model predicts very similar detection fractions to the observations, while a model which only includes the measurement uncertainty shows detection fractions less favored by the data. The success of the toy model in predicting the detection fraction over a factor of 10 in I_{12} suggests that dependence of resolved $\mathcal{R}$ on I_{12} can result primarily from a combination of intrinsic scatter and detection bias.

2.4 Results

2.4.1 Line ratio as a function of galaxy properties

The STING sample spans a range of galaxy properties, such as stellar mass, star-formation rate, and morphology. Before examining the spatially resolved $\mathcal{R}$ in each galaxy, we first compare the global line ratios among the sample galaxies, to study the dependence of line ratios on galaxy properties. For each property, we first investigate the flux ratio $F(^{12}\mathrm{CO})/F(^{13}\mathrm{CO})$, which is determined by the gas content of the entire galaxy. We then study the ^{13}CO intensity weighted mean ratio $\langle\mathcal{R}\rangle$ that represents the typical value of the resolved $\mathcal{R}$ on (sub-)kpc scales.

2.4.1.1 Dust temperature

We plot the flux ratio $F(^{12}\mathrm{CO})/F(^{13}\mathrm{CO})$ as a function of *IRAS* IR colors F_{60}/F_{100} in the left panel of Figure 2.12, together with the data from Crocker et al. (2012). For F_{60}/F_{100} between 0.2 and 0.6, we do not find a strong correlation between $F(^{12}\mathrm{CO})/F(^{13}\mathrm{CO})$ and F_{60}/F_{100}. In previous studies, although a positive correlation between the two parameters has been claimed, for $F_{60}/F_{100} \lesssim 0.6$, the correlation is tentative and shows large scatter (Young & Sanders, 1986; Aalto et al., 1995; Sage & Isbell, 1991; Crocker et al., 2012). A recent survey of ^{13}CO in normal galaxies by Vila-Vilaro et al. (2015) also found no correlation between $F(^{12}\mathrm{CO})/F(^{13}\mathrm{CO})$ and F_{60}/F_{100}. Our results are in agreement with these studies.

The F_{60}/F_{100} ratio is often considered as an indicator of dust temperature. A higher dust temperature might be associated with a higher gas temperature, which would reduce the average opacity of ^{12}CO and increase $F(^{12}\mathrm{CO})/F(^{13}\mathrm{CO})$. A higher dust temperature also implies the galaxy has more active star formation, which may increase the fraction of gas in a diffuse molecular phase (with low opacity and high $\mathcal{R}$) through feedback. There is also the possibility that chemical fractionation towards ^{13}CO at lower dust temperatures results in low $\mathcal{R}$ at low F_{60}/F_{100} (Crocker et al., 2012). All of these effects could lead to a positive correlation between $F(^{12}\mathrm{CO})/F(^{13}\mathrm{CO})$ and dust temperature. However, our results show no such correlation for $F_{60}/F_{100} \sim 0.2 - 0.6$; the effect of dust temperature on the line ratio is not prominent.

The right panel of Figure 2.12 shows that the ^{13}CO intensity weighted mean ratio $\langle\mathcal{R}\rangle$ also shows little dependence on F_{60}/F_{100}. For a galaxy with higher dust temperature and thus higher star formation rate on average, systematically lower optical depth of ^{12}CO in molecular clouds might result from star formation heating the gas and/or broadening the line width. Therefore, a positive correlation is expected if such opacity effects determine the resolved $\mathcal{R}$. Our results suggest that systematic differences in resolved $\mathcal{R}$ cannot be attributed to different dust temperatures.

2.4.1.2 Inclination

The galaxy inclination may affect line ratios by changing the column density along the line-of-sight. Highly inclined galaxies will have larger average optical depth than face-on galaxies, and thus lower $F(^{12}\mathrm{CO})/F(^{13}\mathrm{CO})$, unless line broadening due to rotation reduces the optical depth per velocity

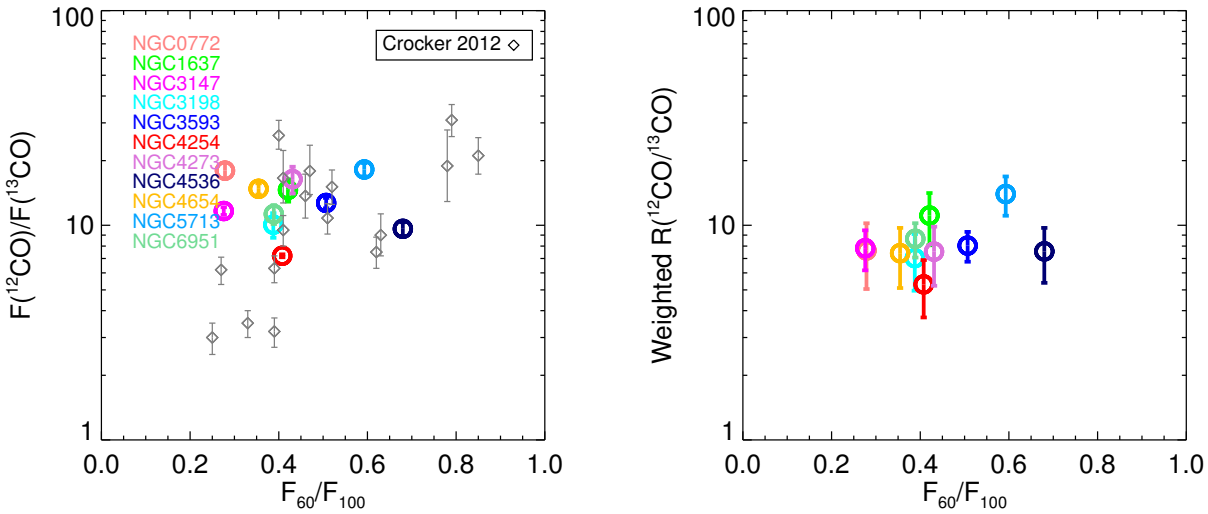

Figure 2.12. *Left*: Flux ratio $F(^{12}\mathrm{CO})/F(^{13}\mathrm{CO})$ vs. the far-IR flux ratio at 60 and 100 μm (F_{60}/F_{100}), with the color circles representing the STING galaxies and the black diamonds showing samples from Crocker et al. (2012). For the STING galaxies, the vertical error bars show the uncertainty in the flux ratio. *Right*: ^{13}CO intensity weighted mean ratio $\langle\mathcal{R}\rangle$ vs. F_{60}/F_{100}. The vertical error bars show the ^{13}CO intensity weighted standard deviation of $\mathcal{R}$.

channel. However, there is no such negative correlation between $F(^{12}\mathrm{CO})/F(^{13}\mathrm{CO})$ and galaxy inclination, as shown in the left panel of Figure 2.13. The results are consistent with previous findings by Young & Sanders (1986) and Sage & Isbell (1991), which also suggest that inclination has no effect on the large-scale line ratio.

For the resolved $\mathcal{R}$, the number of molecular clouds within a beam will increase with the inclination. Therefore, $\mathcal{R}$ in more inclined galaxies will be measured by averaging more clouds than in face-on galaxies, leading to less variations of $\mathcal{R}$ within the galaxy. We present the weighted mean ratio $\langle\mathcal{R}\rangle$ as a function of inclination in the right panel of Figure 2.13. The typical resolved $\mathcal{R}$ of a galaxy does not show a dependence on the galaxy's inclination; there is also no strong effect of inclination on (sub-)kpc scales. The error bars show the standard deviation of resolved $\mathcal{R}$, and we do not find a correlation between the standard deviation of $\mathcal{R}$ and the inclination. This differs from the finding by Sage & Isbell (1991) who found that the variance of the line ratio is larger in face-on galaxies. However, note that the standard deviation of $\mathcal{R}$ we calculate includes only the ^{13}CO-detections, which might underestimate the spatial variance of $\mathcal{R}$ in the galaxy (c.f. Figure 2.11).

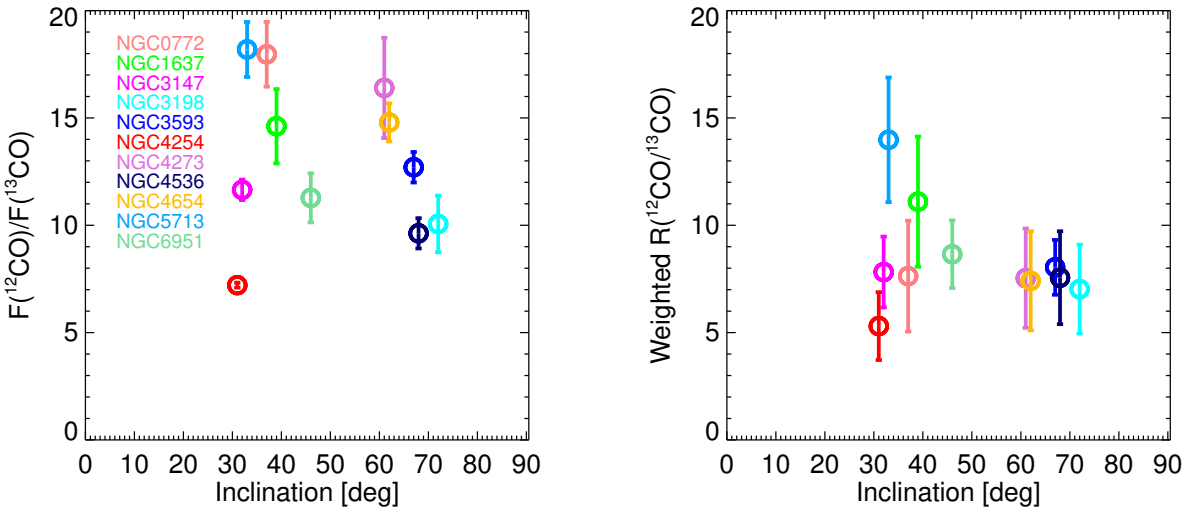

Figure 2.13. *Left*: Flux ratio $F(^{12}\mathrm{CO})/F(^{13}\mathrm{CO})$ as a function of galaxy inclination. The vertical error bars show the uncertainty in the flux ratio. *Right*: ^{13}CO intensity weighted mean ratio $\langle\mathcal{R}\rangle$ as a function of galaxy inclination. The vertical error bars show the intensity weighted standard deviation of $\mathcal{R}$.

2.4.1.3 Metallicity

In the left panel of Figure 2.14, we show the flux ratio $F(^{12}\mathrm{CO})/F(^{13}\mathrm{CO})$ as a function of gas-phase metallicity. Although our sample spans a considerable range in metallicity, there is no clear evidence that $F(^{12}\mathrm{CO})/F(^{13}\mathrm{CO})$ is directly correlated with metallicity. This is in agreement with previous studies using larger samples (Sage & Isbell, 1991; Crocker et al., 2012). Theoretically, an anti-correlation between $F(^{12}\mathrm{CO})/F(^{13}\mathrm{CO})$ and metallicity is expected: in metal-poor galaxies, because ^{12}CO should be less abundant, the average optical depth of ^{12}CO emission will be reduced and thus $F(^{12}\mathrm{CO})/F(^{13}\mathrm{CO})$ will be elevated. However, this expectation assumes a single-component LTE model, which is probably too simplistic to apply to a galaxy as a whole. ^{13}CO and ^{12}CO very likely originate from different structures in the line of sight: ^{13}CO should emit from a deeper layer than the well-shielded ^{12}CO. In low metallicity environments, ^{12}CO is less effectively shielded so its emitting area shrinks (e.g. Wolfire et al., 2010), while ^{13}CO in denser regions might be less affected. Therefore, the increase of the flux ratio $F(^{12}\mathrm{CO})/F(^{13}\mathrm{CO})$ for a metal-poor galaxy may be less than expected.

Metallicity could also affect the line ratios through changes in $[^{12}\mathrm{C}]/[^{13}\mathrm{C}]$. As ^{13}C is produced mainly by intermediate-mass stars and accumulates slowly as a galaxy evolves, in low metallicity environments where gas is less processed, under-abundant ^{13}C and hence a higher

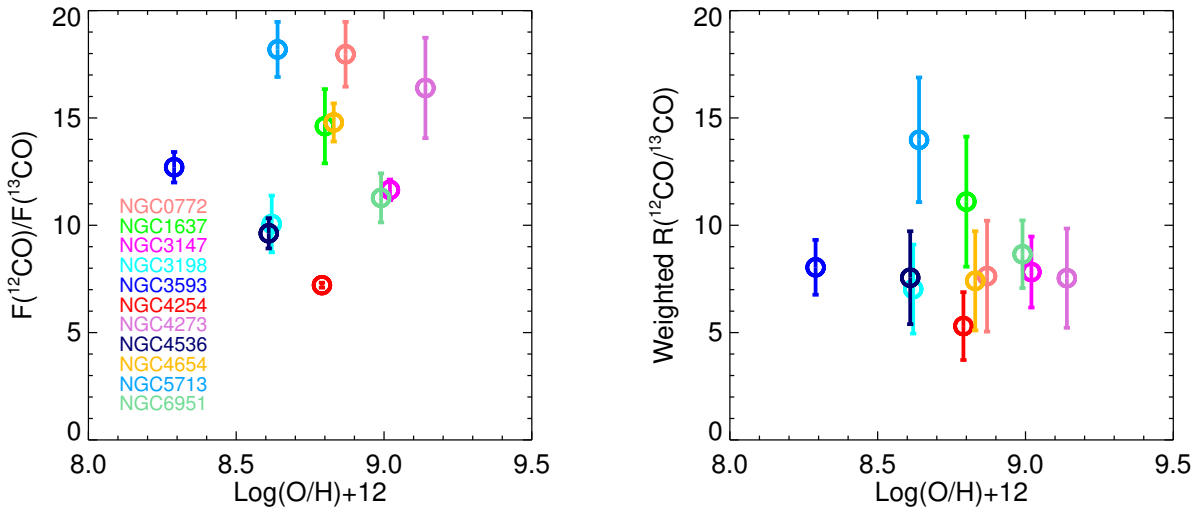

Figure 2.14. *Left*: Flux ratio $F(^{12}\mathrm{CO})/F(^{13}\mathrm{CO})$ as a function of galaxy metallicity. The vertical error bars show the uncertainty in the flux ratio. The references for metallicity are listed in Table 2.1. *Right*: $^{13}\mathrm{CO}$ intensity weighted mean ratio $\langle\mathcal{R}\rangle$ as a function of galaxy metallicity. The vertical error bars show the intensity weighted standard deviation of $\mathcal{R}$.

fractional abundance $[^{12}\mathrm{C}/^{13}\mathrm{C}]$ will also tend to increase $F(^{12}\mathrm{CO})/F(^{13}\mathrm{CO})$ as well as the resolved $\mathcal{R}$. $F(^{12}\mathrm{CO})/F(^{13}\mathrm{CO})$ and the weighted mean ratio $\langle\mathcal{R}\rangle$ are both expected to anti-correlate with metallicity if $[^{12}\mathrm{C}/^{13}\mathrm{C}]$ decreases with increasing metallicity. However, as shown in Figure 2.14, $F(^{12}\mathrm{CO})/F(^{13}\mathrm{CO})$ or $\langle\mathcal{R}\rangle$ does not depend on metallicity in our sample. There are several possible reasons for this discrepancy between the observed results and these expectations. First of all, because there are only a few direct measurements of $[^{12}\mathrm{C}/^{13}\mathrm{C}]$ reported, the relation between the fractional abundance and metallicity remains unclear. One unanticipated finding was that $[^{12}\mathrm{C}/^{13}\mathrm{C}]$ of clouds in the Small and the Large Magellanic Clouds is similar to that of Milky Way clouds (Heikkilä et al., 1999). In addition, the impact of $[^{12}\mathrm{C}/^{13}\mathrm{C}]$ on $F(^{12}\mathrm{CO})/F(^{13}\mathrm{CO})$ and $\langle\mathcal{R}\rangle$ could still be very limited or even washed-out by the other factors that change the opacity, such as has been found in the Milky Way: while $[^{12}\mathrm{C}/^{13}\mathrm{C}]$ has a positive radial gradient in distance from the Galactic center (Milam et al., 2005), $\mathcal{R}$ varies from ~ 10 in the Galactic center (Bally et al., 1987; Martin et al., 2004) to ~ 6 in Galactocentric radius range of $3-6$ kpc (Roman-Duval et al., 2016)

2.4.1.4 Significance of trends

In addition to these three properties, we also tested for a correlation between the line ratio and the stellar mass of the galaxy. The flux ratio and the weighted mean ratio as functions of stellar mass are shown in Figure 2.15. No strong trend between $\mathcal{R}$ and stellar mass was found in our sample.

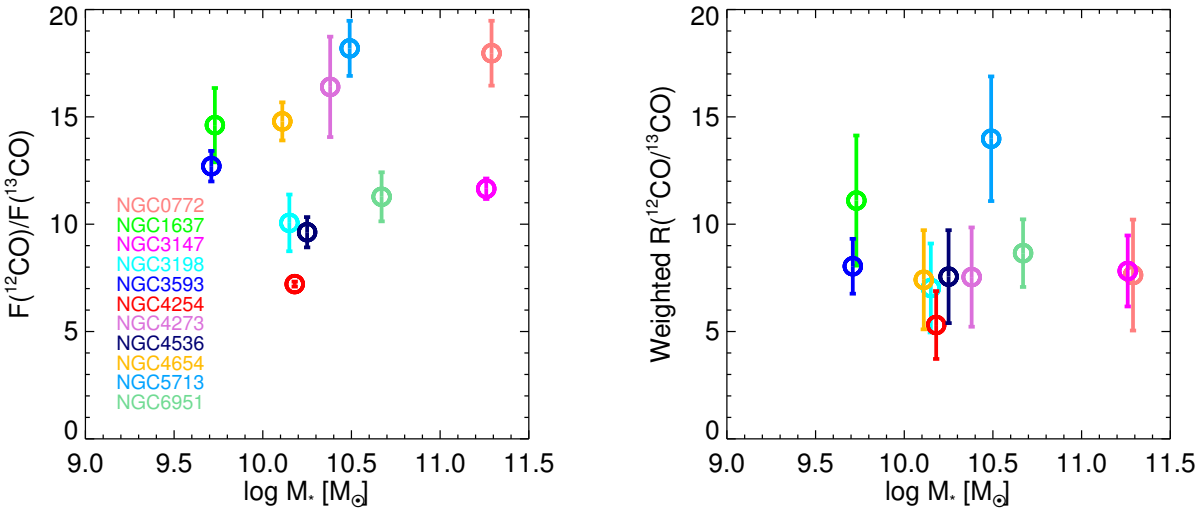

Figure 2.15. *Left*: Flux ratio $F(^{12}\mathrm{CO})/F(^{13}\mathrm{CO})$ as a function of stellar mass of the galaxy. The vertical error bars show the uncertainty in the flux ratio. *Right*: ^{13}CO intensity weighted mean ratio $\langle\mathcal{R}\rangle$ as a function of stellar mass. The vertical error bars show the intensity weighted standard deviation of $\mathcal{R}$.

In Table 3.3, we list the Spearman rank correlation coefficients (r_s) between the line ratios and each galaxy property we have investigated, and the significance of its deviation from zero (P_0). The significance P_0 represents the probability assigned to the hypothesis that the variables are unrelated; a lower P_0 means a more significant correlation. For our sample of 11 galaxies, we expect a significant correlation when $|r_s| > 0.8$ and $P_0 < 0.05$. The results shown in Table 3.3 further confirm the lack of strong trends between ^{12}CO/^{13}CO line ratios the galaxy's dust temperature, inclination, and metallicity.

2.4.2 Variations of spatially resolved line ratio

In this section, we investigate the variations of resolved $\mathcal{R}$ within each galaxy as measured in half-beam width apertures. Both of the stacked and resolved $\mathcal{R}$ are analyzed. The stacked intensities and line ratios are derived following the same approach described in Section 2.3.4.1. In Figure 2.16,

Table 2.4. Line ratio and galaxy properties of the STING sample

Galaxy property	$F(^{12}\mathrm{CO})/F(^{13}\mathrm{CO})$		$\langle\mathcal{R}\rangle$	
	r_s [a]	P_0 [b]	r_s [c]	P_0 [d]
F_{60}/F_{100} [e]	0.27	0.42	−0.02	0.96
Inclination	−0.17	0.61	−0.22	0.52
$\log \mathrm{O/H} + 12$	0.32	0.34	0.01	0.98
$\log M_*$ [f]	0.07	0.84	0.09	0.80

[a]Spearman's rank correlation coefficients between $F(^{12}\mathrm{CO})/F(^{13}\mathrm{CO})$ and galaxy properties.

[b]Probability of the null hypothesis of no correlation between $F(^{12}\mathrm{CO})/F(^{13}\mathrm{CO})$ and galaxy properties.

[c]Spearman's rank correlation coefficients between $\langle\mathcal{R}\rangle$ and galaxy properties.

[d]Probability of the null hypothesis of no correlation between $\langle\mathcal{R}\rangle$ and galaxy properties.

[e]The 60 μm and 100 μm fluxes are from NED.

[f]Stellar masses are derived from from 3.6μm luminosity using Equation C1 in Leroy et al. (2008).

we show the spectra of NGC 4654 stacked by radius. The stacked line ratios are used for studying the mean trends. Since we restrict the stacking to places where resolved ^{12}CO is well detected, the stacked spectra will tend to overestimate the mean ^{12}CO and yield a higher line ratio if the bin also includes significant number of ^{12}CO non-detections. Therefore, we excluded the bins in which ^{12}CO-detections number less than ^{12}CO-non-detections. For quantifying the resolved correlations between $\mathcal{R}$ and other local properties, we only use the half-beams in bright I_{12} bins for which detection fraction is more than 50% (the bins shown in red symbols in Figure 2.8), since these resolved $\mathcal{R}$ do not strongly depend on I_{12} and are less affected by the sensitivity bias.

2.4.2.1 Radial dependence

The radial distribution of $\mathcal{R}$ has been studied in previous works, but their findings do not offer a consistent picture. In the Milky Way, Roman-Duval et al. (2016) found that $\mathcal{R}$ increases with galactocentric distance. While Rickard & Blitz (1985) and Paglione et al. (2001) claimed $\mathcal{R}$ is generally higher in the central regions than the disks in their surveys, there are a handful of galaxies showing constant radial profiles (Young & Sanders, 1986; Sage & Isbell, 1991), and others showing $\mathcal{R}$ increasing with radius (e.g. M51, Pety et al., 2013).

Figure 2.17 shows the resolved and stacked $\mathcal{R}$ as functions of galactocentric radii. The resolved

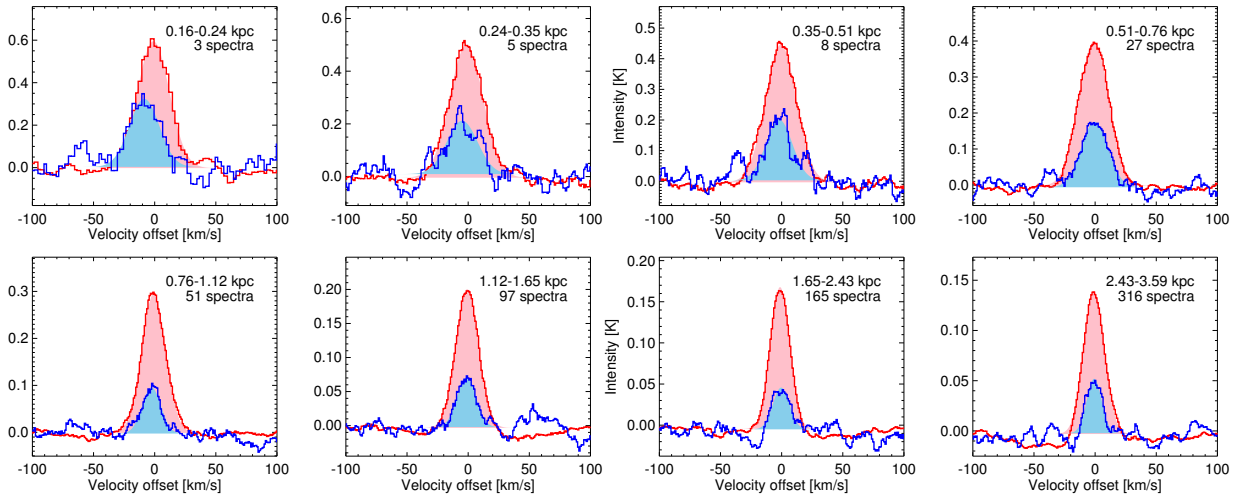

Figure 2.16. Stacked spectra of NGC 4654 at different radii. The ranges of radius bin and the numbers of the spectra used in the stacking are shown in the upper right corner of each panel. The blue lines are the ^{13}CO spectra and the red lines are the ^{12}CO spectra scaled by a factor of 5. The red and blue shaded regions show the Gaussian fitted integrated fluxes of ^{12}CO and ^{13}CO used for the stacked line ratios.

$\mathcal{R}$ are shown in the plot by individual colored points, while the distribution of lower limits for non-detections are shown in gray shading. We binned the galactocentric radii into equal bins in log space and adjusted them until $\mathcal{R}$ in each stacked bin has S/N$>$ 3 or the stacked lower limit exceeds 10. The open circles show stacked $\mathcal{R}$ in each bin. The colored dots show the $\mathcal{R}$ detections. Filled color dots in each panel show the half-beams in bright I_{12} bins used to measure the correlation coefficients, and we require more than 20 such half-beams in a galaxy for the measurement. We show Spearman's correlation coefficient r_s and the significance level (P_0) of the null hypothesis in the top right of each panel. We expect a significant correlation when $|r_s| > 0.6$ and $P_0 < 0.05$. The gray shading shows the lower limits of $\mathcal{R}$ derived by using upper limits of I_{13} for the non-detections.

Of 6 galaxies with correlation coefficients available, only NGC 4536 exhibits a clear trend with radius, in the sense that $\mathcal{R}$ decreases with radius. Such radial trends are often found in starbursting galaxies (e.g. Aalto et al., 2010; Tosaki et al., 2002; Hirota et al., 2010). NGC 4536 also has a starburst center (e.g. Davies et al., 1997); it is possible that the overall higher temperature in starbursting galaxies could generate a strong enough gradient in temperature and ^{13}CO optical depth to produce an observable trend in $\mathcal{R}$ compared to other galaxies . The higher temperature might also account for the higher fluxes of ^{12}CO ($J = 2 \rightarrow 1$) compared ^{12}CO ($J = 1 \rightarrow 0$) spectra near the systemic velocity shown in Figure 2.5.

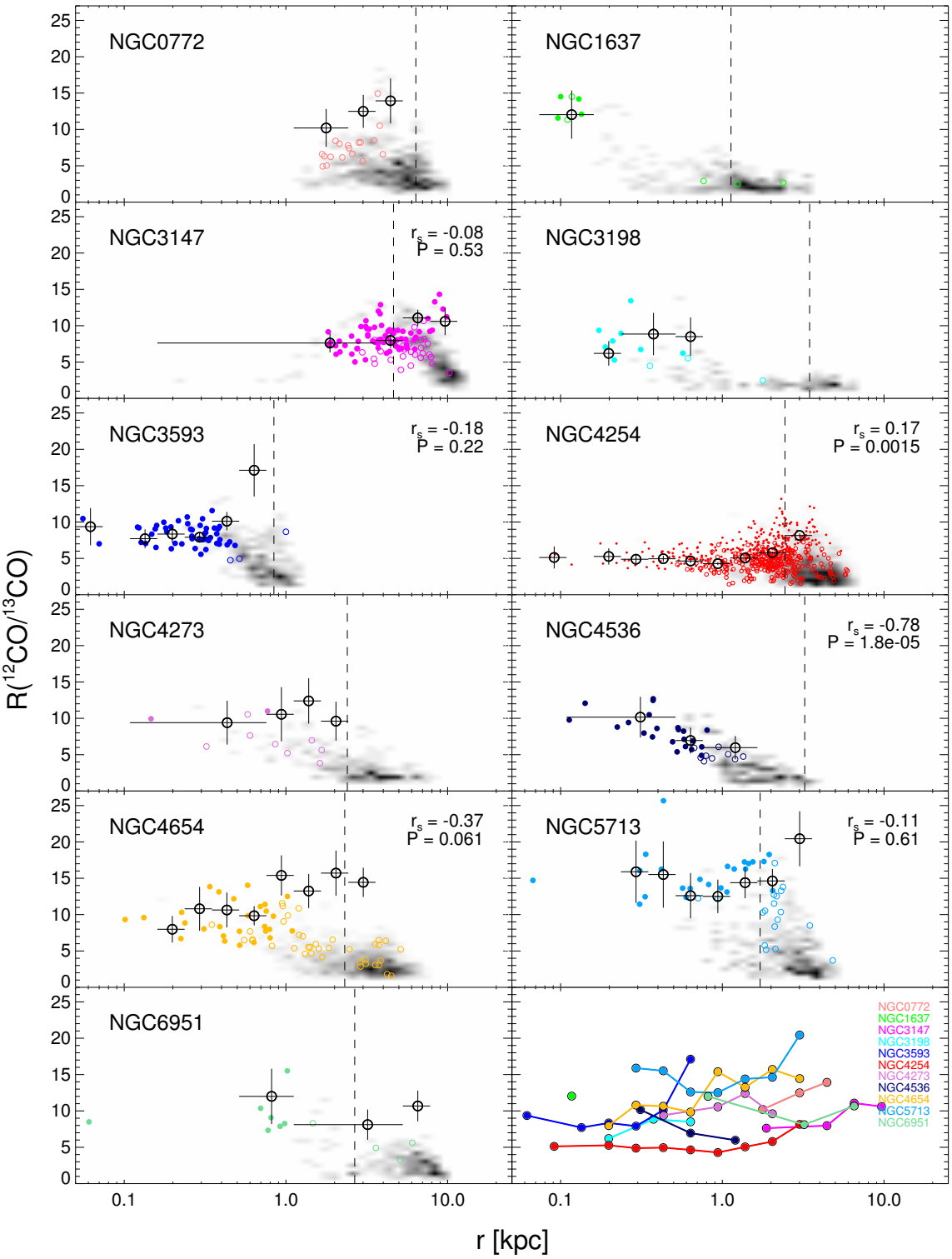

Figure 2.17. Line intensity ratio $\mathcal{R}$ as a function of radius. The first 11 panels show the results for each individual galaxy. Small colored circles show the ratios for individual half-beams with $\mathcal{R}$ detected, with the filled ones highlight those from which the correlation coefficients are derived. The gray scales show the distribution of $\mathcal{R}_{\rm min} = I_{12}/3\sigma_{13}$ for those with ^{12}CO detected but $\mathcal{R}$ not detected. The black large circles are the stacked $\mathcal{R}$ in each radius bin; the horizontal error bars reflect the bin size, and the vertical error bars show their uncertainties. The vertical dotted lines show the positions of $0.2R_{25}$. Spearman's rank correlation coefficient r_s and the significance P are shown in the top right of panels with >20 valid half-beams. The last panel is a summary plot showing stacked $\mathcal{R}$, with different colors representing different galaxies.

The stacked ratios in 5 galaxies, NGC 3593, 4254, 4273, 4654, and 5713, are larger than the weighted mean $\langle\mathcal{R}\rangle$ beyond galactocentric distance of ~ 1 kpc. The elevated $\mathcal{R}$ in the outer regions, if due to decreased CO opacity, may reflect lower density in the gas, since the expected changes in temperature and line width (decreasing away from the galaxy center) would tend to *increase* the opacity. Alternatively, a positive radial gradient of $[^{12}C/^{13}C]$ abundance could also result in higher $\mathcal{R}$ in the outer region.

2.4.2.2 Dependence on line width

Increasing the line width will tend to reduce the opacity in a single velocity channel. As long as the ^{12}CO line remains moderately optically thick, the larger velocity dispersion will elevate the ^{12}CO intensity and thus $\mathcal{R}$ if the other properties of the molecular gas do not vary significantly. We used the M12 masks described in Section 3.1 to generate maps of the ^{12}CO intensity-weighted second moment ("moment-2"). The moment-2 value for each half-beam is a measure of the width of the spectral line (~ 0.42 FWHM for a Gaussian profile). The range of the moment-2 for the samples is $\sim 5 - 100$ km s^{-1}, with the lowest line width determined by the spectral resolution of 10 km s^{-1} we used. The line width in each galaxy generally decreases at larger distance from the galaxy center, except for NGC 772 where the moment-2 peaks in one of the spiral arms.

We measured the dependence of $\mathcal{R}$ on moment-2 in a similar manner as for galactocentric radius and show the results in Figure 2.18. No strong correlations are found in any of the galaxies for the resolved $\mathcal{R}$. In some galaxies, the stacked $\mathcal{R}$ with lowest moment-2 show higher values. This trend is connected to the radial trend, with moment-2 decreasing with radius. For different galaxies, a larger moment-2 does not directly lead to a higher $\mathcal{R}$ overall. These results imply that the changes in the ^{12}CO line width in galaxies do not lead to significant variations in $\mathcal{R}$.

2.4.2.3 Effect of star formation rate

Star formation activity in galaxies depends on the molecular gas properties, and also changes the physical conditions of the surrounding environment through feedback. $\mathcal{R}$, as a possible indicator of variations in molecular gas conditions, could vary with SFR. The large turbulence combined with the higher temperature and radiation strength in starbursts could explain their elevated $\mathcal{R}$ values

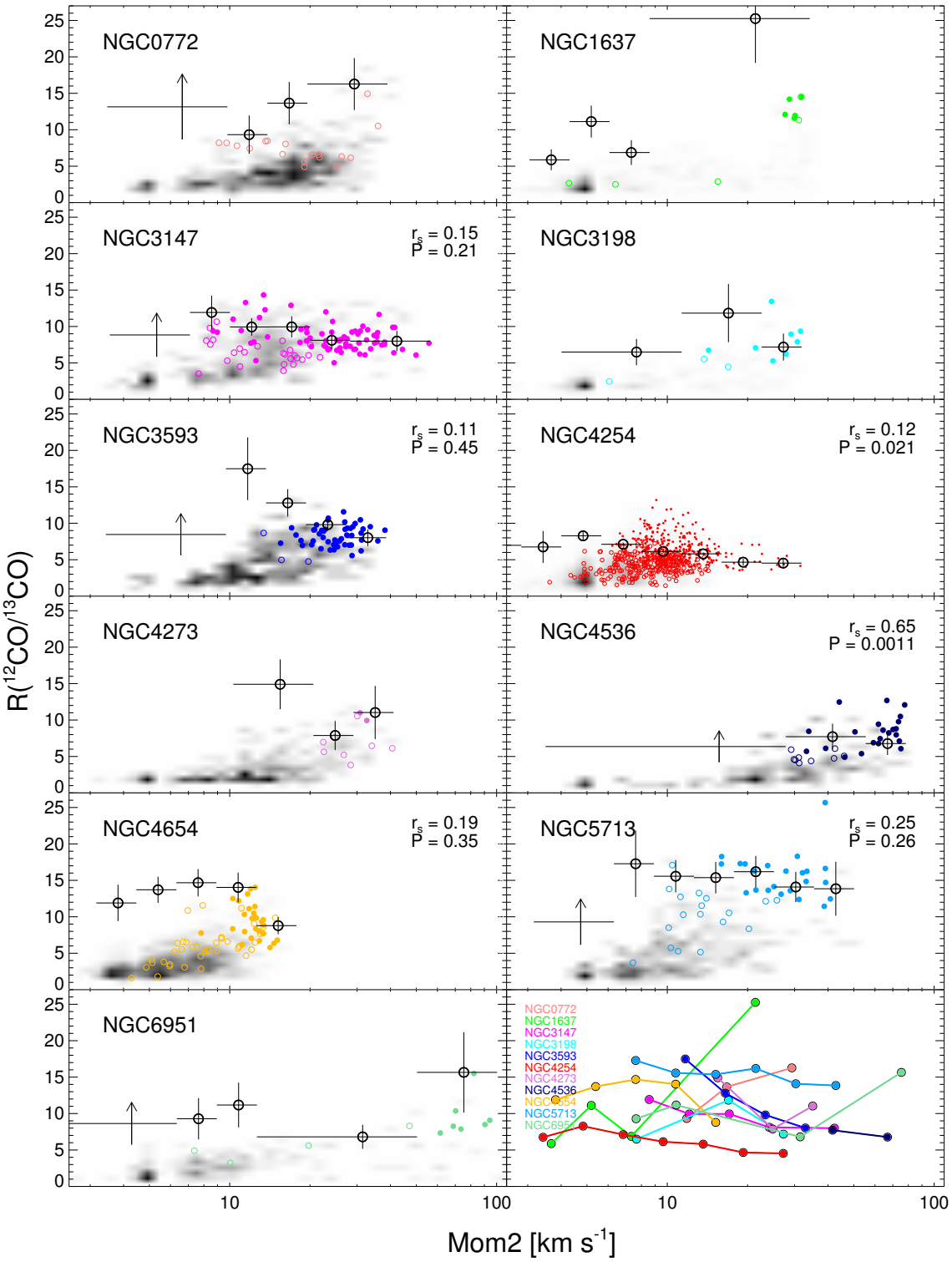

Figure 2.18. Line intensity ratio $\mathcal{R}$ as a function of moment-2. The first 11 panels show the results for each individual galaxy, excluding NGC 1569. Colored circles show the ratios for individual half-beams; the filled ones are those used for deriving Spearman's rank correlation coefficient r_s and the significance P shown in the top right of each panel. The gray scales show the distribution of $\mathcal{R}_{\rm min} = I_{12}/3\sigma_{13}$ for the ^{13}CO non-detections. The black circles and arrows are the stacked $\mathcal{R}$ and lower limits of $\mathcal{R}$ as a function of moment-2 respectively; the horizontal error bars reflect the bin size, and the vertical error bars show their uncertainties. The last panel is a summary plot showing trends of the stacked $\mathcal{R}$, with different colors representing different galaxies.

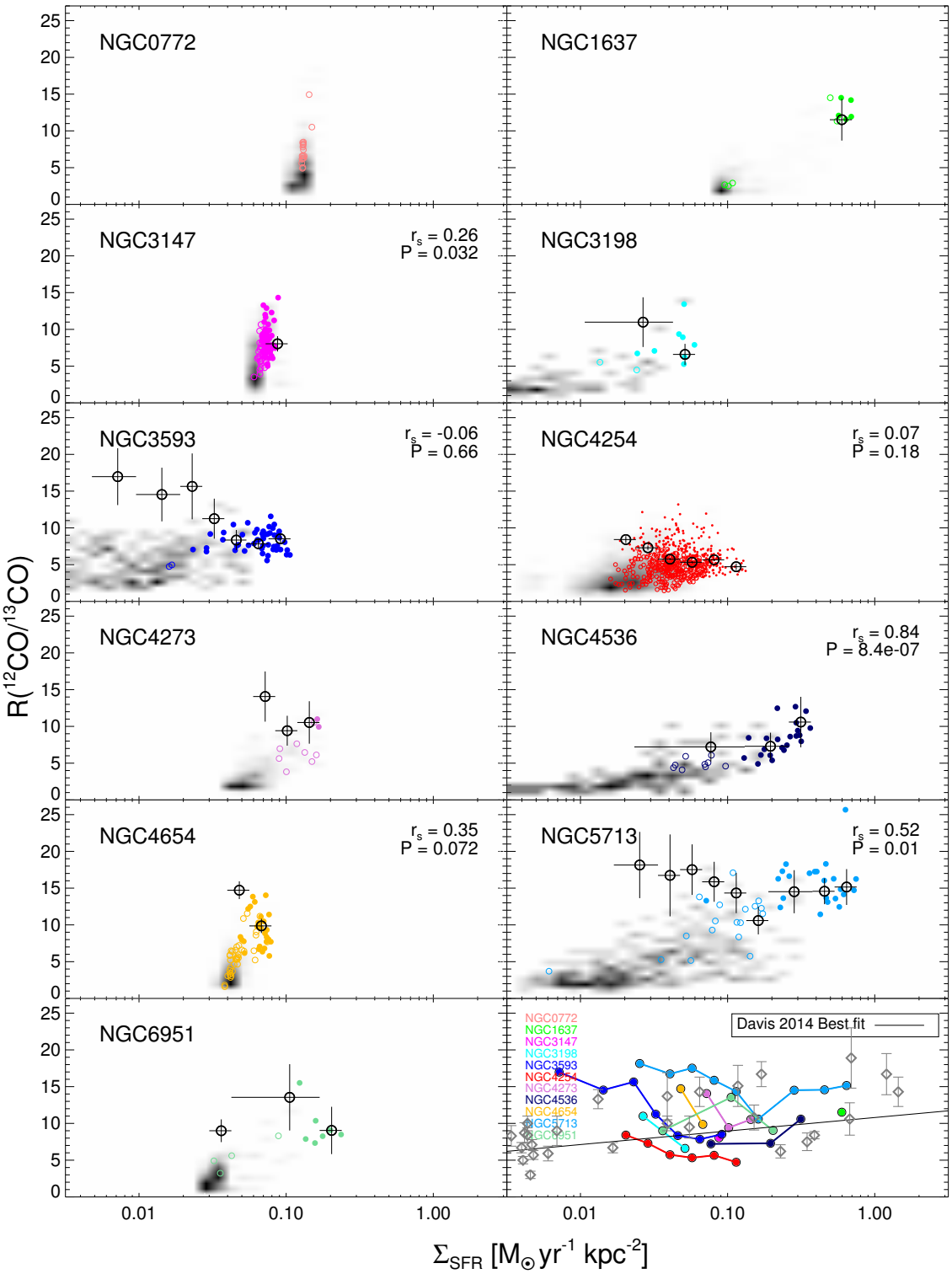

Figure 2.19. Line intensity ratio $\mathcal{R}$ distribution as a function of SFR. The first 11 panels show the results for each individual galaxy in the similar manner as Figure 2.17. In the last panel, colored circles are the trends of stacked $\mathcal{R}$; the black solid line is the linear function provided by Equation 1 of Davis (2014), which results from fitting measurements of $\mathcal{R}$ and star formation rate reported for galaxies in the literature; gray diamonds are the reported values for galaxies in Table 1 of Davis (2014).

(Aalto et al., 1995). Gradients of $\mathcal{R}$ decreasing away from local starbursting regions have also been seen in some spatially resolved studies (Aalto et al., 2010; Hirota et al., 2010; Watanabe et al., 2011).

To study the correlation between $\mathcal{R}$ and SFR density for individual half-beams, we use the 24μm intensity from Spitzer MIPS as a proxy for SFR. For the 2 galaxies with common beam size larger than the 6″ resolution of MIPS 24μm, NGC 3147 and 6951, we convolved their 24μm maps to match the common resolution of the ^{12}CO and ^{13}CO. The 24μm maps are further re-sampled onto the hexagonal grids described in Section 2.3.1. We calculate the SFR following Equation 7 in Calzetti et al. (2010) as

$$\mathrm{SFR}(M_\odot\ \mathrm{yr}^{-1}) = 2.46 \times 10^{-43} L_{24\mu\mathrm{m}}(\mathrm{ergs\ s}^{-1}). \tag{2.6}$$

The results are shown in Figure 2.19. Galaxies with large ranges of SFR density show that the stacked $\mathcal{R}$ is higher for low SFRs. For the resolved $\mathcal{R}$, only in NGC 4536 does $\mathcal{R}$ increase with SFR; in all the other galaxies, $\mathcal{R}$ does not show a strong correlation with the SFR. NGC 4536 is also the only galaxy showing a strong radial gradient of $\mathcal{R}$. Both of its correlations with SFR and radius can be explained by decreased opacity as a result of strong stellar feedback. We discuss the apparent lack of dependence of $\mathcal{R}$ on SFR for other galaxies further in Section 2.5.2.

2.5 Discussion

2.5.1 Line ratio and ISM density structure

There are both observational findings and theoretical predictions of the existence of diffuse gas only traced by ^{12}CO. In previous studies, $\mathcal{R}$ values in the diffuse ISM are generally larger than those in bound, dense clouds (GMCs) (Blitz et al., 1984; Knapp & Bowers, 1988). In the Milky Way, observations of diffuse gas find $\mathcal{R} \gtrsim 10$–15, while $\mathcal{R}$ as low as 3–4 has been reported for dark clouds (Liszt et al., 2010). In nearby galaxies, both GMCs and diffuse gas are included in the larger extragalactic beams, so $\mathcal{R}$ of the beam depends on the ISM density structure. A higher fraction of diffuse gas in the beam will lead to a higher $\mathcal{R}$ value than in the case of dense, opaque clouds (Wilson & Walker, 1994). On (sub-)kpc scales, the typical $\mathcal{R}$ found in nearby galaxies is ~ 8 in

^{13}CO surveys (e.g. Young & Sanders, 1986; Paglione et al., 2001), while $\mathcal{R} \gtrsim 20$ is often considered as an indicator of diffuse gas (e.g. Aalto et al., 2010).

In our sample, the spatially resolved $\mathcal{R}$ of each galaxy are mostly in the range of 7–9, and no extremely high $\mathcal{R}$ is found in our sample. However, our resolved $\mathcal{R}$ measurements on kpc scales have two shortcomings: lack of short-spacing on large scales and limited sensitivity on small scales. First of all, our interferometer-only data may be insensitive to a spatially extended component of diffuse gas. Examining the effect of including single-dish data, Pety et al. (2013) found diffuse molecular gas contributing 50% of the ^{12}CO emission on scales larger than 1 kpc in M51. Compared to Pety et al. (2013), the galaxies in our sample are more distant than M51, and CARMA offers shorter spacings than the IRAM interferometer used in their study. Based on the comparison of $^{12}\mathrm{CO}(J = 1 \rightarrow 0)$ and $^{12}\mathrm{CO}(J = 2 \rightarrow 1)$ flux presented in Section 3.2, we recover $50\% - 80\%$ of the flux in ^{12}CO with the interferometer data. Assuming all the missing flux is contained in diffuse gas that has intrinsically high $\mathcal{R}$ values, the flux ratios of $F(^{12}\mathrm{CO})/F(^{13}\mathrm{CO})$ could be underestimated by up to a factor of 2 in our study.

On the other hand, even when diffuse emission is not resolved out by the interferometer, it may not be detected in individual half-beams because of the limited brightness sensitivity of interferometer maps. Because the interferometer maps usually have higher noise levels, low S/N emission will not be detected in individual half-beams. This can be inferred from the comparison between the weighted mean ratio $\langle\mathcal{R}\rangle$ and the flux ratio $F(^{12}\mathrm{CO})/F(^{13}\mathrm{CO})$ in Figure 2.7: the former, resulting directly from the ^{13}CO-detections, are generally less than the flux ratios, which include the low S/N regions. The different relative ratios of $F(^{12}\mathrm{CO})/F(^{13}\mathrm{CO})$ to $\langle\mathcal{R}\rangle$ in the galaxies can be interpreted as indicating different contributions of diffuse gas to $F(^{12}\mathrm{CO})/F(^{13}\mathrm{CO})$. In NGC 772, 4273, and 4654, $F(^{12}\mathrm{CO})/F(^{13}\mathrm{CO})$ is more than 3 times larger than $\langle\mathcal{R}\rangle$, suggesting there is a significant amount of diffuse gas with higher line ratios distributed on large scales. Furthermore, the stacking analysis allows us to measure average $\mathcal{R}$ with better sensitivity and thus identify regimes in which diffuse gas may lead to higher $\mathcal{R}$. Figure 2.8 shows that some galaxies with slightly enhanced $F(^{12}\mathrm{CO})/F(^{13}\mathrm{CO})$ ratios show excess stacked $\mathcal{R}$ at low I_{12} intensity, such as in NGC 3593, 4273, and 4654. This suggests that a diffuse component becomes dominant in low brightness regions. Moreover, we found that 8 galaxies in our sample (except NGC 1637, 4536 and 6951) show stacked

$\mathcal{R}$ at their largest galactocentric distances than $\mathcal{R}$ of the innermost region we can probe. In 6 galaxies, NGC 772, 3198, 3593, 4254, 4273, 4654, and 5713, the stacked $\mathcal{R}$ beyond a distance of $\gtrsim$ 1kpc are larger than the weighted mean $\langle\mathcal{R}\rangle$. In these 6 galaxies, only NGC 772 shows stacked $\mathcal{R}$ increasing with velocity dispersion; for the other 5 galaxies, stacked $\mathcal{R}$ does not depend on line width but decreases with SFR for $\Sigma_{\rm SFR} \lesssim 0.1$ $\rm M_\odot yr^{-1}kpc^{-2}$. It is possible that these trends are due to the increased fraction of diffuse gas at larger galactic radii; this is compatible with the expectation that diffuse gas becomes more abundant when going from center to atomic-dominated regions. Alternatively, it is also possible that the radial trend is drawn from a SFR trend; for NGC 3593, 4273, and 4654, it can also be a result of $\mathcal{R}$'s dependence on I_{12}. We conclude that for normal spiral galaxies, half-beams with diffuse gas are most likely to be distributed in outer disk regions with low SFRs. However, as most of these half-beams are below our detection limit, higher sensitivity resolved ^{13}CO mapping would be needed to better identify their actual distribution and correlations with other local properties. Meanwhile, further studies incorporating single dish flux ratios are indispensable to identify extended diffuse structures.

2.5.2 Lack of correlation between resolved $\mathcal{R}$ and SFR

Using global $\mathcal{R}$ in more than 40 galaxies from literature, Davis (2014) found $\mathcal{R}$ is correlated with SFR surface density among spiral and early-type galaxies, and attributed this trend to systematically higher gas temperature and/or velocity dispersion with increasing SFR. Higher star formation could heat the gas, and a higher temperature will reduce optical depths of both ^{13}CO and ^{12}CO emission, resulting in a higher $\mathcal{R}$ (Aalto et al., 1995; Paglione et al., 2001). Furthermore, feedback turbulence from active star formation could also reduce the optical depth and elevate the line ratio (Aalto et al., 2010).

In our sample, except NGC 4536, we do not find a strong correlation between resolved $\mathcal{R}$ and star formation rate within a galaxy based on a kpc-scale analysis (Figure 2.19). One possibility is that the higher gas density associated with higher SFR surface density may offset the impact of temperature and velocity dispersion on optical depth. Taking non-LTE effects into account, other studies using LVG models show that for molecular gas with high kinetic temperatures of $\sim$ 100 K, a volume density of $n_{\rm H_2} \sim 10^4$ cm^{-3} could result in $\mathcal{R} \sim 10$, comparable to $\mathcal{R}$ values for typical

conditions in the disk (Sakamoto et al., 1997a; Meier & Turner, 2004). For dense gas, the ^{13}CO emission is enhanced compared to the lower density regions where it is subthermally excited, so $\mathcal{R}$ measured in regions dominated by warm and dense gas could be similar to that of the cold and lower density gas in typical disk conditions. The expectation of warm, dense gas in active star formation regions is also consistent with HCN observations indicating large volume densities in such regions (e.g. Gao & Solomon, 2004; Wu et al., 2005). As discussed in Section 2.5.1, stacked $\mathcal{R}$ decreases with SFRs for $\Sigma_{\rm SFR} \lesssim 0.1$ M$_\odot$yr^{-1}kpc^{-2} which might be due to the larger fraction of diffuse gas also also reflecting a density dependence for $\mathcal{R}$. It is also interesting to note that in both of the two galaxies with relatively active in star formation in our sample, NGC 4536 and 5713, $\mathcal{R}$ increases with SFR for $\Sigma_{\rm SFR} \gtrsim 0.1$ M$_\odot$yr^{-1}kpc^{-2}. The offset of $\mathcal{R}$ by density might be less for higher SFRs. However, more resolved observations are needed to confirm the trend. On the other hand, if high temperature is not accompanied by higher gas density, as would be the case for diffuse gas adjacent to star forming regions, then higher $\mathcal{R}$ would be expected; it is possible that such a trend may be missed by our interferometer data which are less sensitive to this diffuse gas.

Aside from modifying the optical depth, star formation activity can also affect $\mathcal{R}$ by changing the abundance of ^{13}CO relative to ^{12}CO. UV radiation from star formation sites can reduce the ^{13}CO abundance by isotope-selective photodissociation, leading to higher $\mathcal{R}$ in star forming regions. However, this photodissociation effect is generally disfavored by the lack of an observed correlation between $\mathcal{R}$ and ^{13}CO/C^{18}O, given that C^{18}O should be more affected by isotope-selective photodissociation (Paglione et al., 2001; Tan et al., 2011; Danielson et al., 2013). Higher $\mathcal{R}$ could also be due to an enhanced ^{12}C abundance resulting from recent massive star formation in star forming regions (Casoli et al., 1991; Taniguchi & Ohyama, 1998). We also did not find resolved $\mathcal{R}$ increases with SFRs in each galaxy as expected if ^{12}CO abundance is enhanced by isotope-selective photodissociation or massive star formation. In contrast, chemical fractionation towards ^{13}CO at temperatures less than 35 K would decrease the relative abundance of ^{12}CO to ^{13}CO, decreasing $\mathcal{R}$ if the clouds remain cold (Chu & Watson, 1983; Milam et al., 2005). This effect could also compensate the changes of opacity on $\mathcal{R}$. Given these competing effects of abundance and opacity, it is clear that more direct measurements of isotopic abundances as a function of star formation activity are needed in addition to the line ratios $\mathcal{R}$.

2.5.3 Implications for $X_{\rm CO}$

Since ^{12}CO is a widely used tracer for molecular mass, understanding how the CO-to-H_2 conversion factor $X_{\rm CO}$ varies in different environments is crucial for extragalactic studies. With less optical depth than ^{12}CO, ^{13}CO would appear to be a better tracer of column density. In Milky Way studies, ^{13}CO has been used as an independent measurement of molecular gas column density to calculate $X_{\rm CO}$ (e.g. Pineda et al., 2008; Roman-Duval et al., 2010). However, these calculations are based on a series of assumptions that cannot easily be generalized to extragalactic environments: ^{13}CO emission traces the same density structure as ^{12}CO, the abundance of ^{13}CO is constant, and most importantly, the gas is under LTE. When observed on large scales in external galaxies, ^{12}CO emission can also arise from the intra-cloud gas in addition to the dense clouds which account for most of the ^{13}CO emission. A fixed abundance of ^{13}CO is unlikely to be appropriate for galaxies that span a large range in properties such as metallicity and star formation rate. Similarly, the simplified assumption of LTE is also questionable when a wide range of local conditions occur within the telescope beam. And even where LTE does approximately hold, an estimate of the kinetic temperature is needed to constrain the excitation analysis.

Despite these difficulties inferring the $X_{\rm CO}$ factor from ^{13}CO observations following LTE assumptions, the $X_{\rm CO}$ and $\mathcal{R}$ are expected to be anti-correlated provided the relative [^{12}CO/^{13}CO] abundance does not change dramatically. Both $X_{\rm CO}$ and $\mathcal{R}$ depend on the bulk properties of molecular clouds; variations in physical conditions that affect one of them will also likely affect the other. For example, if an unusually high $\mathcal{R}$ (> 20) is identified such as in the case of a starbursting galaxy, there are good reasons to doubt if a standard $X_{\rm CO}$ should be applied. The $X_{\rm CO}$ values measured in starbursting galaxies are indeed ~ 5 times lower than the standard value (Bryant & Scoville, 1999; Papadopoulos et al., 2012). A larger velocity dispersion and higher temperature can explain the higher $\mathcal{R}$ and lower $X_{\rm CO}$ at the same time. However, it is still difficult to observe a clear (anti-)correlation between $\mathcal{R}$ and $X_{\rm CO}$ for normal galaxies. Among different galaxies, none of the properties we have examined (metallicity, inclination, line width and star formation activity) seem to play an important role in determining the global $\mathcal{R}$. This is consistent with the nearly constant $X_{\rm CO}$ observed over a similar metallicity range in other studies. By inferring the H_2 mass from the difference of dust-derived gas mass and HI observations, Sandstrom et al. (2013) reported

a generally flat radial distribution for $X_{\rm CO}$ in nearby galaxies. We also find $\mathcal{R}$ to be rather constant within a galaxy, which seems to be consistent with their results. While Sanders et al. (2003) found a lower $X_{\rm CO}$ in the central kpc in their sample galaxies on average, the lack of $\mathcal{R}$ measurements outside ~ 2 kpc for most of our galaxies (due to sensitivity limitations) prevents us from comparing the outer region with the central kpc of our sample. In the future, use of additional diagnostics of the physical conditions in the molecular gas (for example, high critical density lines or higher excitation transitions) should permit a more detailed description of variations in $X_{\rm CO}$.

2.6 Conclusions

We have measured ^{13}CO fluxes for 12 galaxies in the CARMA STING sample and obtained ^{13}CO maps for 11 of these on scales of a few hundred pc to a few kpc. We compare these maps with ^{12}CO observations, and investigate the resulting ^{12}CO to ^{13}CO line intensity ratio ($\mathcal{R}$) maps to study their dependence on line width, galactocentric distance and star formation activity. We also study the relation between galaxy properties and line ratios for galaxies in the sample. Our main conclusions are:

1. For the regions where both ^{12}CO and ^{13}CO are detected, the resolved $\mathcal{R}$ values range from 5.9 to 14.9, with most values between 7 and 9, which are quite similar to $\mathcal{R}$ of GMCs in nearby galaxies. We do not find any half-beams with very high $\mathcal{R}$ (> 20) which are usually associated with presence of diffuse gas, implying that the majority of regions sampled in our data are likely to be dense gas structures. We note that detection of very high resolved $\mathcal{R}$ may require more sensitive observations.

2. For regions with high S/N of ^{13}CO, the resolved $\mathcal{R}$ in a galaxy increases with I_{12}. However, stacking all the beams with ^{12}CO detection regardless of ^{13}CO S/N, we found that the average $\mathcal{R}$ does not depend on I_{12}, or show a decreasing trend. The discrepancy between the resolved $\mathcal{R}$ and stacked $\mathcal{R}$ can be explained as a bias induced by the limited sensitivity in the resolved $\mathcal{R}$ measurements.

3. Integrating ^{13}CO over the entire galaxy, we obtain the flux ratios of ^{12}CO to ^{13}CO emission- for the 12 galaxies in our sample, with a typical value around 10. By including half-beams

under the ^{13}CO detection threshold, the $F(^{12}\mathrm{CO})/F(^{13}\mathrm{CO})$ is generally larger than the ^{13}CO intensity weighted mean of the resolved line ratio $\langle\mathcal{R}\rangle$ in a galaxy. Although there are significant galaxy-to-galaxy variations in both $F(^{12}\mathrm{CO})/F(^{13}\mathrm{CO})$ and $\langle\mathcal{R}\rangle$, we do not find clear dependences of the line ratios on galaxy properties.

4. Contrary to expectations from previous findings from single dish observations on galaxy scales, we find no clear evidence that resolved $\mathcal{R}$ on (sub)kpc scales depends on the local properties of galactocentric radius, line width, or star formation activity. However, our resolved $\mathcal{R}$ values are confined to regions with bright ^{13}CO and hence span a small dynamic range in each of the properties. Nevertheless, our findings suggest that the effect of SF feedback on resolved $\mathcal{R}$ on (sub)kpc scales may be compensated by the underlying density and/or an isotopic abundance gradient.

5. By stacking spectra for regions with low S/N of ^{13}CO, we obtained the average $\mathcal{R}$ as functions of galactocentric radius, line width, and SFR. NGC 3593, 4254, 4273, 4654 and 5713 show stacked $\mathcal{R}$ that are elevated beyond galactocentric distance of $\sim$ 1 kpc as well as higher stacked $\mathcal{R}$ with lower SFRs. We suggest that the increased $\mathcal{R}$ are due to larger fractions of diffuse gas beyond galactocentric distance of $\sim$ 1 kpc. Alternatively, stacked $\mathcal{R}$ can also be increased in outer regions if the ^{13}CO abundance decreases away from the center.

6. While resolved $\mathcal{R}$ on (sub-)kpc scales show limited variations within a galaxy, indications of systematic differences of $\mathcal{R}$ between galaxies are seen in our sample, implying that resolved $\mathcal{R}$ might be sensitive to environmental properties, on local or global scales, that are not captured by our current analysis. Inclusion of additional data, such as stellar mass, star formation and gas accretion history, or abundances of secondary elements, may be needed to better understand these variations.

Chapter 3

^{13}CO Observations in the CARMA Extragalactic Database for Galaxy Evolution (EDGE) Survey

We present ^{13}CO observations for the EDGE-CALIFA survey, which is a mapping survey of 126 nearby galaxies at a typical spatial resolution of 1.5 kpc. Combining our CO observations with optical spectroscopy data, we perform a systematic study of spatially resolved ^{13}CO and $\mathcal{R}$ on kpc scales in relation to the properties of stellar and ionized gas for a wide variety of galaxies. We find that the $\mathcal{R}$ values are higher in the interacting galaxies than in the isolated galaxies, but they are insensitive to other global properties such as morphology, total stellar mass, or galaxy size. Interpretation of correlations between $\mathcal{R}$ and the resolved properties is challenging, especially as the low signal-to-noise of ^{13}CO imposes selection biases on the investigation. We carefully study possible effects of sensitivity bias on $\mathcal{R}$ and the resolved correlations through Monte Carlo simulations. We also present annulus-averaged $\mathcal{R}$ profiles for our sample up to a galactocentric radius of $\sim$5 kpc, taking into account the ^{13}CO non-detections by spectra stacking. We find that roughly half of the galaxies show increased $\mathcal{R}$ beyond $0.25R_{25}$, suggesting more optically thin gas in the disks relative to the centers generally.

3.1 Introduction

The molecular ISM plays a critical role in galaxy evolution, serving as the fuel for star formation in galaxies. Large scale processes accumulate the gas and regulate the structure of molecular clouds. In turn, the gas properties on local cloud scales control the star formation process which drives the evolution of the entire galaxy. Studies of the molecular ISM properties on local scales and their relations to both local and global scale properties from nearby galaxy surveys are therefore important to the understanding of galaxy evolution.

In nearby galaxies, ^{12}CO($J = 1 \rightarrow 0$) is the most commonly used tracer of molecular gas.

However, its high opacity hampers the estimation of properties of molecular gas. The less abundant isotopologue ^{13}CO has lower optical depth and is essential for determination of physical conditions in molecular gas using CO lines. The line intensity ratio $^{12}\mathrm{CO}(J = 1 \rightarrow 0)/\ ^{13}\mathrm{CO}(J = 1 \rightarrow 0)$ (hereafter $\mathcal{R}$) can be used to trace variations in optical depths of molecular gas, with the caveat that it can also be influenced by chemical processes.

Because the emission of ^{13}CO is weaker and more difficult to observe, there are only a small number of galaxies studied with high resolution interferometric mapping (e.g. Meier & Turner, 2004; Pety et al., 2013; Aalto et al., 2010; Sliwa et al., 2017). Variations of resolved $\mathcal{R}$ within a galaxy are found in these studies. However, these studies did not provide quantitative investigation of relations between $\mathcal{R}$ and other local physical properties. Previous single dish studies found that the unresolved $\mathcal{R}$ of a galaxy increases with the *IRAS* IR color and the average SFR surface density, suggesting that the global $\mathcal{R}$ values are sensitive to the temperature and/or the line width through opacity (Young & Sanders, 1986; Aalto et al., 1991; Davis, 2014). In contrast to these single dish extragalactic ^{13}CO surveys, no strong correlation between $\mathcal{R}$ and SFR surface density has been found on scales under several kpc (Cao et al., 2017; Cormier et al., 2018). Alternatively, high $\mathcal{R}$ in a galaxy can also imply more diffuse molecular gas in the region than low $\mathcal{R}$ regions (e.g. Roman-Duval et al., 2016; Goldsmith et al., 2008; Rickard & Blitz, 1985; Pety et al., 2013). Changes in $\mathcal{R}$ therefore may reflect variations in the density of molecular gas in different regions within a galaxy.

Resolved $\mathcal{R}$ values ranging from 4 to 25 have been reported in nearby galaxies. In recent systematic studies of resolved $\mathcal{R}$ on (sub)kpc scales, besides variations of $\mathcal{R}$ within a galaxy, Cao et al. (2017) and Cormier et al. (2018) found significant galaxy-to-galaxy differences in $\mathcal{R}$. Without considering chemical effects, the variations of resolved $\mathcal{R}$ observed among different galaxies may also reflect the different molecular properties and structures regulated by galaxy properties on large scales. However, no strong correlations between resolved $\mathcal{R}$ and global galaxy properties are found in these studies with the rather small numbers of galaxy sample. Observations of ^{13}CO for a large sample of galaxies spanning a significant range of global galaxy properties are needed to study how $\mathcal{R}$ varies among galaxies, and whether large scale properties have a direct impact on the molecular gas opacity and density structure.

On the other hand, the difference in $\mathcal{R}$ could reflect variations in ^{13}CO abundance related to

nucleosynthesis. While ^{12}C is produced by all stars through various mass loss mechanism, ^{13}C is ejected into the ISM in the AGB phase of low mass stars mainly via CNO processing of ^{12}C . The isotope fractional abundance [^{12}C/^{13}C] is therefore an important tracer of the chemical evolution of galaxies. Due to the opacity effect, $\mathcal{R}$ can be used as a lower limit of [^{12}C/^{13}C] (Henkel & Mauersberger, 1993). Abnormally high $\mathcal{R}$ values are found in (U)LIRGs and high redshift galaxies and are suggested to relate to the recent star formation in these galaxies (Sliwa et al., 2017; Danielson et al., 2013). Meanwhile, a study using chemical evolution modeling suggests $\mathcal{R}$ could be used to constrain the low mass end of initial mass function (Romano et al., 2017). However, the overall picture of how the $\mathcal{R}$ relates to the chemical evolution of galaxies remains unclear. Since the chemical composition of stellar populations and ionized gas also offer useful information about the chemical evolution, studying their relations to $\mathcal{R}$ will shed light on the impact of nucleosynthesis on molecular gas.

In this study, we present the mapping of ^{13}CO($J = 1 \rightarrow 0$) and the line ratio $\mathcal{R}$ on kiloparsec scales for a wide variety of galaxies from the the EDGE survey (Bolatto et al., 2017). Combining our ^{13}CO observations with optical spectroscopic data, we investigate how molecular gas properties could be affected by global galaxy properties, and how molecular gas relates to the underlying stellar population and ionized gas on kpc scales. We describe the ^{13}CO observations and the ancillary data from the CALIFA IFU survey in Section 3.2. In Section 3.3, we present the results of $\mathcal{R}$ and their relations to global and resolved properties. We discuss the implication of $\mathcal{R}$ variations and the caveats of this study in Section 3.4.

3.2 Observations and Data Description

3.2.1 EDGE ^{13}CO observation

The ^{13}CO observations of EDGE were carried out from late 2014 to mid 2015 in the CARMA D and E arrays. Full details of the survey, observations, and data reduction for the EDGE sample are described in Bolatto et al. (2017). The sample galaxies were observed in CARMA's "snapshot" mode, which automatically chooses high priority targets that need integration time and are over the elevation limit. The targets are assigned to three groups according to their optical redshift, and

each group uses the same tuning and correlation setup. ^{13}CO is obtained simultaneously with ^{12}CO with the correlator at 110.201 GHz in the lower sideband. The ^{12}CO bandwidth is 250 MHz and 5 bands are used to cover the velocity range of 3000 km/s with 3.4 km/s resolution, while ^{13}CO uses 3 bands with bandwidth of 500 MHz, corresponding to a 3800 km/s range with a lower spectral resolution of 14.3 km/s. A 7-point hexagonal mosaic with centers separated by the primary beam size of $27''$ was used, to cover the field-of-view (FoV) with radius $\sim 50''$. The integration time of each galaxy is about 40 minutes in E-array, and ~ 3.5 hours in D-array.

The visibility data calibration was done by the automatic pipeline developed for STING using MIRIAD (Rahman et al., 2011, 2012; Wong et al., 2013). Uranus is the primary flux calibrator used; when it is not available, Mars, Neptune, or MWC349 are used. Phase calibrators are automatically selected from the snapshot database, within 25° from the source. The uncertainty from the calibration is $\sim 10\%$. The calibrated data are deconvolved and imaged using the MIRIAD tasks MOSSDI2 and INVERT with Briggs's weighting robustness parameter of 0.5. The resulting typical beam size for ^{13}CO is $\sim 5''$. The pixel size of the data cubes is $1''$, and the velocity range is 860 km s^{-1} (1600 km s^{-1} for ARP 220) with a channel spacing of 20 km s^{-1}. We aligned the ^{13}CO cube to ^{12}CO cube's spatial cell for each galaxy. We choose a common resolution of $7''$ and smooth all the ^{12}CO and ^{13}CO cubes to a beam size of $7''$ for further analysis.

3.2.2 The CALIFA IFU Survey

The galaxies in the EDGE sample are selected from the CALIFA survey, an optical IFU survey consisting of ~ 600 nearby galaxies observed by the 3.5 m telescope at the Calar Alto Observatory (Sánchez et al., 2012, 2016a). The sample galaxies in CALIFA are selected from SDSS DR7 with diameter in the range of $45'' - 79.2''$ to achieve sufficient spatial coverage of the galaxy within the IFU's FoV of $74 \times 64''$. The sample has a mass range of $9.7 < \log M_*(\mathrm{M}_\odot) < 11.4$ at $0.005 < z < 0.03$, showing similar statistical properties to massive main sequence galaxies in the SDSS sample (Walcher et al., 2014). The spatial resolution of the CALIFA is typically $2.5''$, corresponding to a scale of ~ 700 pc at a distance of 70 Mpc. With the (sub)-kiloparsec resolution, the CALIFA IFU survey enables investigation of spatially resolved properties of stellar and ionized gas contents for a large sample of galaxies in the local universe. The spectra are observed in two

setting, with a low resolution of 6 Å across the full spectral range and a medium resolution of 2.3 Å (Sánchez et al., 2016a) covering shorter wavelengths. We use the low spectral resolution data in this study because the low resolution spectra have wider spectral coverage.

The spatially resolved properties of the stellar populations and ionized gas are derived from the CALIFA observations by Pipe3D (Sánchez et al., 2016b), a pipeline developed for IFU data reduction by Sánchez et al. (2016a). Pipe3D uses a Monte-Carlo approach to model the continuum emission from the stars and the line emission from the ionized gas. The stellar emission is modeled by a linear combination of synthetic stellar populations (SSP), taking into account non-linear effects of stellar kinematics and dust attenuation on the spectra. The underlying population resulting from the model is used to derive average quantities such as the age and metallicity for each pixel. Meanwhile, the emission lines are modeled with single Gaussian functions to obtain fluxes, velocities, and line widths. For each spectrum, after the emission lines were subtracted, a set of stellar indices (Hδ, Hβ, Mgb, Fe5270, Fe5335, and D4000) are derived. All of these spatially resolved properties produced by Pipe3D are stored as maps with a pixel size of $1''$ for each galaxy.

3.2.3 Data alignment and extraction

We align and convolve the CALIFA Pipe3D maps to match the EDGE CO maps and build a database that combines all the resolved properties of stars, ionized gas, and molecular gas. The Pipe3D maps are first regridded to EDGE CO cubes using the IDL routine *hastrom* so that all the images of each galaxy are in the same frame. Subsequently, we convolve the recellded Pipe3D maps to $7''$ with a Gaussian kernel to match the typical resolution of the EDGE CO observations, assuming a Gaussian PSF of $2.5''$ of CALIFA cubes (although it is actually a Moffat PSF). We note this convolution is not correct for properties other than integrated flux; therefore we only use the smoothed maps of fluxes in the analysis to derive resolved properties in Section 3.2.4.

After the CALIFA and EDGE images are aligned and smoothed, we extract the values from both the regridded and smoothed images based on hexagonal cells to reduce the data redundancy for the analysis. We generate the hexagonal cells on the images with spacings of $3.5''$, that is, half of the FWHM beam size of the convolved images. We select the values of the $1'' \times 1''$ pixel nearest to each hexagonal cell's center to represent the properties for the entire cell, and extract them from

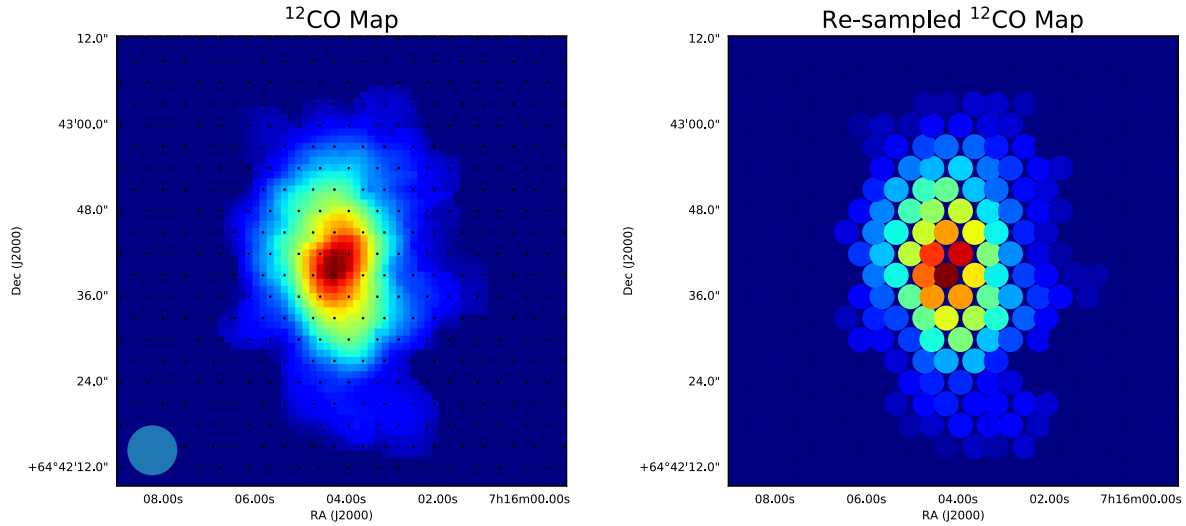

Figure 3.1. ^{12}CO integrated intensity maps of NGC 2347. *Left panel*: the ^{12}CO map from the aligned, smoothed ^{12}CO cube overlaid with the centers of half-beam spaced re-sampling hexagonal cell shown as black dots; the common beam size of 7″ used in this paper is shown in the left bottom. *Right panel*: the ^{12}CO map reconstructed from the data points, with a filled circle representing each re-sample cell approximately.

the images for further analysis of resolved properties in this study. By using these extracted values based on the hexagonal cells instead of each pixel from the images, we reduce the total number of data points by a factor of 10.

An example of the map of ^{12}CO integrated intensity and the map reconstructed from the re-sample data points is shown in Figure 3.1. The re-sample map gives a better sense of the beam resolution and reduces the redundant data points for further analysis. At the same time, the reconstructed map shows similar characteristics as the original map, confirming that the re-sample data points are able to maintain morphological features of morphology in the original map. We use the re-sample values on the hexagonal cell as our data points for analysis that involves resolved properties in this study. In the following, we use the term "cell" to refer to the hexagonal cells to distinguish them from the original pixels of the maps.

3.2.4 Derived properties

We calculate the star formation rate (SFR) from the extinction corrected Hα flux of each cell. The attenuation of Hα is calculated from the flux ratio of Hα/Hβ using Eq. (1) from Catalán-Torrecilla et al. (2015):

$$A(\mathrm{H}_\alpha) = \frac{K_{\mathrm{H}\alpha}}{-0.4 \times (K_{\mathrm{H}\alpha} - K_{\mathrm{H}\beta})} \times \log \frac{\mathrm{H}\alpha/\mathrm{H}\beta}{2.86}. \tag{3.1}$$

$K_{\mathrm{H}\alpha} = 2.53, K_\beta = 3.6$ are the extinction coefficients defined in Cardelli et al. (1989) for the Galactic extinction curve, and the constant 2.86 is the intrinsic Balmer ratio for case B recombination. After the extinction correction, Hα flux is converted to SFR following Eq.(2) from Rosa-González et al. (2002) assuming a Salpeter IMF:

$$SFR(\mathrm{M}_\odot\ \mathrm{yr}^{-1}) = 7.9 \times 10^{-42}\ \mathrm{L}_{\mathrm{H}\alpha}(\mathrm{erg\ s}^{-1}). \tag{3.2}$$

Both of these equations used for the SFR calculations are applicable to star forming regions only. We therefore identify the star formation regions applying the criterion suggested by Sánchez-Menguiano et al. (2016): we use the (Kewley et al., 2001) demarcation line to exclude AGN-like regions, and limit the equivalent width of Hα to $EW(\mathrm{H}\alpha) > 6$ Å to exclude weak AGNs and regions ionized by low-mass evolved stars (Cid Fernandes et al., 2011). Only for the cells classified as star forming regions is the star formation rate calculated using Equations 3.1 and 3.2. The surface densities are deprojected for disk inclination i using a correction factor of $\cos i$.

We also calculate the oxygen abundance $12 + \log(\mathrm{O/H})$ for each star forming cell from the O3N2 index, $\mathrm{O3N2} = \log([\mathrm{OIII}]\lambda5007/\mathrm{H}\beta) - \log([\mathrm{OIII}]\lambda6583/\mathrm{H}\alpha)$. We use the empirical relation calibrated from T_e-based abundance measurements by Marino et al. (2013):

$$12 + \log(\mathrm{O/H}) = 8.53 - 0.21 \times \mathrm{O3N2}. \tag{3.3}$$

3.3 Results

3.3.1 ^{13}CO integrated intensity maps

We apply the EDGE ^{12}CO dilated-mask described in Bolatto et al. (2017) to the ^{13}CO data cubes in order to generate the ^{13}CO integrated intensity maps. The mask was generated by searching pixels with ^{12}CO emission above 3.5σ in two adjacent channels of the cube, and expanding to contiguous regions with ^{12}CO above 2σ. The ^{12}CO moment maps (moment 0 for integrated intensity, moment 1 for line-of-sight velocity, and moment 2 for velocity dispersion) used in this study are also generated from these ^{12}CO dilated-masks. We define a sample of 42 galaxies as the EDGE ^{13}CO sample; in each of the sample galaxies, there are more than 55 pixels (corresponding to the size of a Gaussian

Table 3.1. ^{13}CO observation and galaxy properties in the EDGE ^{13}CO sample

No.	Galaxy	F_{13}	F_{12}/F_{13}	$\langle\mathcal{R}\rangle$	$\langle\sigma(I_{13})\rangle$ [a]	$\mathcal{N}(I_{13})$ [b]	$\mathcal{N}(I_{13})$ [c]	F_{60}/F_{100} [d]	Inter [e]
	Name	(Jy km/s)					($I_{12} > I_{\rm comp}$)		
1	ARP220	28.80 ± 3.83	29.05 ± 3.87	23.39 ± 7.31	0.63	13	11	0.90 ± 0.00	1
2	IC0480	9.14 ± 2.62	16.12 ± 4.65	8.01 ± 1.32	0.45	8	5	0.43 ± 0.04	0
3	IC0944	17.30 ± 3.77	9.85 ± 2.18	6.39 ± 2.55	0.46	8	3	0.23 ± 0.03	0
4	IC1683	13.55 ± 2.71	12.49 ± 2.52	10.69 ± 2.56	0.55	6	5	0.50 ± 0.05	0
5	IC2247	8.57 ± 2.30	15.33 ± 4.14	8.46 ± 1.96	0.29	11	0	0.38 ± 0.04	0
6	NGC0523	9.92 ± 3.55	19.08 ± 6.85	7.42 ± 2.01	0.39	6	1	0.44 ± 0.05	1
7	NGC2253	22.08 ± 4.02	13.98 ± 2.57	8.49 ± 3.80	0.35	10	3	0.40 ± 0.03	0
8	NGC2347	20.46 ± 2.79	7.65 ± 1.07	6.11 ± 0.82	0.34	14	0	0.36 ± 0.03	0
9	NGC2410	15.68 ± 3.34	10.25 ± 2.22	5.54 ± 1.21	0.41	12	0	0.41 ± 0.03	0
10	NGC2623	11.58 ± 2.13	19.68 ± 3.63	15.98 ± 1.57	0.45	8	8	0.92 ± 0.00	1
11	NGC2639	21.14 ± 3.69	8.77 ± 1.57	4.89 ± 1.45	0.37	18	0	0.28 ± 0.02	0
12	NGC2906	19.78 ± 3.40	8.69 ± 1.54	4.51 ± 1.36	0.34	9	0	0.34 ± 0.03	0
13	NGC3811	14.14 ± 3.51	12.18 ± 3.05	6.14 ± 3.50	0.35	15	4	0.44 ± 0.44	0
14	NGC3994	16.05 ± 3.12	9.17 ± 1.81	5.89 ± 1.14	0.49	9	3	0.48 ± 0.07	1
15	NGC4047	34.67 ± 4.20	10.60 ± 1.30	7.09 ± 1.37	0.44	34	16	0.36 ± 0.18	0
16	NGC4149	12.81 ± 2.62	11.50 ± 2.38	8.58 ± 1.27	0.47	11	6	0.38 ± 0.03	0
17	NGC4676A	13.76 ± 2.91	10.52 ± 2.25	8.83 ± 1.29	0.68	7	6	0.52 ± 0.04	1
18	NGC5218	39.48 ± 4.35	19.74 ± 2.18	14.21 ± 2.06	0.50	19	15	0.52 ± 0.00	1
19	NGC5394	16.40 ± 2.54	19.23 ± 2.99	18.43 ± 2.83	0.48	12	12	0.54 ± 0.21	1
20	NGC5406	5.97 ± 4.37	19.64 ± 14.42	1.44 ± 0.00	0.30	1	0	0.31 ± 0.04	0
21	NGC5480	27.22 ± 3.73	9.39 ± 1.32	7.05 ± 1.68	0.33	12	1	0.34 ± 0.02	0
22	NGC5520	13.55 ± 2.58	9.07 ± 1.77	7.20 ± 1.39	0.36	7	0	0.40 ± 0.03	0
23	NGC5614	25.19 ± 4.69	16.92 ± 3.17	12.75 ± 4.00	0.56	7	6	0.25 ± 0.02	1
24	NGC5633	23.70 ± 3.34	10.59 ± 1.52	7.19 ± 1.78	0.34	24	0	0.35 ± 0.01	0
25	NGC5908	85.94 ± 4.98	8.54 ± 0.50	7.62 ± 1.26	0.44	65	53	0.25 ± 0.25	0
26	NGC5930	16.09 ± 2.64	15.85 ± 2.62	12.21 ± 1.05	0.56	11	11	0.68 ± 0.01	1
27	NGC5934	17.47 ± 3.20	9.71 ± 1.80	8.86 ± 1.38	0.64	11	10	0.34 ± 0.02	1
28	NGC5953	50.29 ± 3.83	13.31 ± 1.03	11.43 ± 2.13	0.37	41	33	0.59 ± 0.01	1
29	NGC5980	28.08 ± 3.12	9.17 ± 1.04	6.83 ± 1.13	0.35	33	4	0.41 ± 0.03	0
30	NGC6060	19.78 ± 4.28	12.54 ± 2.74	4.62 ± 1.88	0.34	5	0	0.31 ± 0.04	0
31	NGC6155	12.40 ± 3.01	12.22 ± 3.01	4.12 ± 0.73	0.27	6	0	0.35 ± 0.02	0
32	NGC6186	30.09 ± 3.85	10.21 ± 1.33	10.70 ± 1.59	0.51	16	13	0.43 ± 0.03	0
33	NGC6361	64.84 ± 4.16	10.87 ± 0.71	9.01 ± 2.73	0.40	54	41	0.31 ± 0.01	0
34	NGC6478	28.19 ± 3.67	9.56 ± 1.26	6.61 ± 1.35	0.44	21	3	0.28 ± 0.02	0
35	NGC7738	13.35 ± 2.15	13.86 ± 2.25	11.29 ± 1.22	0.43	11	11	0.58 ± 0.07	0
36	NGC7819	9.16 ± 2.11	6.55 ± 1.55	6.45 ± 1.24	0.44	6	0	0.43 ± 0.05	0
37	UGC04029	9.37 ± 2.42	11.29 ± 2.95	6.82 ± 0.81	0.40	4	2	0.43 ± 0.04	0
38	UGC04132	26.14 ± 4.33	13.08 ± 2.18	7.68 ± 1.87	0.55	19	12	0.38 ± 0.04	0
39	UGC05111	16.73 ± 2.95	10.14 ± 1.81	7.09 ± 1.41	0.38	8	0	0.28 ± 0.08	0
40	UGC10043	17.32 ± 2.79	7.12 ± 1.19	5.19 ± 1.75	0.45	15	0	0.34 ± 0.03	0
41	UGC10123	18.22 ± 3.20	9.99 ± 1.78	6.88 ± 2.13	0.45	15	2	0.32 ± 0.02	0
42	UGC10384	13.86 ± 2.42	9.32 ± 1.65	7.73 ± 0.79	0.42	9	4	0.41 ± 0.04	0

[a] Mean 1σ noise of I_{13} using dilated ^{12}CO masks of the galaxy.

[b] Number of cells detected in ^{13}CO with S/N$>$ 3.

[c] Number of cells detected in ^{13}CO with S/N$>$ 3 and having bright ^{12}CO ($I_{12} > I_{\rm comp}$).

[d] IRAS IR color from NED.

[e] The assignment of interacting galaxies (1) or isolated galaxies (0). The interacting galaxies are those labeled as "multiple" in the HyperLEDA catalog, or classified in merging or post-merger stage by Barrera-Ballesteros et al. (2015).

Table 3.2. ^{13}CO observation and galaxy properties in the extended EDGE ^{13}CO sample

No.	Galaxy Name	F_{13} (Jy km/s)	F_{12}/F_{13}	$\langle\sigma(I_{13})\rangle$ [a]	F_{60}/F_{100} [b]	Inter [c]
1	IC1199	7.81 ± 2.48	10.74 ± 3.46	0.04	0.36 ± 0.07	0
2	IC4566	15.85 ± 3.48	6.19 ± 1.40	0.06	1.00 ± 1.41	0
3	NGC0496	10.11 ± 2.69	7.68 ± 2.07	0.04	0.30 ± 0.05	0
4	NGC3815	10.27 ± 2.69	8.33 ± 2.22	0.04	0.44 ± 0.44	0
5	NGC5016	12.14 ± 3.12	10.45 ± 2.72	0.05	0.37 ± 0.01	0
6	NGC5784	9.35 ± 2.32	6.48 ± 1.65	0.03	0.27 ± 0.01	0
7	NGC6004	16.22 ± 3.81	7.71 ± 1.85	0.08	0.31 ± 0.02	0
8	NGC6301	13.18 ± 3.92	8.40 ± 2.52	0.08	0.21 ± 0.03	0
9	UGC03539	10.48 ± 2.77	10.02 ± 2.68	0.03	0.40 ± 0.07	0
10	UGC03969	11.36 ± 3.34	7.64 ± 2.28	0.04	0.42 ± 0.06	0
11	UGC08107	10.72 ± 3.46	13.96 ± 4.53	0.05	0.28 ± 0.05	1
12	UGC08267	9.57 ± 2.87	9.80 ± 2.97	0.03	0.27 ± 0.05	0
13	UGC09537	16.93 ± 3.44	4.27 ± 0.90	0.05	0.28 ± 0.04	0
14	UGC09665	9.94 ± 2.73	11.59 ± 3.22	0.04	0.36 ± 0.03	0
15	UGC09759	7.67 ± 2.50	11.22 ± 3.70	0.03	0.29 ± 0.03	0
16	UGC10710	10.76 ± 3.12	6.29 ± 1.86	0.04	0.21 ± 0.04	0

[a] Mean 1σ noise of I_{13} using dilated ^{12}CO masks of the galaxy.

[b] IRAS IR color from NED.

[c] The assignment of interacting galaxies (1) or isolated galaxies (0). The interacting galaxies are those labeled as "multiple" in the HyperLEDA catalog, or classified in merging or post-merger stage by Barrera-Ballesteros et al. (2015).

beam of 7″) detected both in ^{13}CO and ^{12}CO with S/N > 3. We summarize the galaxy properties and ^{13}CO observations of these 42 galaxies in Table 3.1.

The ^{13}CO intensity maps of the sample galaxies are shown in Figure 3.2. ^{13}CO emission in these resolved maps are detected both in galaxy centers and disks in most of the sample galaxies. Because ^{13}CO is much weaker and has lower S/N than ^{12}CO in our observation, ^{13}CO intensity (I_{13}) detections with S/N > 3, shown as the magenta contours are less widespread than ^{12}CO intensity (I_{12}) detections shown as the first level of black contours. In particular, the ^{13}CO detections are usually confined to regions where I_{12} is well detected. The peaks of ^{13}CO are also mostly located within regions with bright ^{12}CO. However, the detailed ^{13}CO intensity maps show substantially different features from the ^{12}CO intensity, an indication that the resolved $\mathcal{R}$ varies across each galaxy.

3.3.2 ^{13}CO flux spectra and integrated fluxes

We stack all the ^{13}CO spectra within the field-of-view to obtain the flux spectrum for each the galaxy. The flux in each channel is the total masked ^{13}CO intensity for all the pixels in the channel. We calculate ^{13}CO integrated fluxes (F_{13}) from these masked spectra. We obtain 56 galaxies with S/N(F_{13}) > 3. Except for NGC 0523 and NGC 5406, all of the other 40 galaxies in the EDGE ^{13}CO sample are detected with S/N(F_{13}) > 3. We list in Table 3.2 the galaxy properties and ^{13}CO fluxes of the 16 additional galaxies with S/N(F_{13}) > 3 that are not included in the EDGE ^{13}CO sample described in Section 3.3.1. We refer to the 56 galaxies as the "extended" EDGE ^{13}CO sample. The spectra of the extended EDGE ^{13}CO sample are shown in Figure 3.4.

3.3.3 Line ratios

We use ^{12}CO and ^{13}CO integrated fluxes calculated within the dilated ^{12}CO mask to obtain the flux ratio F_{12}/F_{13} for each galaxy in the extended EDGE ^{13}CO sample. The flux ratio indicates the overall line ratio of a galaxy, comparable with the unresolved $\mathcal{R}$ obtained from single-dish measurements assuming missing flux from the interferometric observation is negligible. The ^{12}CO fluxes and their uncertainties can be found in the second column of Table 2 in Bolatto et al. (2017). The values of F_{13} and F_{12}/F_{13} are tabulated in the third and fourth columns of Tables 3.1 and 3.2.

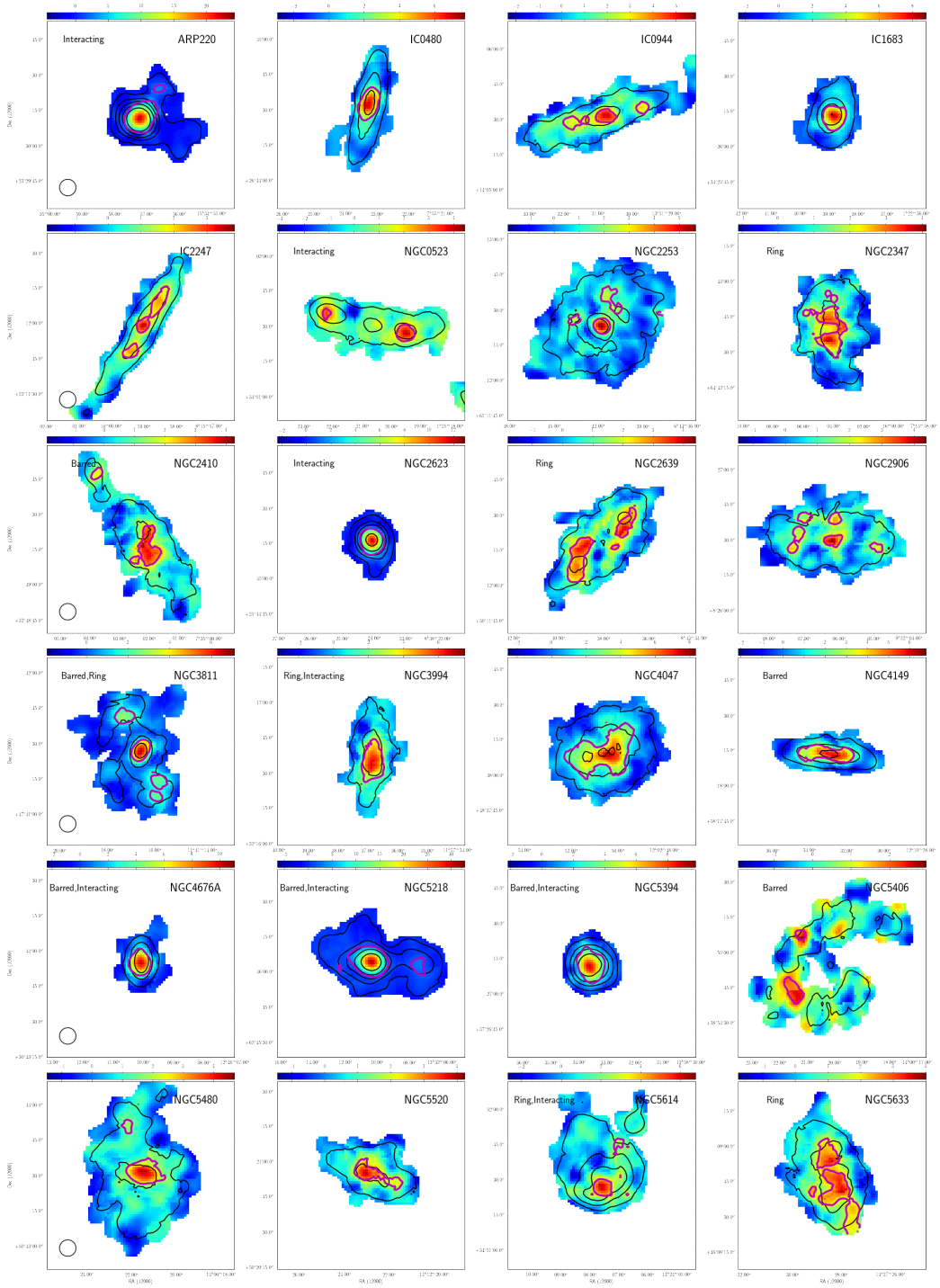

Figure 3.2. ^{13}CO intensity maps of the sample galaxies from the EDGE survey. The magenta contours overlaid show the ^{13}CO intensity observed with S/N > 3, while the black contours levels show the ^{12}CO intensity with contour levels of [1, 4, 8, 16] $\times 3\sigma(I_{13})$. The morphology features such as "bar", "ring", and "interacting" are shown in the left corner if applicable. The "barred" and "ring" features are labeled in the HyperLEDA catalog (Makarov et al., 2014), and interacting galaxies are labeled as "multiple" in the HyperLEDA catalog, or those classified in merging or post-merger stage by Barrera-Ballesteros et al. (2015). The beam size of 7″ are shown in the first panel of each row. The maps of remaining sample galaxies are in Figure 3.3.

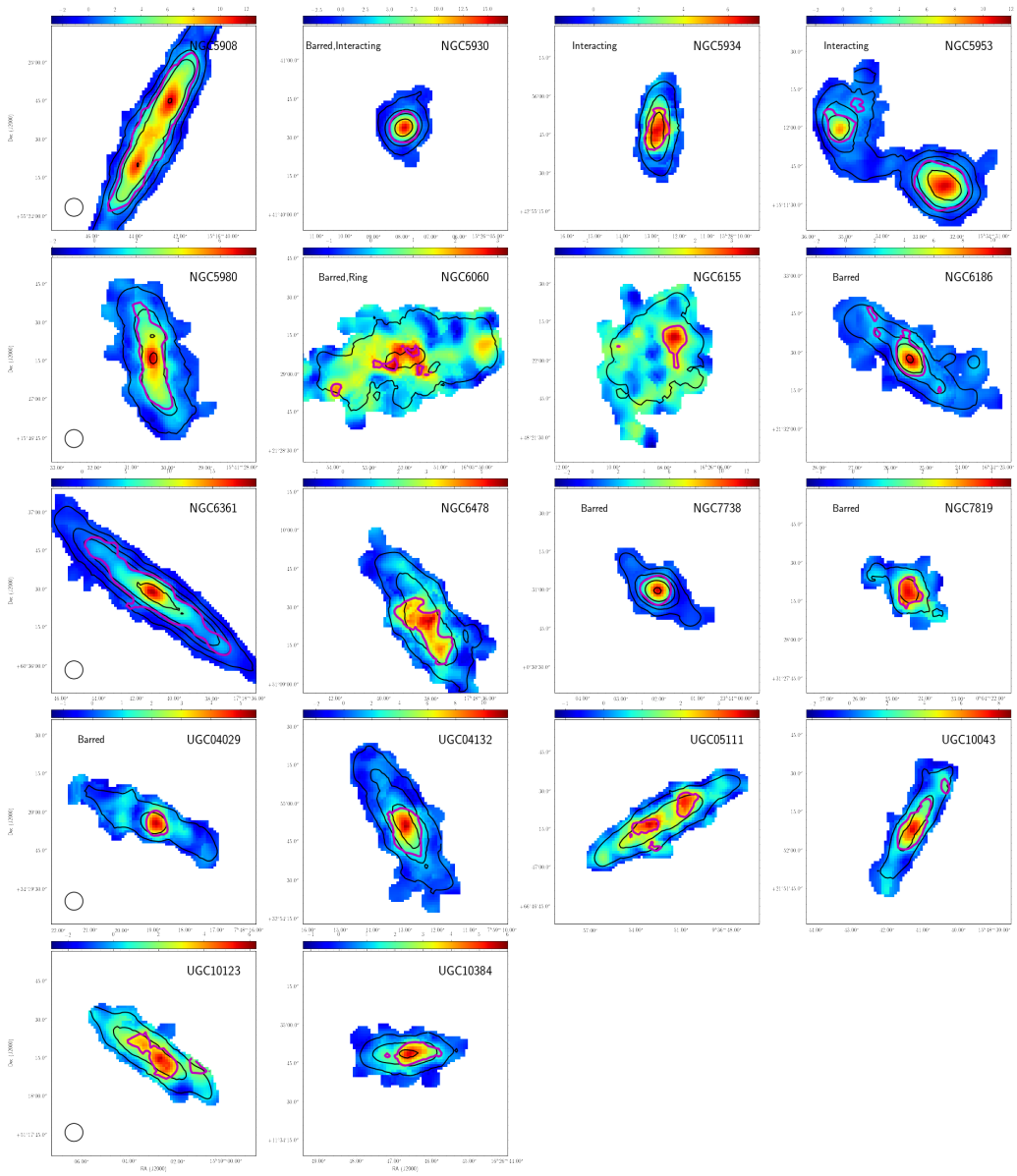

Figure 3.3. ^{13}CO intensity maps of the sample galaxies from the EDGE survey (continued). See captions in Figure 3.2

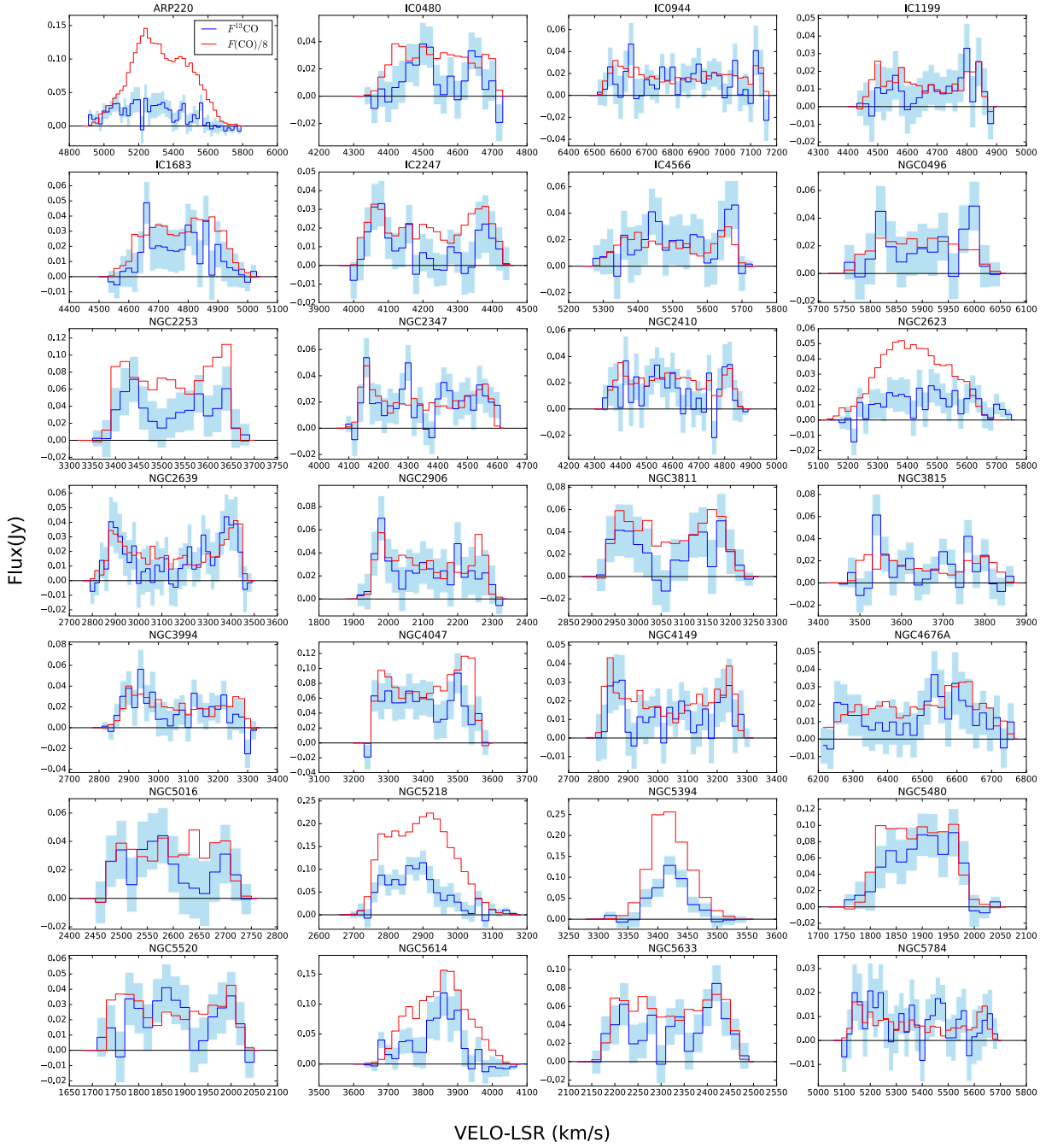

Figure 3.4. ^{13}CO flux spectra for the 56 galaxies the extended EDGE sample. The blue lines show the ^{13}CO flux in each channel obtained using the dilated ^{12}CO masks, and red lines are the ^{12}CO flux resulting from the same masks scaled down to a factor of 8. The light blue shaded regions represent 1σ uncertainty of ^{13}CO flux.

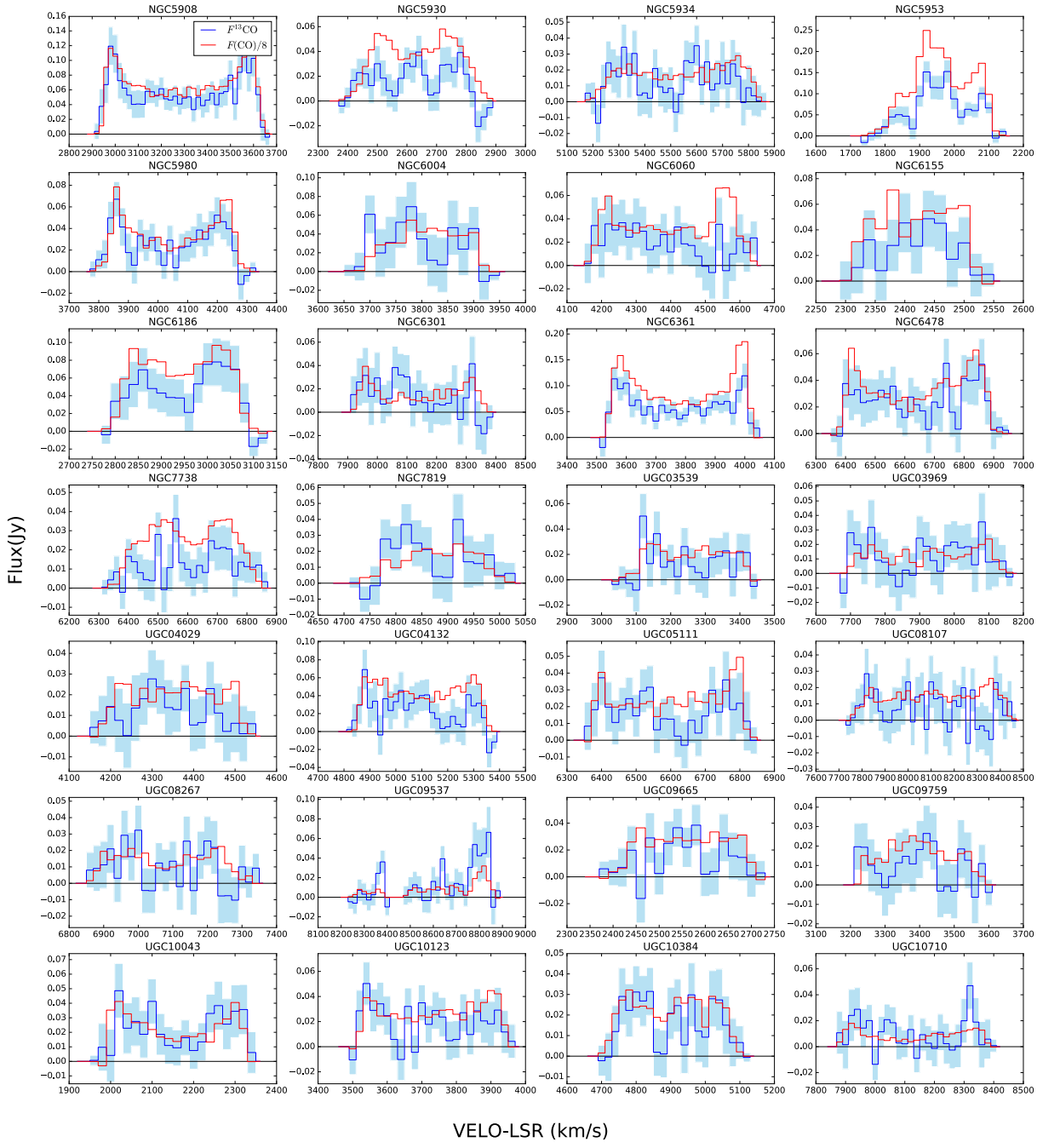

Figure 3.5. ^{13}CO flux spectra for the 56 galaxies the extended EDGE sample (continued). See captions in Figure 3.4

For the 42 galaxies in the EDGE ^{13}CO sample, we derive the resolved $\mathcal{R}$ from I_{13} and I_{12} of each cell. We derive a weighted mean value for the resolved intensity ratio $\langle\mathcal{R}\rangle$ for each galaxy. $\langle\mathcal{R}\rangle$ is the mean of the resolved $\mathcal{R}$ weighted by I_{13} for cells with I_{13} above the detection threshold of 3σ (see Equation 2.2). The weighted mean and the corresponding weighted standard deviation characterize the resolved $\mathcal{R}$ observed for each galaxy. The values of $\langle\mathcal{R}\rangle$ and the standard deviation are listed in the fifth column of Table 3.1.

Figure 3.6 shows the comparison between $\langle\mathcal{R}\rangle$ and the flux ratio F_{12}/F_{13} for the EDGE ^{13}CO sample. The two kinds of line ratios clearly show a positive trend in the left panel. The flux ratio F_{12}/F_{13} of a galaxy is generally 1 to 2 times larger than its value of $\langle\mathcal{R}\rangle$ in our sample. This is because only cells with higher ^{13}CO above the detection threshold, and therefore lower $\mathcal{R}$, are included in the calculation of $\langle\mathcal{R}\rangle$, while the flux ratio F_{12}/F_{13} also takes regions below the threshold into account. The scaling factor between F_{12}/F_{13} and $\langle\mathcal{R}\rangle$ varies in our sample. This suggests that the effects of the sensitivity bias on $\langle\mathcal{R}\rangle$ could be different among the galaxies. We refer to the ratio of the number of cells with ^{13}CO detected to that of ^{12}CO detected in a galaxy as the overall ^{13}CO detection fraction. As shown in the right panel of Figure 3.6, the ratio of F_{12}/F_{13} to $\langle\mathcal{R}\rangle$ decreases with the overall ^{13}CO detection fraction. $\langle\mathcal{R}\rangle$ in galaxies with smaller overall ^{13}CO detection fractions are more likely biased due to the limited sensitivity of resolved I_{13} and $\mathcal{R}$ than those with larger detection fractions. Therefore the decreasing trend implies that the sensitivity bias has a larger effect on $\langle\mathcal{R}\rangle$ if resolved $\mathcal{R}$ are detected in a smaller fraction of the cells in a galaxy.

3.3.4 Global line ratios and galaxy properties

The flux spectra (Figure 3.4 and Figure 3.5) indicate that the ^{12}CO to ^{13}CO line ratio in our sample varies among different galaxies. We use the flux ratio F_{12}/F_{13} to investigate the relation of the line ratio to the global galaxy parameters in the extended EDGE ^{13}CO sample. Figure 3.7 plots distributions of galaxy properties for the EDGE sample, the extended EDGE ^{13}CO sample, and the EDGE ^{13}CO sample. The distributions of the (extended) EDGE ^{13}CO samples are slightly biased to higher values of M_*, SFR, and metallicity, mainly because only the galaxies with higher ^{12}CO flux and therefore stronger corresponding ^{13}CO are selected. The extended EDGE ^{13}CO sample

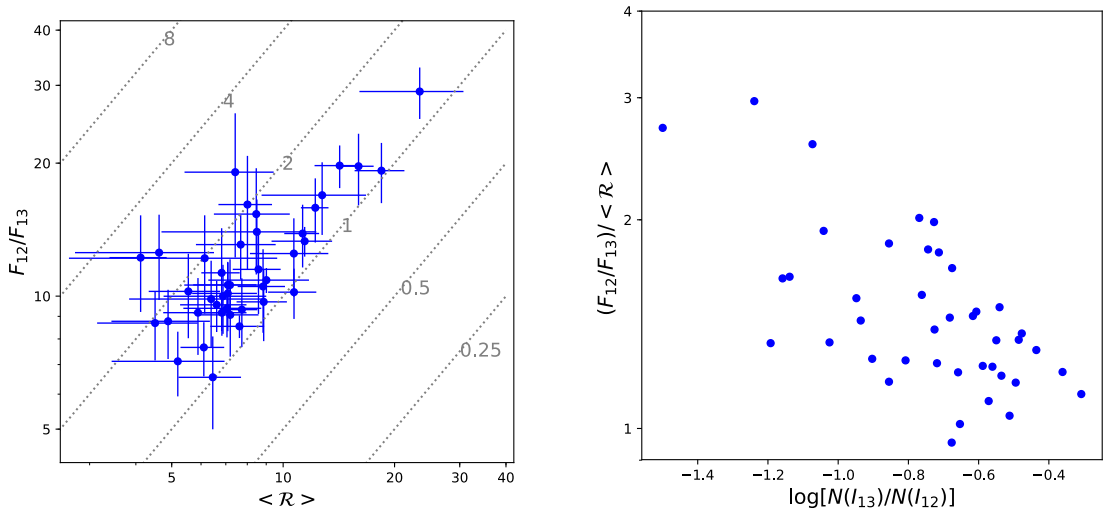

Figure 3.6. Comparison between flux ratio F_{13} and weighted mean of resolved $\mathcal{R}$ ($\langle\mathcal{R}\rangle$) for the EDGE ^{13}CO sample. Left: The horizontal error bars show the weighted standard deviation of resolved $\mathcal{R}$, while the vertical error bars show the measurement uncertainty of F_{12}/F_{13}. Constant scaling factors are shown as the gray dotted lines. Right: scaling factor between F_{12}/F_{13} and $\langle\mathcal{R}\rangle$ as a function of ratio of the number of cells detected in I_{13} with S/N> 3 to the number of cells detected in I_{12} with S/N> 3. The flux ratios F_{12}/F_{13} are generally 1 to 2 times larger than $\langle\mathcal{R}\rangle$, and the ratio of F_{12}/F_{13} to $\langle\mathcal{R}\rangle$ decreases when resolved I_{13} and $\mathcal{R}$ are measured with more cells.

has 16 more galaxies with weaker ^{12}CO fluxes than the EDGE ^{13}CO sample, but the distributions of M_*, SFR, and metallicity of the two samples are similar.

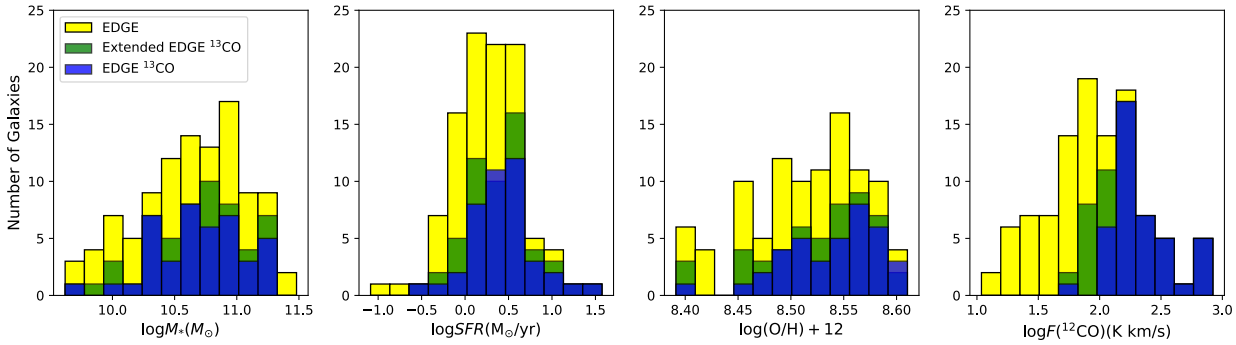

Figure 3.7. Distribution of galaxy parameters in the EDGE sample (yellow), the extended EDGE ^{13}CO sample (green), and the EDGE ^{13}CO sample (blue). The distributions of the EDGE ^{13}CO sample are slightly biased to higher stellar mass, SFR, and metallicity.

Figure 3.8 illustrates distributions of F_{12}/F_{13} and $\langle\mathcal{R}\rangle$ splitting the sample by with different morphological features. The ratios in the galaxies having bars or rings are similar to the other galaxies without these features. However, the interacting galaxies show significantly higher F_{12}/F_{13} and $\langle\mathcal{R}\rangle$ than the isolated galaxies. The median values of F_{12}/F_{13} for the 11 interacting galaxies

and the other 45 isolated galaxies are 17.37 and 10.96 respectively. The median of $\langle\mathcal{R}\rangle$ for the interacting galaxies is 12.67, also significantly higher than the median value of 6.98 in isolated galaxies. In further investigations of F_{12}/F_{13} and $\mathcal{R}$, we will separate the interacting galaxies from the EDGE ^{13}CO sample to highlight their systematic differences.

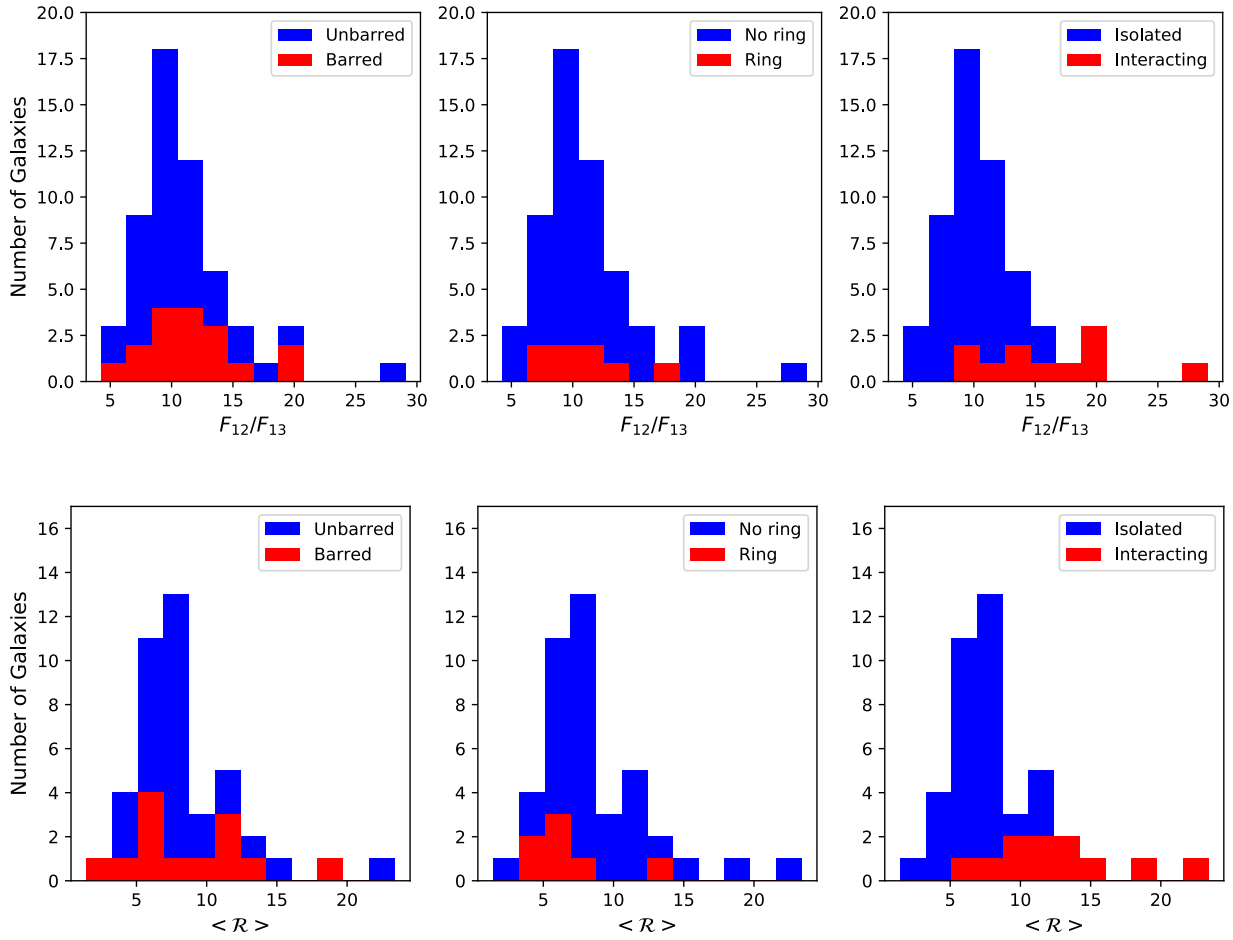

Figure 3.8. Comparisons of distributions of line ratios with different morphology features. The top panels show the distribution of F_{12}/F_{13}, and the bottom panels show that of $\langle\mathcal{R}\rangle$. The panels on the left compares the barred galaxies and unbarred galaxies, the middle panels show the comparison of galaxies having rings and those without rings, and the right panels show distributions of interacting galaxies and interacting galaxies. Interacting galaxies tend to have larger F_{12}/F_{13} and $\langle\mathcal{R}\rangle$ than the isolated galaxies. The ratios with bars or rings are similar to the ratios in other galaxies without these features.

Figure 3.9 summarizes F_{12}/F_{13} as functions of the global galaxy parameters. We highlight the interacting galaxies in EDGE ^{13}CO sample in red in Figure 3.9; the other isolated galaxies are shown in blue. Spearman's rank correlation coefficients r and the probabilities of the null hypothesis P_0 are shown in each panel; the black text shows the results of correlation tests for all

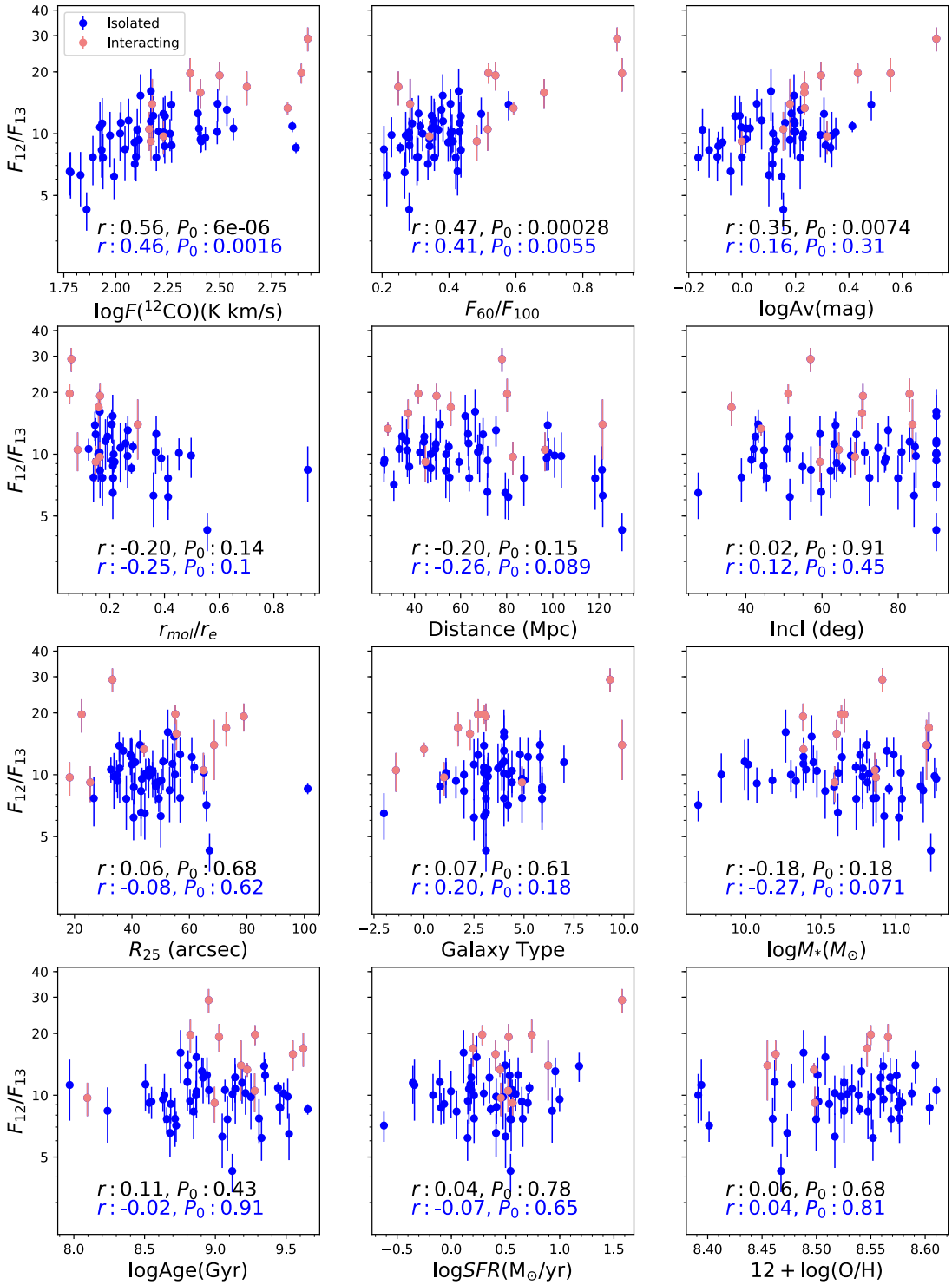

Figure 3.9. F_{12}/F_{13} as functions of galaxy parameters for the 56 galaxies in the extended EDGE ^{13}CO sample. Blue symbols show the isolated galaxies and the red symbols show the interacting galaxies. The vertical bars show the uncertainty of F_{13}. The panels from the top left to the bottom right are (1) total flux of ^{12}CO (2) the far-IR flux ratio at 60 and 100 μm from NED; (3) nebular extinction from Pipe3D; (4) ratio of radius enclosing 50% of the molecular mass to equivalent radius; (5) luminosity distance in Mpc computed from redshift for gas lines assuming $H_0 = 70, \Omega_m = 0.27, \Omega_l = 0.73$; (6) morphology inclination from HyperLEDA; (7) apparent B radius from HyperLEDA; (8) morphological type from HyperLEDA; (9) total stellar mass from Pipe3D; (10) mean stellar age from Pipe3D; (11) total SFR from Hα corrected by extinction; (12) O3N2-based metallicity.

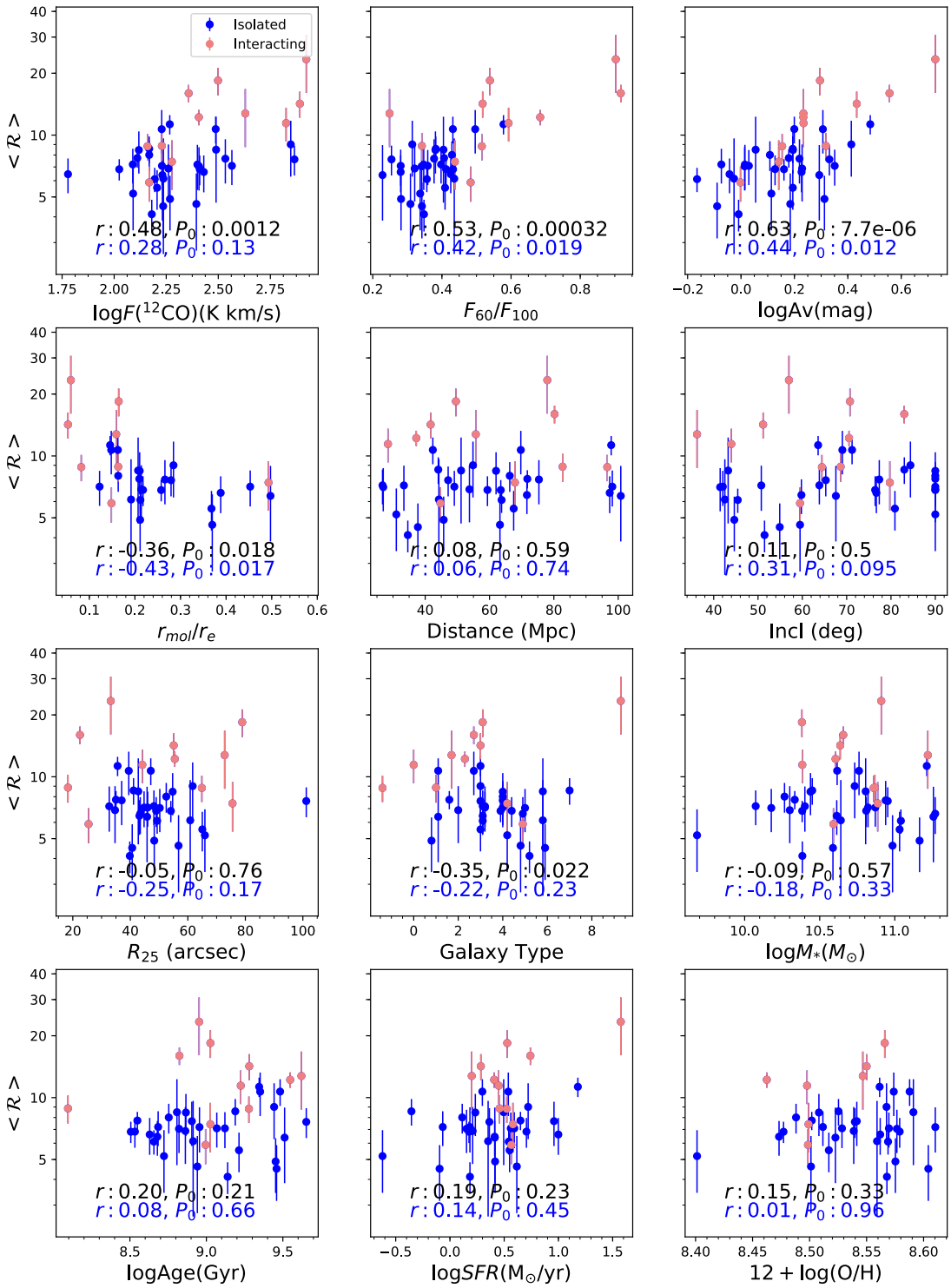

Figure 3.10. $\langle\mathcal{R}\rangle$ as functions of galaxy parameters for the 42 galaxies in the EDGE ^{13}CO sample. Blue symbols show the isolated galaxies and the red symbols show the interacting galaxies. Error bars on the symbols show weighted standard deviation of resolved $\mathcal{R}$. See the caption of Figure 3.9 for descriptions of x axis of each panel.

the 56 galaxies in the extended EDGE ^{13}CO sample, and the blue text shows the results for the isolated galaxies only.

The top left panel of Figure 3.9 shows the F_{12}/F_{13} increases with the total flux of ^{12}CO. This trend is likely due to bias of the extended EDGE ^{13}CO sample shown in the last panel of Figure 3.7. For galaxies with low F_{12}, the extended EDGE ^{13}CO sample is limited to higher F_{13} and lower F_{12}/F_{13}. As shown in the top middle panel, F_{12}/F_{13} increases with F_{60}/F_{100}; higher F_{12}/F_{13} are associated with higher dust temperature implied by larger F_{60}/F_{100} values. F_{12}/F_{13} and $\langle\mathcal{R}\rangle$ also tend to increase with the dust extinction $A_{\rm v}$ (top right panels in Figure 3.9). Interacting galaxies might have strong impacts on both of the trends, as these galaxies also show higher IR color and dust extinction than the isolated galaxies. Excluding the interacting galaxies from the sample, F_{12}/F_{13} in the isolated galaxies does not correlate with $A_{\rm v}$. In contrast, the correlation between F_{12}/F_{13} and F_{60}/F_{100} are still significant above 2σ level ($P_0 < 0.05$). Although our sample includes a wide variety of galaxies, no significant correlations above 2σ level are found between F_{12}/F_{13} and the rest of the galaxy parameters shown in Figure 3.9.

We also show the global correlations based on the I_{12}-weighted mean $\langle\mathcal{R}\rangle$ in Figure 3.10. Unlike F_{12}/F_{13}, $\langle\mathcal{R}\rangle$ does not show a dependence on F_{12} in isolated galaxies. This is probably because the $\langle\mathcal{R}\rangle$ is based on local measurements of both I_{12} and I_{13}, which depends less on the global quantities of F_{12} and F_{13}. Besides F_{60}/F_{100}, $\langle\mathcal{R}\rangle$ also correlates with dust extinction (top right panel) and the molecular gas concentration (left panel in second row) above 2σ significance levels in the isolated galaxies. There is no correlation between $\langle\mathcal{R}\rangle$ and the other global properties. We cannot exclude the possibility that these correlations we find are due to the sample bias to lower $\langle\mathcal{R}\rangle$ for galaxies with low F_{60}/F_{100}, low dust extinction, or more extended distribution of the molecular gas. Nevertheless, the results suggest that the variations in global ratios F_{12}/F_{13} and $\langle\mathcal{R}\rangle$ among galaxies are more likely associated with the dust and molecular gas properties than the stellar and ionized gas properties on galactic scale.

3.3.5 Resolved $\mathcal{R}$ and local properties on kpc scales

In this section, we investigate how $\mathcal{R}$ correlates with the resolved properties on kpc scales. We examine the dependence of $\mathcal{R}$ on CO measurements from the EDGE survey such as I_{12}, I_{13}, and

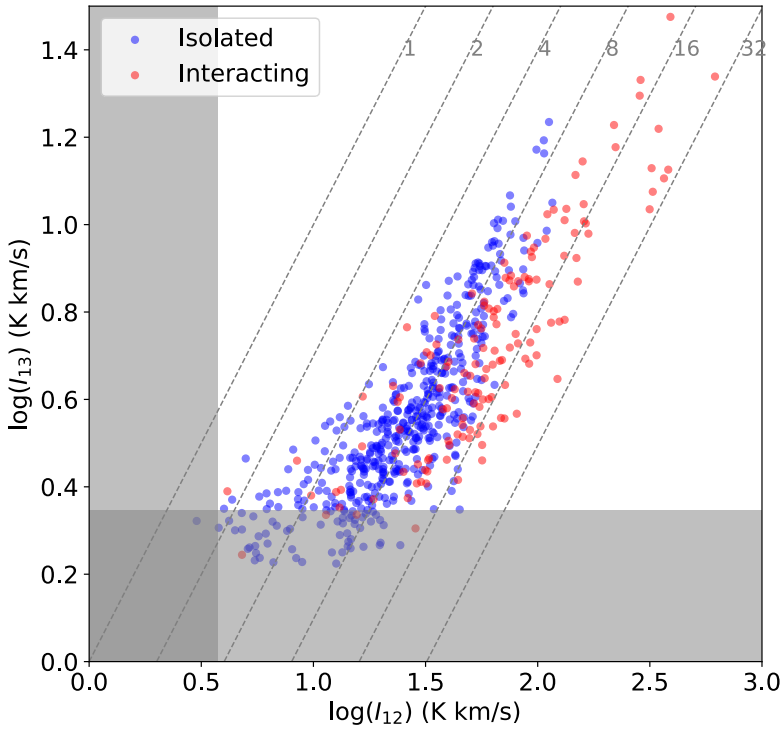

Figure 3.11. I_{13} as a function of I_{12} for the 42 galaxies in the EDGE ^{13}CO sample. The blue dots show the I_{13} detections with S/N $>$ 3 in the 31 isolated galaxies, while the red ones are the I_{13} detected in the 11 interacting galaxies. The typical detection limits of ^{13}CO and ^{12}CO are shown as the upper and right boundaries of the gray shaded regions respectively. Constant $\mathcal{R}$ values of [1,2,4,8,16,32] are shown as gray dashed lines.

line width measured from I_{12}-weighted moment 2. In addition, with the CALIFA IFU data at the same resolution as the CO observations in the EDGE samples, we are able to investigate the relations of resolved $\mathcal{R}$ to the local properties of stars and ionized gas on kpc scales.

3.3.5.1 Correlations between $\mathcal{R}$ and resolved properties

In Figure 3.11, we present the distribution of I_{12} and I_{13} for all the 631 cells where both I_{12} and I_{13} are detected with S/N $>$ 3 in the EDGE ^{13}CO sample. I_{13} is generally $\sim$ 8 times weaker than I_{12} in the isolated galaxies ($\mathcal{R}\sim$ 8). The range of I_{12} in the interacting galaxies is wider than in the isolated galaxies. I_{12} in the interacting galaxies also appears to be higher than those in the isolated galaxies typically. The difference in the I_{13} distributions between interacting galaxies and isolated galaxies are less obvious than the differences in the I_{12} distributions, although the largest I_{13} values in our sample are ubiquitously found in the interacting galaxies.

Figure 3.12 shows the correlations between resolved $\mathcal{R}$ and observed CO properties. $\mathcal{R}$ strongly

depends on I_{12} (left panel). $\mathcal{R}$ also slightly increases with I_{13} (middle panel) and moment 2 (right panel). The Spearman's rank correlation coefficients r and the probabilities of no correlation P_0 are shown in the first three rows of Table 3.14. Excluding the 144 cells from the 11 interacting galaxies, the correlations between $\mathcal{R}$ and these three parameters are still significant in the isolated galaxies. The strong apparent dependence on I_{12} is due to the sensitivity bias to lower values in our $\mathcal{R}$ measurements when I_{12} are weak. Since I_{13} and moment 2 also increases with I_{12}, these trends could be resulting from this selection bias due to the limited sensitivity at lower I_{12}. We probe the sensitivity bias and its effects on the correlations between resolved $\mathcal{R}$ and other properties in Section 3.3.5.2.

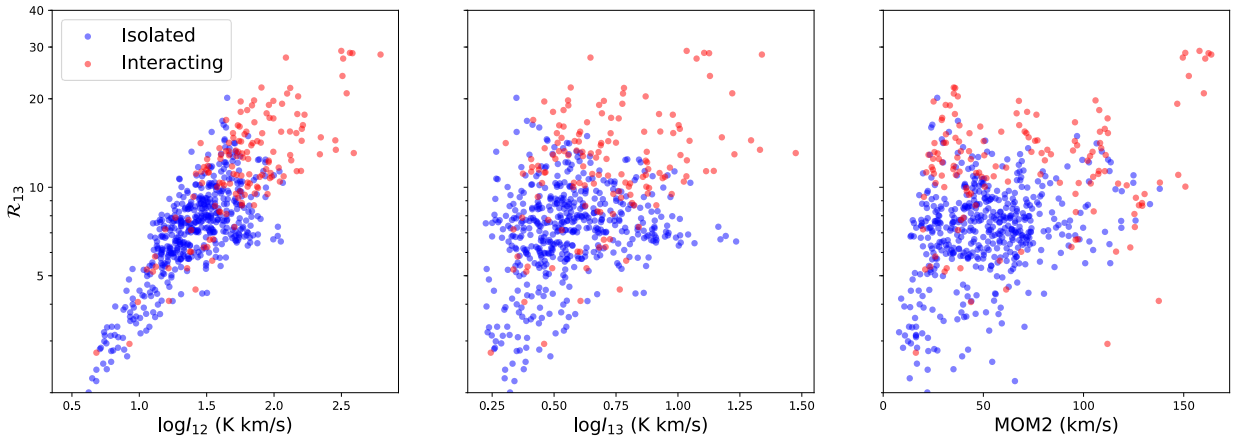

Figure 3.12. Resolved $\mathcal{R}$ and its dependencies on observed molecular gas properties for all the 43 galaxies in the EDGE ^{13}CO sample. The blue dots show the I_{13} detections with S/N > 3 in the 31 isolated galaxies, while the red ones are the I_{13} detections for the 11 interacting galaxies. Left: resolved $\mathcal{R}$ vs. I_{12}. Middle: resolved $\mathcal{R}$ vs. I_{13}. Right: $\mathcal{R}$ vs. moment 2 (I_{12}-weighted second moment).

To investigate the correlation between $\mathcal{R}$ and resolved properties of stars and ionized gas such as stellar surface density and star formation rate surface density, we remove 70 cells in the 7 edge-on isolated galaxies (inclination = 90°) from the EDGE ^{13}CO sample. Less cells are available for SFR surface density and gas metallicity than the others, because these quantities are only calculated for star-forming regions that are more restrictive than the others. The distributions of the stellar and ionized gas properties of the selected cells are shown in Figure 3.13. The cells with measurable $\mathcal{R}$ span narrower ranges of stellar and ionized gas properties than the cells with I_{12} detected. The stellar surface density, stellar age, dust extinction, SFR surface density, and gas metallicity of I_{13} detections are biased toward higher values comparing with the distributions of I_{12} detections.

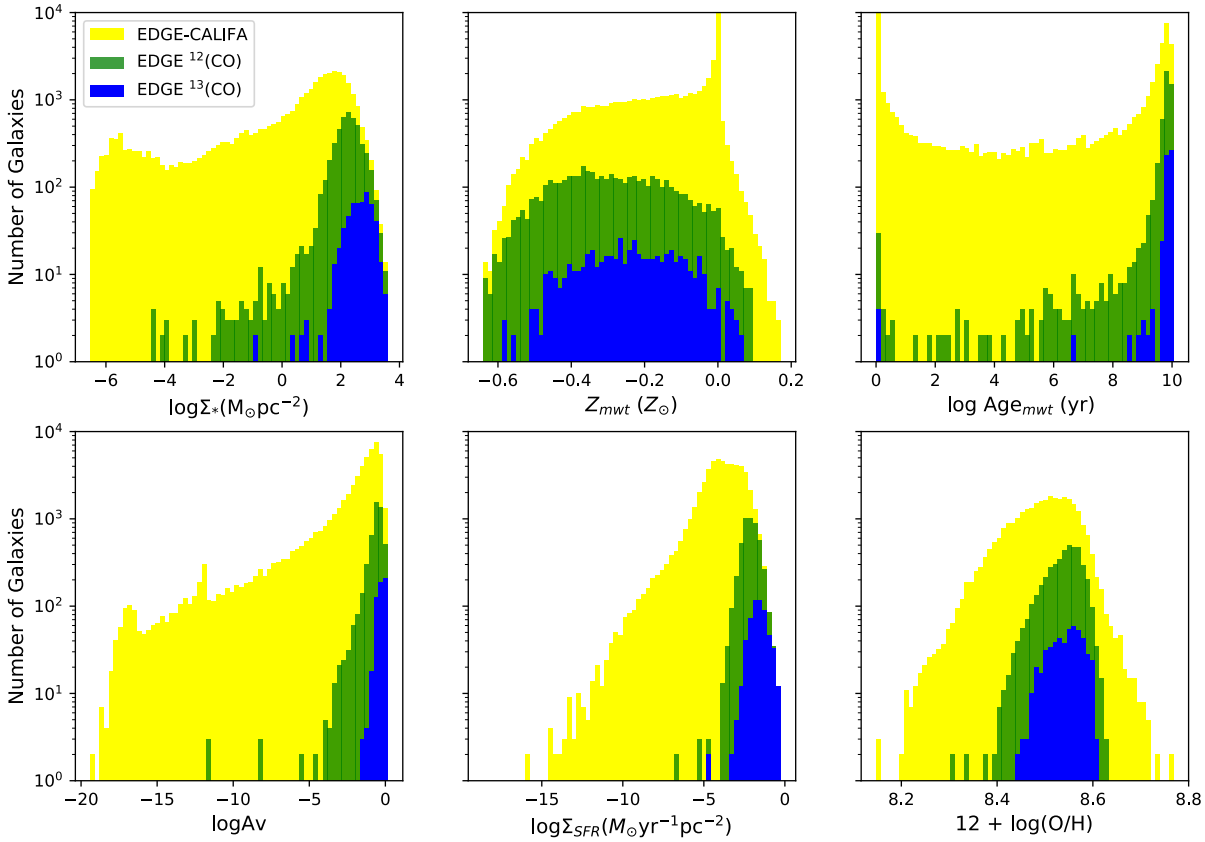

Figure 3.13. Distributions of resolved properties derived from the CALIFA IFU observation. The ranges of cells detected ^{12}CO (green) are narrower than the ranges of all cells from the EDGE-CALIFA survey (yellow). I_{13} detections used for the investigation of correlations are biased to higher ends of all of the six properties compared to the I_{12} detections. The panels from the top-left to the bottom-right are: (1) Stellar mass derived by PIPE3D; (2) Mass weighted stellar metallicity; (3) Mass weighted age of the stellar population; (4) Dust extinction of the stellar population; (5) SFR surface density derived from Ha flux; (6) Gas metallcity 12+log(O/H) derived from O3N2. See detailed descriptions of the quantities in Section 3.2.4.

Because the I_{12} detections are also biased toward higher ends compared with the distribution of all the cells in the EDGE-CALIFA survey, the biases in the stellar and ionized gas properties of I_{13} detections are probably due to the requirements of higher I_{12}.

Figure 3.19 shows $\mathcal{R}$ vs. the properties of stellar population and ionized gas derived from CALIFA. The Spearman correlation coefficients and their significances are shown in Table 3.14. Resolved $\mathcal{R}$ values weakly correlate with stellar surface density, metallicity of stars, dust attenuation, and SFR surface density above 3σ significance ($P_0 < 0.003$). However, since these properties also increase with I_{12} and there is a strong dependence of $\mathcal{R}$ on I_{12} due to the sensitivity bias, these correlations can also be due to the effects of sensitivity bias.

Moreover, similar to the results from the flux ratios F_{12}/F_{13}, typical resolved $\mathcal{R}$ in the interacting

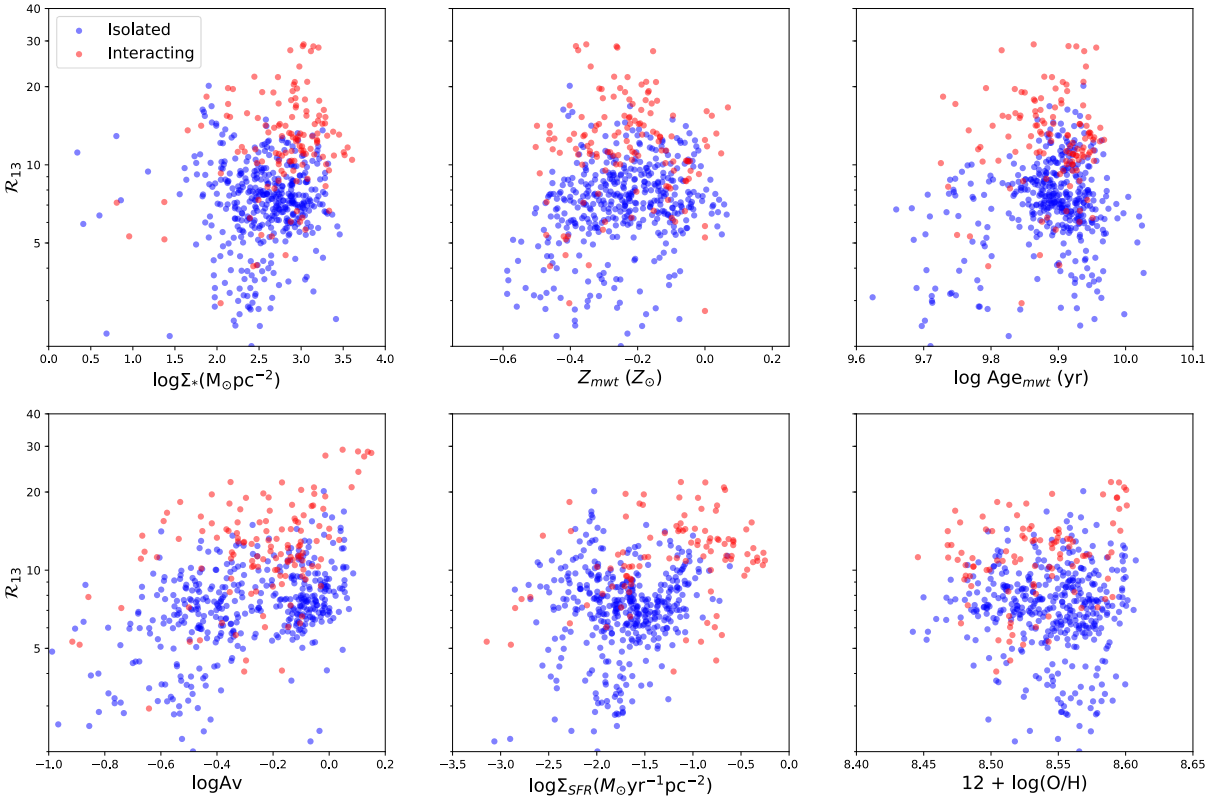

Figure 3.14. Resolved $\mathcal{R}$ as functions of stellar and ionized gas properties. The blue dots show the I_{13} detections with S/N > 3 in the isolated galaxies, while the red ones are the I_{12} detections for the interacting galaxies. See descriptions of each x axis in 3.13.

galaxies is also higher than $\mathcal{R}$ in isolated galaxies (Figure 3.12 and Figure 3.19). The higher $\mathcal{R}$ values in the interacting galaxies are also present if the sample is binned by resolved properties other than I_{12}. The ranges of these resolved properties in the interacting galaxies are also similar to the ranges in the isolated galaxies. In addition, unlike the isolated galaxies, $\mathcal{R}$ in interacting galaxies does not significantly correlate with moment 2 and dust extinction. On the other hand, $\mathcal{R}$ slightly increases with SFR surface density and decreases with gas metallicity in the interacting galaxies with significance level above 2σ, while these two correlations are not found in the isolated galaxies. This implies that on kpc scales the molecular gas opacity and/or the abundance [^{12}CO/^{13}CO] in the interacting galaxies are more sensitivity to the local stellar feedback and gas metallicity than in the isolated galaxies.

Table 3.3. Correlation coefficients between $\mathcal{R}$ and local propertiess

Local property	All galaxies				Isolated galaxies				Interacting galaxies			
	r_s [a]	P_0 [b]	N [c]	N_g [d]	r_s [e]	P_0 [f]	N [g]	N_g [h]	r_s [i]	P_0 [j]	N [k]	N_g [l]
$\log(I_{12})$ (K km/s)	0.76	< 0.001	631	42	0.68	< 0.001	487	31	0.29	< 0.001	144	11
$\log(I_{13})$ (K km/s)	0.36	< 0.001	631	42	0.27	< 0.001	487	31	0.29	0.002	144	11
MOM2 (km/s)	0.29	< 0.001	631	42	0.27	< 0.001	487	31	0.11	0.21	144	11
$\log \Sigma_*(\mathrm{M}_\odot \mathrm{pc}^{-2})$	0.19	< 0.001	546	35	0.03	0.61	415	24	0.17	0.053	131	11
Z ($Z_\odot$)	0.15	< 0.001	552	35	0.22	< 0.001	417	24	-0.03	0.69	135	11
log Age (yr)	0.07	0.087	552	35	0.03	0.49	417	24	0.13	0.13	135	11
log Av	0.39	< 0.001	631	42	0.41	< 0.001	417	24	0.26	< 0.001	135	11
$\log \Sigma_{SFR}(M_\odot \mathrm{yr}^{-1} \mathrm{pc}^{-2})$	0.26	< 0.001	504	34	0.07	0.15	403	24	0.23	0.021	101	11
log(O/H)+12	-0.05	0.23	504	34	-0.05	0.35	403	24	0.27	0.006	101	11

[a] Spearman's rank correlation coefficients between $\mathcal{R}$ and local parameters in all the galaxies.

[b] Probability of the null hypothesis of no correlation between $\mathcal{R}$ and local parameters in all the galaxies.

[c] Number of cells used in all the galaxies available for the correlation test.

[d] Number of all the galaxies available for the correlation test.

[e] Spearman's rank correlation coefficients between $\mathcal{R}$ and local parameters in isolated galaxies.

[f] Probability of the null hypothesis of no correlation between $\mathcal{R}$ and local parameters in isolated galaxies.

[g] Number of cells used in isolated galaxies available for the correlation test.

[h] Number of isolated galaxies available for the correlation test.

[i] Spearman's rank correlation coefficients between $\mathcal{R}$ and local parameters in interacting galaxies.

[j] Probability of the null hypothesis of no correlation between $\mathcal{R}$ and local parameters in interacting galaxies.

[k] Number of cells used in interacting galaxies available for the correlation test.

[l] Number of interacting galaxies available for the correlation test.

3.3.5.2 Sensitivity bias of I_{13} and $\mathcal{R}$

We use two simple models to examine the possible effects of sensitivity bias on the resolved correlations investigated in this study. In the models, we assume the mean $\mathcal{R}$ throughout all the I_{12} bins is a constant value for the galaxies. We first consider a constant scatter model, in which the distribution of $\mathcal{R}$ in each I_{12} bin obeys a Gaussian distribution, and the variance of $\mathcal{R}$ in each bin is also a constant value regardless of I_{12}. For the isolated galaxies, we adopt the constant $\mathcal{R}$ value of 10 and the constant scatter of 0.5 in this model. $\mathcal{R}$ in the interacting galaxies are modeled in the same manner as the isolated galaxies but with higher constant $\mathcal{R}$ of 10 and larger scatter of 5.0 assumed. The second model is motivated by the apparent decreasing scatter of $\mathcal{R}$ as I_{12} increases. The measured $\mathcal{R}$ on kpc scales are considered as the average value of $\mathcal{R}$ for a large number of cloudlets on smaller scales within a beam; each cloudlet emitting the same amount of I_{12} and their I_{13} is an independent and identically distributed random variable. The inverse of $\mathcal{R}$ in each I_{12} bin follows a Gaussian distribution in the cloudlet model; the mean of $1/\mathcal{R}$ is a constant but the variances is proportional to $1/I_{12}$ (Cao et al., 2017). Similar to the constant scatter model, the assumed $\mathcal{R}$ values are 10 and 20 for the isolated and interacting galaxies in the cloudlet model. The standard deviation of $1/I_{12}$ measured in the reference bin $I_{12\mathrm{ref}} \sim 90$ K km/s is 0.105. Figure 3.15 shows the distributions of I_{12} and I_{13} resulting from the models. The simple models reproduce similar characteristics of I_{13} as a function of I_{12} to the observation as shown in Figure 3.11.

For the cells detected in I_{12}, we simulate I_{13} of each cells by randomly drawing the $\mathcal{R}$ or $1/\mathcal{R}$ distributions assumed by the models. We then add the measurement uncertainty to the modeled I_{13}. The $\mathcal{R}$ is calculated by dividing the observed I_{12} by the modeled I_{13}, and the uncertainty of $\mathcal{R}$ is then calculated by error propagation. Except for I_{13} and $\mathcal{R}$, all the other resolved properties of the cell are kept. For each simulation, we select the cells with modeled I_{13} detected by S/N > 3 and calculate the Spearman's rank correlation coefficients r_s and the P_0 values between the modeled $\mathcal{R}$ and other resolved properties.

We repeat the simulations 1000 times for each model, and the distributions of the r and P_0 values are shown in Figure 3.16 and 3.17, for the correlations between $\mathcal{R}$ and the 6 properties with $P_0 < 0.003$ in Table 3.14. The Spearman's rank correlation coefficients from our simulations are similar to the observed ones; the differences in peaks of r_s between the models and the observation

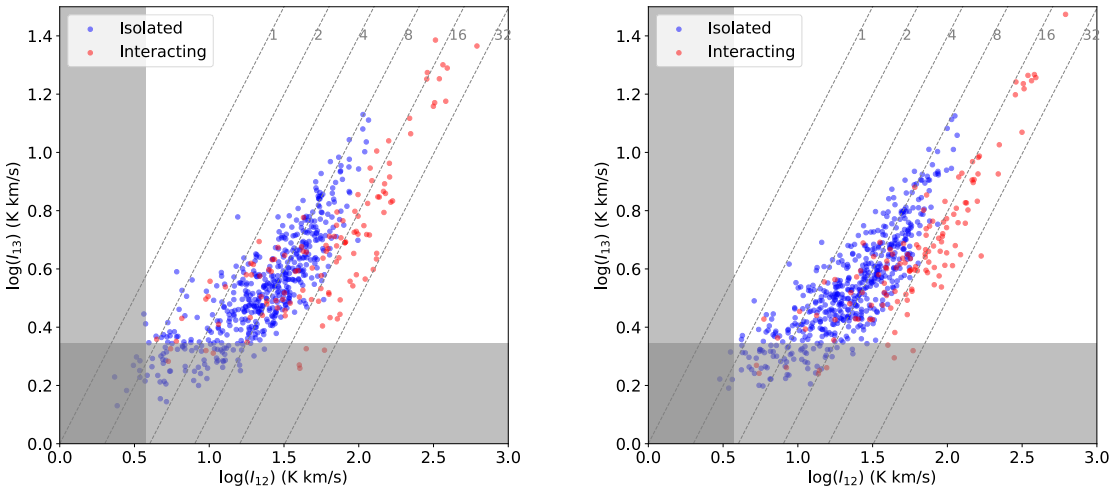

Figure 3.15. I_{13} as a function of I_{13} in the the constant scatter model (left panel) and in the cloudlet model (right panel). The blue dots and line represent the resolved $\mathcal{R}$ and the constant $\mathcal{R}$ used for the models for normal galaxies; the red dots and line are those for the interacting galaxies. The toy models based I_{12} reproduce similar characteristics of I_{13} to the observation. The blue dots show the I_{13} detections with S/N > 3 in the isolated galaxies, while the red ones are the I_{12} detections for the interacting galaxies. The detection limits of ^{13}CO and ^{12}CO are shown as the upper and right boundaries of the gray shaded regions respectively. Constant $\mathcal{R}$ values of [1,2,4,8,16,32] are shown as gray dashed lines.

are within 0.1. Although the modeled P_0 value distributions are not exactly the same as the observed distributions, the P_0 values from the model are mostly well below the threshold of $P_0 = 0.003$, which means the modeled correlations are significant above 3σ.

In our simulations, the modeled $\mathcal{R}$ values are derived entirely from I_{12} and its measurement uncertainty; no correlations between $\mathcal{R}$ and the other local properties are assumed. The apparent trends of $\mathcal{R}$ as functions I_{12}, I_{13}, stellar mass, moment 2, stellar surface density, stellar metallicity and SFR surface density, and dust attenuation can be reproduced by the models above 3σ significance. Therefore, the correlations are likely due to the sensitivity bias by only selecting resolved I_{13} above the detection threshold at the low I_{12} end. The sensitivity does have a strong effect on the correlations between $\mathcal{R}$ and the local properties in our sample.

3.3.5.3 Resolved $\mathcal{R}$ with bright I_{12} in isolated galaxies

Both $\mathcal{R}$ and the detection fraction of I_{13} relative to I_{12} increases with I_{12} (Figure 3.18), implying the cells with weaker I_{12} are more likely affected by the sensitivity bias. We define a completeness limit of $I_{12}{}^{\rm comp}$ for the isolated galaxies; above this limit, 75 percent of the cells with I_{12} detected are also detected in I_{13}. In our sample, $I_{12}{}^{\rm comp} = 29$ K km/s. We show this limit as the upper bound

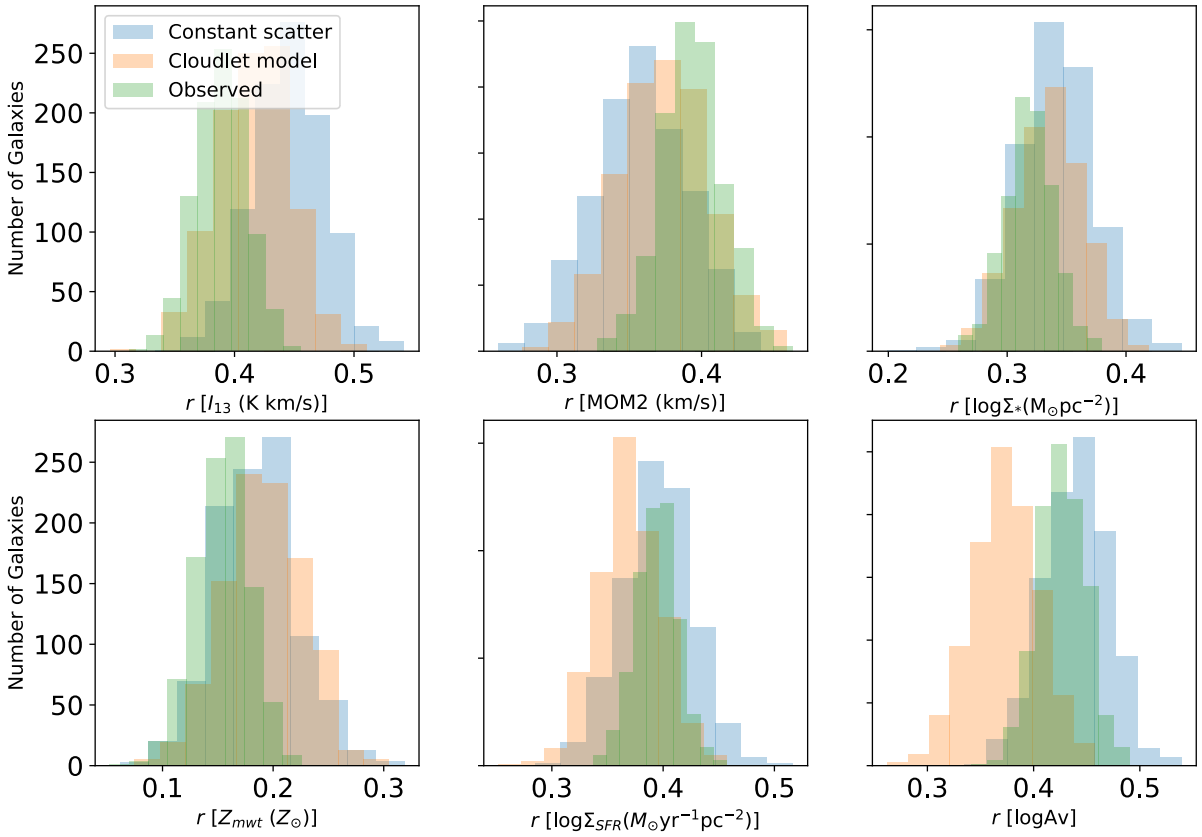

Figure 3.16. Distribution of Spearman's rank correlation coefficients r_s between $\mathcal{R}$ and local properties from the toy models and the observation. The blue bars show the distribution of r_s from the 1000 simulations using the constant scatter model, and the orange bars show the results from the cloudlet model. The green histogram shows the distribution of r_s when the measurement uncertainty of $\mathcal{R}$ are taken into account. Both models reproduce the observed correlations with $r_s > 0$.

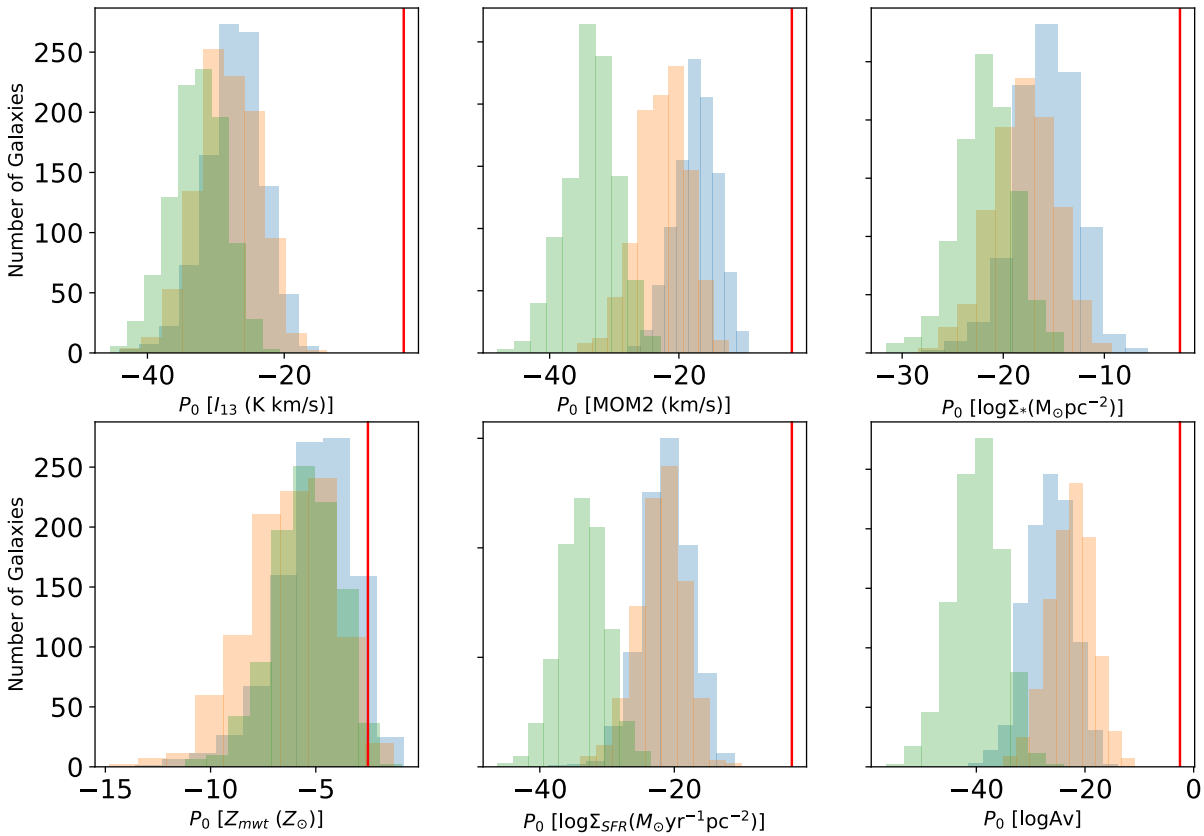

Figure 3.17. Distribution of logarithm of probability of the null hypothesis of no correlation between $\mathcal{R}$ and local properties from the toy models and the observation. The blue bars show the distribution of P_0 from the 1000 simulations using the constant scatter model, and the orange bars show the results from the cloudlet model. The green histogram shows the distribution of $\log P_0$ when the measurement uncertainty of $\mathcal{R}$ are taken into account. The red lines show $P_0 = 0.003$ corresponding to the significance level of 3σ. The P_0 values from the models are well below $P_0 = 0.003$, implying that the significant correlations observed can be attributed to the effect of sensitivity bias.

s

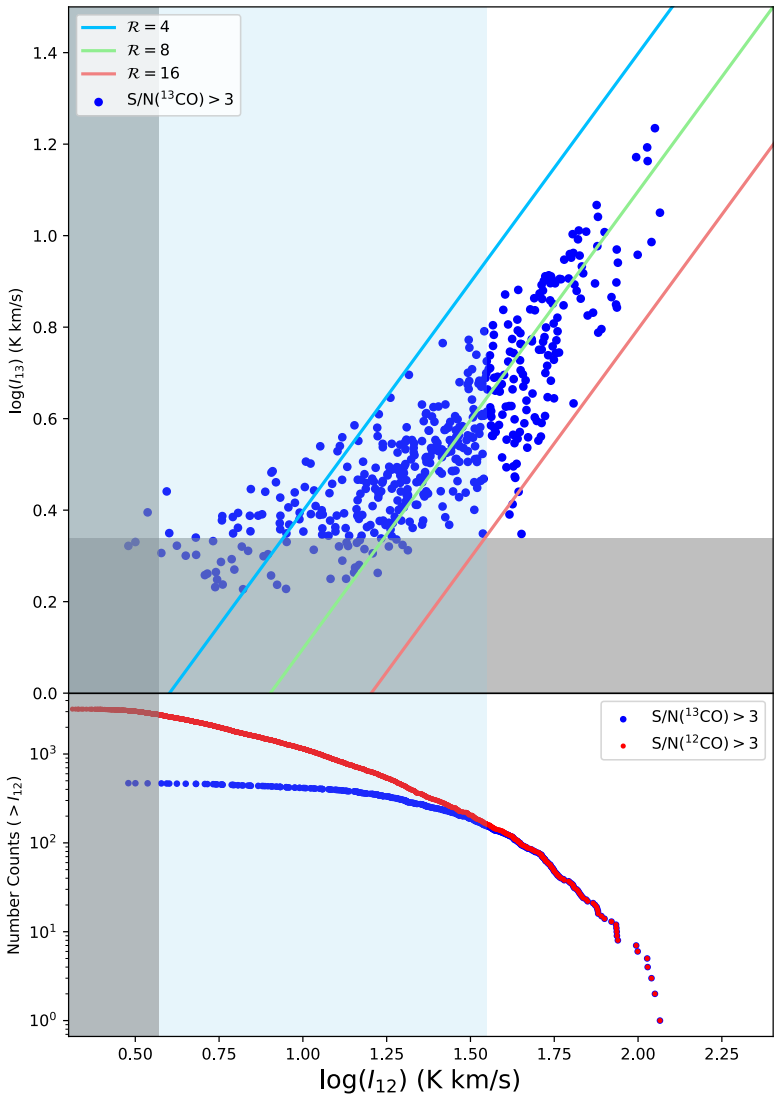

Figure 3.18. ^{13}CO intensity as a function of ^{12}CO intensities for non-interacting galaxies in the EDGE ^{13}CO sample. The blue dots show the ^{13}CO detections, while the red symbols represent the regions where ^{13}CO are below the detection limits. The detection limits of ^{13}CO and ^{12}CO are shown as the upper and right boundaries of the gray shaded regions respectively. In the lower panel, total numbers of I_{12} and I_{13} detections above a given I_{12} are shown.

of the light blue shaded region in Figure 3.18. The blue shaded region below the completeness limit is more biased by the sensitivity and the correlations are likely affected by this bias.

To reduce the sensitivity bias effect due to the incomplete detection of I_{13}, we use all the cells with I_{12} above the completeness limit of $I_{12}{}^{\rm comp}$ in isolated galaxies for the investigation of resolved correlations. Approximately 200 cells from 14 isolated galaxies are selected. We calculate the Spearman's correlation coefficient r_s and the probability of null hypothesis P_0 for each of

the correlations. Figure 3.19 summarizes the bivariate distribution of resolved $\mathcal{R}$ and the local properties on kpc scales for the isolated galaxies with bright I_{12} above the completeness limit.

There is no dependence on I_{12} for cells selected with bright I_{12}. However, a strong correlation between $\mathcal{R}$ and I_{13} is present. Moreover, the resolved $\mathcal{R}$ is weakly correlated with stellar mass and gas metallicity above 3σ significance ($P_0 < 0.003$). No significant trends of $\mathcal{R}$ with moment 2, stellar metallicity, stellar age, dust extinction, or SFR surface density are found in our sample. These results are much different from the correlation coefficients using all the I_{13} detections in the isolated galaxies shown in columns 6 – 9 of Table 3.14.

By selecting cells with bright I_{12}, $\mathcal{R}$ for smaller I_{13} will be biased toward higher values; the correlation we find between $\mathcal{R}$ and I_{13} is likely due to this selection effect. We also run simulations from the two simple models to examine the impact of this selection bias. Distributions of the r and P_0 values of the three significant correlations ($\mathcal{R}$ vs. I_{13}, stellar mass, and gas metallicity) are shown in Figure 3.20 and 3.21. The Spearman's rank correlation coefficients from the models show smaller absolute values compare to the observed r. Both the models show decreasing $\mathcal{R}$ with I_{13} ($r < 0$); the dependence of $\mathcal{R}$ on I_{13} in the models is weaker than that in the observed sample. However, the correlations between $\mathcal{R}$ and I_{13} in the models can still reach the significance level of 3σ. Therefore, it is possible that this trend observed is partly induced by the selection bias in the resolved cell sample used for the correlation test.

On the other hand, for stellar mass surface density and metallicity, distributions of r from the models is symmetric around 0 and in the range between -0.2 and 0.2. P_0 values resulting from the model are generally distributed above 0.01, larger than the 3σ threshold of $P_0 = 0.003$ and the P_0 values measured from the observation. These two correlations for cells with bright I_{12} cannot be reproduced from the toy models with high significance. With the hypothesis that there is no correlation between $\mathcal{R}$ and stellar surface or gas metallicity, the selection bias effects of the sample alone cannot explain the trend we observe.

3.3.6 Radial profiles of $\mathcal{R}$

To improve the S/N compared to that can be achieved in individual cells, we generate the radial profiles of $\mathcal{R}$ using a spectral stacking method. The resolved $\mathcal{R}$ are usually detected with bright

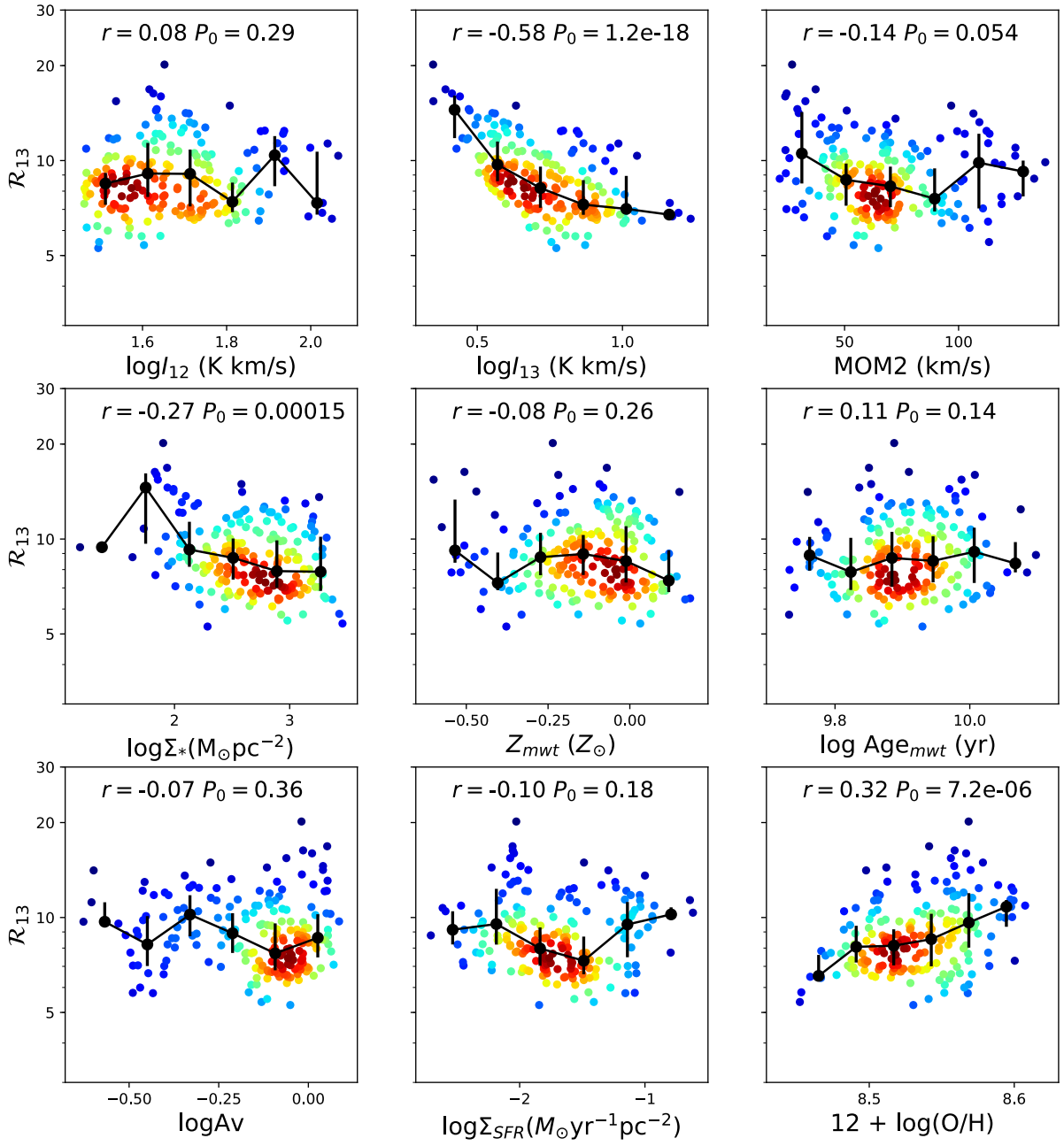

Figure 3.19. Resolved $\mathcal{R}$ as functions of resolved properties derived from the EDGE-CALIFA survey for cells with I_{12}>$I_{12}{}^{\rm comp}$. The panels from the top-left to the bottom-right are (1) ^{12}CO intensity; (2) ^{13}CO intensity; (3) MOM2 of ^{12}CO intensity; (4) stellar mass derived by PIPE3D; (5) Light weighted stellar metallicity; (6) Light weighted stellar age; (7) SFR derived from extinction corrected Hα flux; (8) Gas metallcity 12+log(O/H) derived from O3N2; (9) Dust extinction. See detailed descriptions of the quantities in Section (Data description). Each filled circle represent an individual cell, and the black open circles show the median $\mathcal{R}$. On the top of each panel, we show the Spearman correlation coefficient r and the probability of null hypothesis P_0 for each of the correlation.

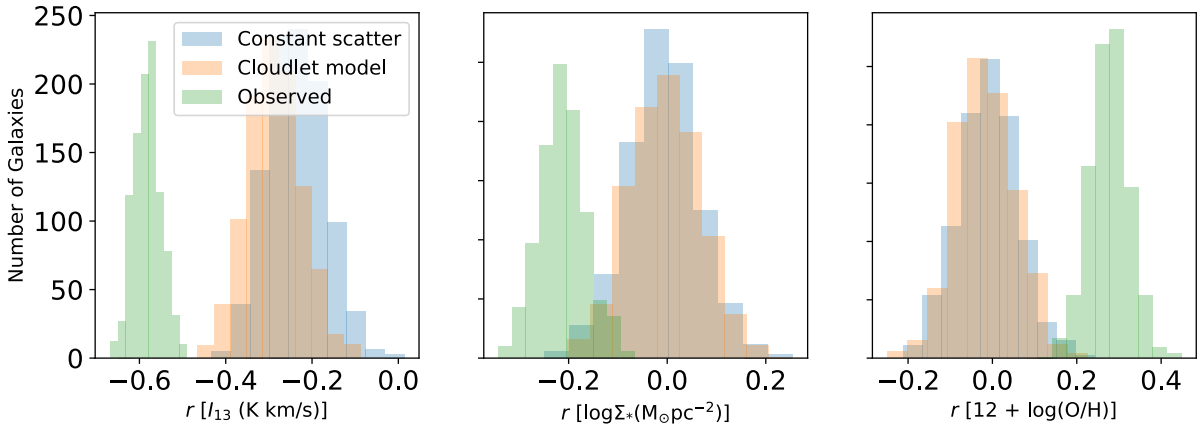

Figure 3.20. Distribution of Spearman's rank correlation coefficients r between $\mathcal{R}$ and local properties from the toy models and the observation for cells selected by $I_{12}{>}I_{12}{}^{\rm comp}$. The blue bars show the distribution of r from the 1000 simulations using the constant scatter model, and the orange bars show the results from the cloudlet model. The green histogram shows the distribution of r when the measurement uncertainty of $\mathcal{R}$ are taken into account. Both of models show smaller absolute values of r compare to the observation.

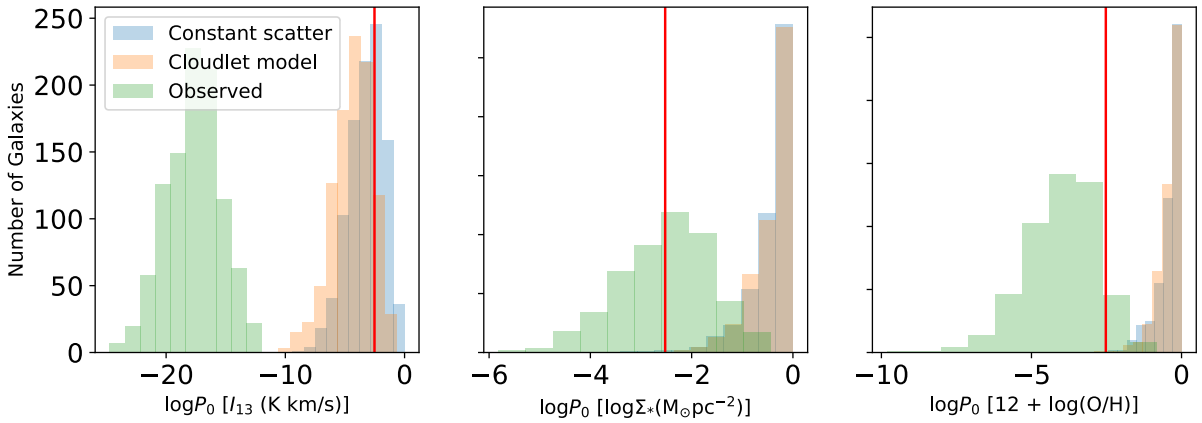

Figure 3.21. Distribution of logarithm of probability of the null hypothesis of no correlation between $\mathcal{R}$ and local properties from the toy models and the observation for cells selected by $I_{12}{>}I_{12}{}^{\rm comp}$. The blue bars show the distribution of P_0 from the 1000 simulations using the constant scatter model, and the orange bars show the results from the cloudlet model. The green histogram shows the distribution of $\log P_0$ when the measurement uncertainty of $\mathcal{R}$ are taken into account. The reds line show $P_0 = 0.003$ corresponding to the significance level of 3σ. The P_0 values from the models are well below $P_0 = 0.003$, implying that the significance correlations observed can be attributed to the effect of sensitivity bias.

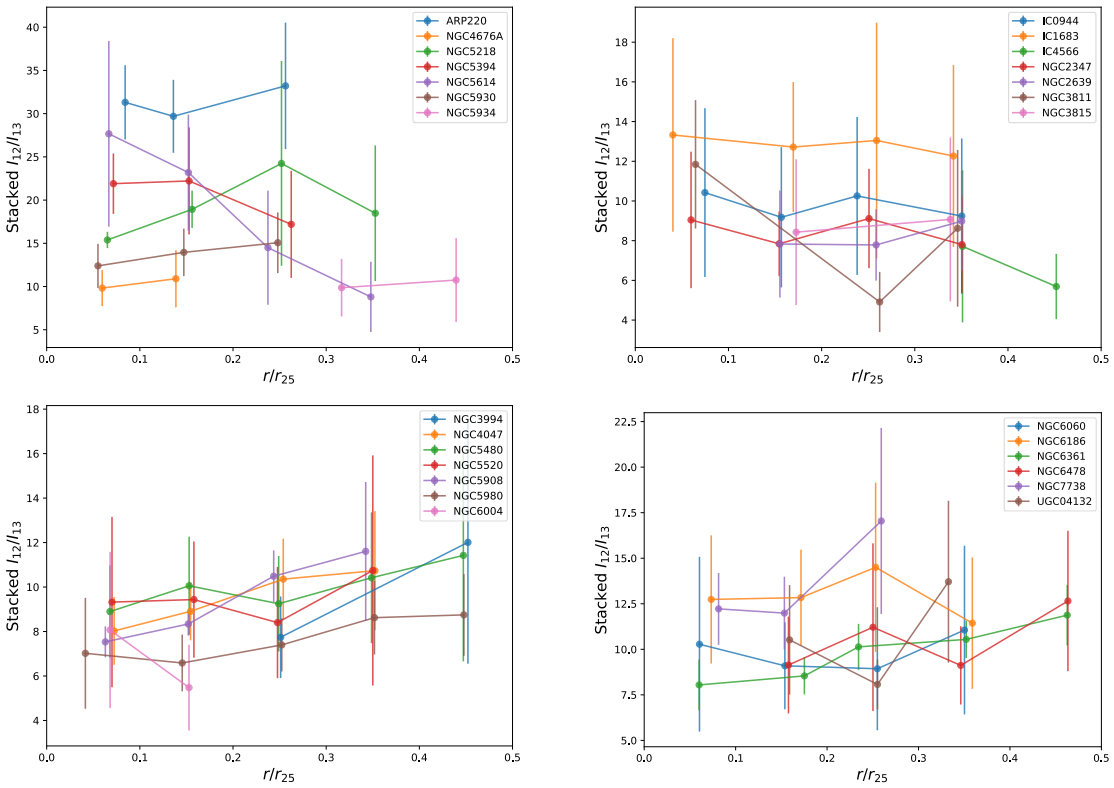

Figure 3.22. Radial averaged profiles of $\mathcal{R}$. The galactocentric radius for each galaxy is normalized to its R_{25}. Spectra of ^{13}CO and ^{12}CO are shifted and stacked at each normalized radii bin are used to derive the averaged $\mathcal{R}$. The interacting galaxies are shown in the panel and the rest of panels show the other isolated galaxies.

I_{12} in the central regions of the galaxies. As I_{12} decreases with radius, lower S/N of I_{13} prevents the estimation of resolved $\mathcal{R}$ at larger radii. To obtain radial profiles of $\mathcal{R}$, we stack the spectra of I_{12} and I_{13} in normalized radial bins with a step of $0.1R_{25}$. At a given radius, the ^{13}CO and ^{12}CO spectra for all the cells with I_{12} detected are selected. For each pair of ^{12}CO and ^{13}CO spectra of a cell, the ^{12}CO dilated mask is used to choose a velocity window for both spectra. Both of the masked spectra are shifted to a common velocity using the the I_{12}-weighted mean velocity (moment 1). After all the spectra in the radial bin are shifted, ^{13}CO and ^{12}CO are stacked and their uncertainties are calculated by error propagation. If the peak S/N of the stacked ^{13}CO is above 2, the integrated fluxes from the stacked spectra are used to derive the radial average $\mathcal{R}$.

Figure 3.22 shows the stacked $\mathcal{R}$ profiles we obtain for the sample galaxies. Using the stacked spectra, we are able to obtain the radial profiles of $\mathcal{R}$ up to 0.4 r/R_{25} (corresponding to a radius of typically $\sim$ 5 kpc) for most of galaxies. We group the 28 galaxies into three categories based on the slopes from the linear regression of the radial profiles of $\mathcal{R}$.

1. **$\mathcal{R}$ profile shows increasing trend**: 3 interacting galaxies (ARP 220, NGC 5218, and NGC 5930) and 11 isolated galaxies (NGC 3994, NGC 4047, NGC 5480, NGC 5520, NGC 5908, NGC 5980, NGC 6060, NGC 6361, NGC 6478, NGC 7738, and UGC 04132).

2. **No obvious general radial trend**: NGC 4676A (interacting), IC 0944, IC 1683, NGC 2347, NGC 2639, NGC 3815, NGC 5520, NGC 6060, and NGC 6186. In these galaxies, the variations of $\mathcal{R}$ in radius are within the measurement uncertainty of the stacked $\mathcal{R}$.

3. **Decreasing $\mathcal{R}$ with radius**: NGC 5394, NGC 5614, IC 4566, NGC 3811, and NGC 6004. The first two are interacting galaxies, and the others are isolated galaxies. NGC 5614 has a ring; the remaining four galaxies are barred galaxies.

Half of the galaxies with stacked $\mathcal{R}$ profiles show slightly increasing trend. The general increasing trend we find in this study is qualitatively consistent with our previous work of 11 galaxies from the CARMA STING survey (Cao et al., 2017) and a recent study of ^{13}CO of 9 nearby galaxies on kpc scales by Cormier et al. (2018). Increasing $\mathcal{R}$ with galactocentric radius are also reported in the Milky Way (Roman-Duval et al., 2016) and in some nearby galaxies (Meier & Turner, 2004; Rosolowsky & Blitz, 2005). Our results are in contrast to an earlier single dish study by Paglione et al. (2001) that found $\mathcal{R}$ decrease away from the galaxy center for about half of their sample galaxies.

$\mathcal{R}$ profiles present a flat or increasing trend for the majority of the sample galaxies. Only 5 out the 28 galaxies in our sample show a decreasing trend. All of these 5 galaxies have a bar, a ring, or are in interacting systems. In these galaxies, the higher $\mathcal{R}$ in the central regions may be due to gas flows caused by bars, rings, or interactions.

The general trends of our sample can be more obviously seen in Figure 3.23. We obtain the stacked $\mathcal{R}$ over two raidal ranges, inside and outside $0.25R_{25}$. $\mathcal{R}$ in the disks are slightly higher than the central $\mathcal{R}$ for majority of the sample galaxies. The differences of $\mathcal{R}$ in the center and disk in the 30 galaxies are within a factor of 2. There is no general radial trend for the interacting galaxies (the top left panel 3.22 of Figure and the bottom left panel of Figure 3.23). However, decreasing radial trend of $\mathcal{R}$ are often found in galaxies where the gas is disturbed by bar, ring, or interacting process (Figure 3.23).

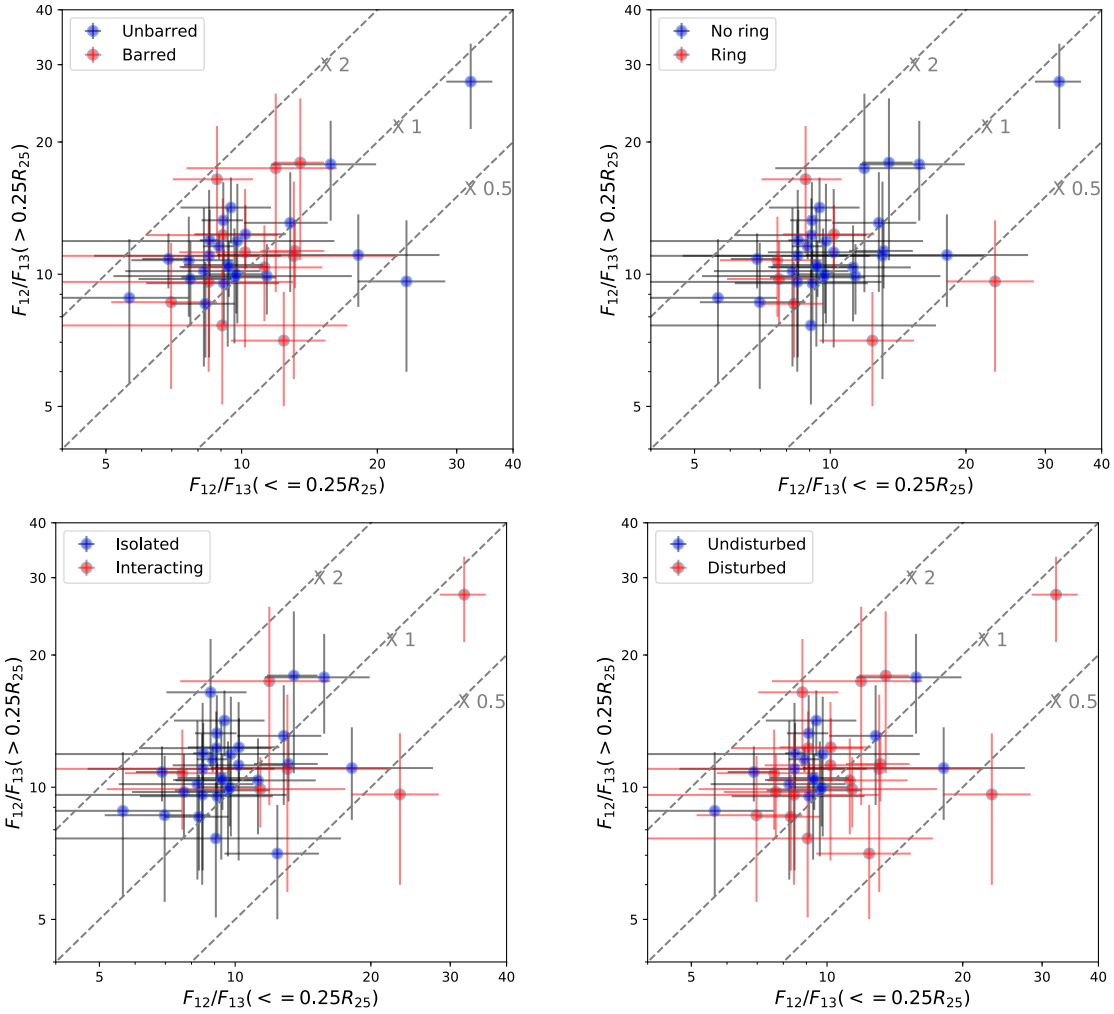

Figure 3.23. Comparison of stacked $\mathcal{R}$ inside and outside $0.25R_{25}$. The first three panels compare barred and unbarred galaxies, galaxies with and without ring, and interacting galaxies and isolated galaxies. In the last panel, galaxies with a ring, a bar, or in interacting are labeled as "disturbed" galaxies, whereas the rest are labeled as "undisturbed".

3.4 Discussion

3.4.1 Possible causes of $\mathcal{R}$ variations in isolated galaxies

Variations of $\mathcal{R}$ are caused by changes in fractional chemical abundance [^{12}CO/^{13}CO], or by the differences in physical conditions of molecular gas such as density, temperature, and line width that determines the gas opacity. Using a sample with a relatively wide variety of galaxies in this study, we find no significant correlation above 3σ between $\mathcal{R}$ and global properties derived on galactic scales except F_{60}/F_{100}. The general increasing F_{12}/F_{13} with F_{60}/F_{100} agrees with the results of some previous studies (e.g. Aalto et al., 1995; Crocker et al., 2012). We find the correlation is significant even when the highest values from interacting galaxies are removed. Since F_{60}/F_{100} measures the dust temperature approximately, our results show that $\mathcal{R}$ increases with dust temperature on galactic scales. One possible cause is that $\mathcal{R}$ is elevated when the optical depth of ^{12}CO is reduced with higher temperature. However, the investigations on resolved $\mathcal{R}$ measurements in this study and the two recent studies by Cao et al. (2017) and Cormier et al. (2018) suggest that $\mathcal{R}$ is not very sensitive to temperature variations on kpc scales. Because the difference in beam filling factors of ^{13}CO and ^{12}CO on large scales may also play an important role in determining $\mathcal{R}$ in the unresolved, single-dish studies, it is difficult to argue that it is dust temperature causes the changes in global $\mathcal{R}$. The dependencies of global $\mathcal{R}$ and F_{12}/F_{13} on dust temperature can also be explained by changes in the abundance [^{12}CO/^{13}CO]: when the temperature of a galaxy is low, global $\mathcal{R}$ and F_{12}/F_{13} of the galaxy tend to be lower due to the chemical fractionation towards ^{13}CO and thus low [^{12}CO/^{13}CO]. On the other hand, for a larger sample of normal spiral galaxies in a single dish survey with no missing flux, Vila-Vilaro et al. (2015) report a lack of correlation between $\mathcal{R}$ and F_{60}/F_{100}. It is possible the correlation between F_{12}/F_{13} and F_{60}/F_{100} may also be due to the bias of the EDGE ^{13}CO sample toward lower end for galaxies with lower F_{12} and presumably lower F_{60}/F_{100}.

The azimuthally averaged $\mathcal{R}$ slightly increases with radius in half of the sample galaxies. A higher fraction of less dense gas at larger radii could explain the average increasing trend: the decreasing average gas density away from the galaxy center reduces the gas opacity and leads to positive gradient trend in $\mathcal{R}$. This scenario is also consistent with of our results from the correlation

test in cells with bright I_{12}, from which the resolved $\mathcal{R}$ slightly decreases with stellar mass surface density. Away from the galaxy center, stellar mass surface density decreases, and thus the gas is less gravitationally confined to the midplane. $\mathcal{R}$ would then increase when the average density is reduced. Alternatively, increasing fractional abundance of $[^{12}C/^{13}C]$ with radius such as measured in the Milky Way by Milam et al. (2005) due to the chemical evolution could also explain the radial trend. However, there is no direct measurement of $[^{12}C/^{13}C]$ as a function of radius in other galaxies. Moreover, we did not see a significant correlation between $\mathcal{R}$ and stellar age; the impact of chemical evolution on $\mathcal{R}$ is not well understood yet.

The correlation between $\mathcal{R}$ and ionized gas metallicity we find for the cells with bright I_{12} seems to contradict with the average increasing radial trend of $\mathcal{R}$; the metallicity generally decreases with radius, and anti-correlation between $\mathcal{R}$ and metallicity is implied from the increased $\mathcal{R}$ with radii. However, the correlation we find is limited to central regions with relatively bright I_{12}. A two component model can explain the increasing $\mathcal{R}$ with metallicity. ^{13}CO emission is originated from the dense, inner layer, while the ^{12}CO is from a less dense, outer layer. For cells with lower metallicity, the outer layer of ^{12}CO is less shielded and I_{12} is reduced, but in the deeper layer I_{13} is less affected, therefore $\mathcal{R}$ will increase with metallicity. This scenario requires a large amount of gas in a beam, which is likely the case in our sample cells where both I_{13} and I_{12} are large enough.

3.4.2 Elevated $\mathcal{R}$ in interacting galaxies

Galaxy interactions are important processes in the evolution of galaxies. During the integrating process, the gas is driven toward the inner few kiloparsec of the galaxy and triggers active star formation. Both the stars and interstellar medium are strongly perturbed during the process. The physical conditions in molecular gas during the merging process are expected to be different from the gas in normal, isolated galaxies.

It has been reported by several single dish surveys that the global $\mathcal{R}$ in bright mergers is higher than $\mathcal{R}$ in normal spiral galaxies (e.g. Aalto et al., 1991; Casoli et al., 1991, 1992). Observed resolved $\mathcal{R}$ of merging galaxies on smaller scales from different individual studies also tend to be higher than the typical $\mathcal{R}$ observed in normal galaxies (e.g. Young & Scoville, 1984; Taniguchi & Ohyama, 1998; Henkel et al., 2014; Aalto et al., 2010). In our previous systematic study of resolved

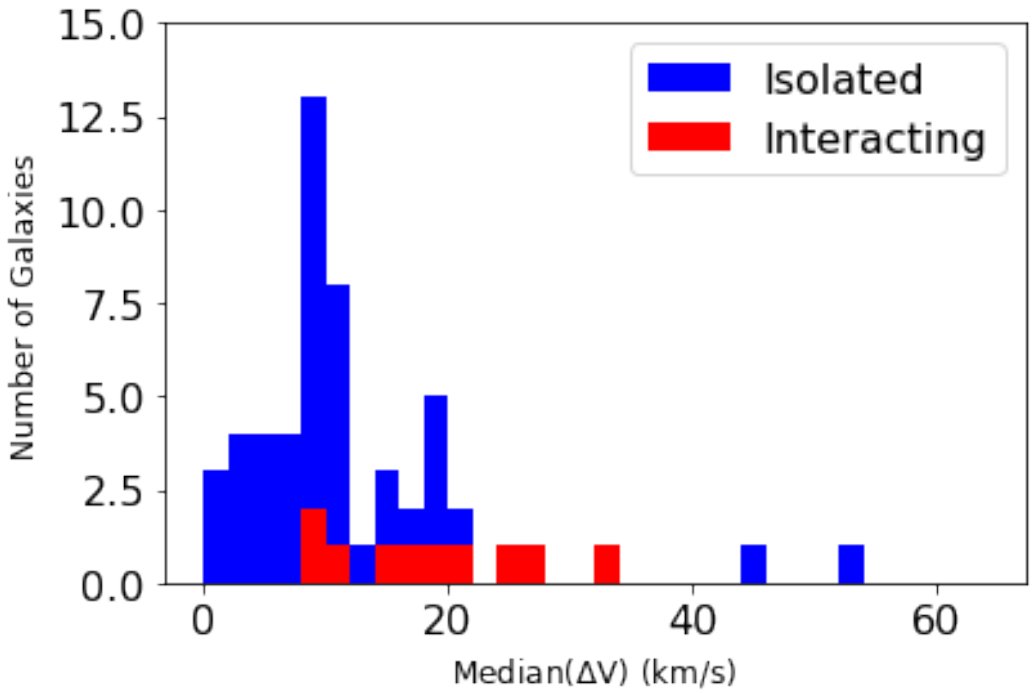

Figure 3.24. Distribution of median velocity dispersion resulting from fitting a model to the ^{13}CO rotation curve by Bbarolo of the galaxy. The typical velocity dispersion in interacting galaxies is higher than that in the isolated galaxies.

$\mathcal{R}$ from the STING survey, the highest $\mathcal{R}$ is found in the interacting galaxy NGC 5713 (Cao et al., 2017). In this study with the EDGE survey, we find that both the line ratio averaged on galactic scales and the resolved $\mathcal{R}$ on kpc scales in interacting galaxies are higher than in normal galaxies, suggesting that the gas conditions are systematically different in the interacting galaxies.

Three scenarios had been proposed to explain the systematically higher line ratios in merging systems:

1. A large amount of gas with higher $\mathcal{R}$ is funneled into the inner galaxy from the outskirts by gas inflow during the interacting process. This scenario is plausible as the radial profiles of $\mathcal{R}$ in our sample galaxies show generally increasing trends. The inflow of gas from outer regions of the galaxies that are more diffuse and/or less processed with low ^{13}C can elevate $\mathcal{R}$ in the interacting galaxies. Moreover, the molecular gas distribution in the interacting galaxies also tends to be more concentrated than the others. This result might also signify that the gas are funneled into the centers in the interacting galaxies. However, the gas must remain diffuse and unprocessed.

2. The gas is much warmer and/or the line width is larger so the opacity is reduced. The bright mergers also have higher IR color F_{60}/F_{100} which measures the dust temperature. The gas in these galaxies is likely heated by the active star formation triggered by the interaction. However, $\mathcal{R}$ in interacting galaxies with low IR color is also higher than $\mathcal{R}$ in isolated galaxies with similar IR color, and this cannot be attributed to the differences in dust temperature. Similar to F_{60}/F_{100}, although the highest $\mathcal{R}$ values are found in interacting galaxies with largest values of moment 2, $\mathcal{R}$ in interacting galaxies at a given moment 2 also appears to be higher than their counterparts from the isolated galaxies. We bear in mind that the velocity dispersion of each cell measured from moment 2 are not corrected for the effects of beam smearing. In Figure 3.24, we compare the typical (median) values of the velocity dispersion resulting from simultaneous modeling of the rotation and dispersion using ^{3D}BAROLO (Di Teodoro & Fraternali, 2015). The velocity dispersions in the interacting galaxies tend to be higher; elevated $\mathcal{R}$ in interacting galaxies might also be explained by the broadened line width in them.

3. The isotope abundance $[^{12}C/^{13}C]$ is elevated in the interacting systems due to the active star formation. While ^{12}C is produced by all stars through various mass loss mechanism (e.g. SNeI, SNeII, AGB), ^{13}C is ejected into the ISM in the AGB phase of low mass stars mainly via CNO processing of ^{12}C. The recent massive star formation triggered by the merging status can boost the ^{12}C abundance for the interacting galaxies. Abnormally high $\mathcal{R}$ values in (U)LIRGs and high redshift galaxies are found contributing to the elevated $[^{12}C/^{13}C]$ by multi-line analysis (Sliwa et al., 2017; Danielson et al., 2013). Chemical evolution models also suggest that $[^{12}C/^{13}C]$ is boosted in mergers (Romano et al., 2017). We cannot exclude this possibility, although the elevated $\mathcal{R}$ cannot be directly attributed to their differences in stellar age from the isolated galaxies in our sample. High levels of ^{12}CO and ^{13}CO lines, or $C^{18}O(1-0)$ might help. A more direct measurement of $[^{12}C/^{13}C]$ from CN lines such as performed by Henkel et al. (2014) would largely benefit this discussion.

3.4.3 Caveats of this study

One caveat of the this study is that we do not have single dish observations for the calculations of the line ratios. There could be ^{12}CO emissions that are missed in our interferometric observations: extended emission might be filtered out by the lack of short spacings, and weak I_{12} on smaller scales are missed due to the relatively low sensitivity of interferometers compared to single dishes. The effect of spatial filtering on the intensity and $\mathcal{R}$ measurement of each galaxy is unclear, but are more likely to affect ^{12}CO than ^{13}CO. Observing the sample galaxies in single dish telescopes such as IRAM and GBT will improve this study.

Another caveat of the investigation on resolved $\mathcal{R}$ is the lack of knowledge on I_{13} and $\mathcal{R}$ for the outer regions with weak I_{12}. The sample of $\mathcal{R}$ is largely biased to lower values at large radii beyond $0.2r/R_{25}$ where both I_{12} and I_{13} are weak. The variations in stellar and ionized gas properties are also more obvious in these regions. Limiting our correlation tests to I_{12} bright regions that are not severely affected by the sensitivity results in small numbers of data points with very narrow ranges of resolved properties in each galaxy. We combine the cells from different galaxies for the investigation of resolved $\mathcal{R}$. In this approach, each cell is treated equally. Some galaxies have more cells included than the others, and these galaxies might have stronger impacts on the results of the correlation tests. Some of the correlations are contributed largely by the two brightest galaxies, NGC 5908 and NGC 6361. Resolved $\mathcal{R}$ observations with better sensitivities are needed for a better understanding the relation of molecular gas to stellar and ionized gas properties.

3.5 Conclusions

We present ^{13}CO observations for the EDGE-CALIFA survey, which is a mapping survey of 126 nearby galaxies at a typical spatial resolution of 1.5 kpc. We have measured total ^{13}CO flux for 56 galaxies and resolve ^{13}CO intensity on kpc scales for 42 galaxies from the EDGE-CALIFA survey. Combining our ^{13}CO and ^{12}CO observations with optical spectroscopy IFU data from the CALIFA survey, we perform a systematic study of spatially resolved ^{13}CO and $\mathcal{R}$ on kpc scales in relation to the properties of stellar and ionized gas for a wide variety of galaxies. Our main conclusions are as follows:

1. We measure the global line ratio of a galaxy by the flux ratio F_{12}/F_{13} and the I_{13}-weighted mean resolved ratio $\langle\mathcal{R}\rangle$). Both the global line ratios increase with the IRAS IR color F_{60}/F_{100} in the sample galaxies with detectable F_{13} or I_{13}. For the normal, isolated galaxies, the global ratios are insensitive to other galactic scale properties such as morphology type, total stellar mass, galaxy size, mean stellar age, and etc.

2. We find that both the flux ratio F_{12}/F_{13} and the weighted mean $\langle\mathcal{R}\rangle$ are higher in the interacting galaxies than in the isolated galaxies. Moreover, the resolved $\mathcal{R}$ values measured on kpc scales in interacting galaxies are also systematically higher than in the isolated galaxies. The gas inflow, higher velocity dispersion, and the elevated [^{12}C/^{13}C] in the interacting process could be possible causes of the systematic higher $\mathcal{R}$ in the interacting galaxies.

3. We combine all the resolved $\mathcal{R}$ measurements from the 42 galaxies in the EDGE ^{13}CO sample to study the relations between $\mathcal{R}$ and other properties on the same scales. However, low signal-to-noise of I_{13} imposes selection bias to the investigation on the resolved correlations. We study effects of sensitivity bias on $\mathcal{R}$ and the resolved correlations through Monte Carlo simulations based on two simple models. The models can reproduce the correlation between $\mathcal{R}$ and I_{12}, moment 2, stellar mass surface density, stellar metallicity, SFR surface density, and dust extinction similar to the observations, therefore these apparent correlations could possibly explained by the sensitivity bias of the resolved $\mathcal{R}$ used for the investigation.

4. We limit the resolve-to-resolve correlation investigations to a sub-sample of cells that have bright I_{12} and is thus less affected by the sensitivity bias. We find that in the isolated galaxies, resolved $\mathcal{R}$ decreases with I_{13}, stellar mass surface density, and increases with ionized gas metallicity. We run the simulations and conclude that these three correlations cannot be entirely attributed to the selection effects of the sub-sample. On the other hand, there is no significant correlation between resolved $\mathcal{R}$ and I_{12}, moment 2, stellar metallicity, stellar age, dust extinction, or SFR surface density for the sub-sample with bright I_{12}. Our results suggest that the underlying density and/or chemical abundance play more important roles than other local stellar or ISM properties in determining resolved $\mathcal{R}$ values.

5. We present annulus-averaged $\mathcal{R}$ radial profiles for our sample up to a galactocentric radius

of $\sim$5 kpc, taking into account the ^{13}CO non-detections by spectra stacking. We find that roughly half of galaxies show increased $\mathcal{R}$ beyond $0.25R_{25}$, suggesting more optically thin gas or lower ^{13}C abundance in the disks relative to the centers in general. Decreasing trends are mostly seen in interacting galaxies or barred galaxies.

Chapter 4

Multi-line Studies of NGC 4254 and NGC 5713

4.1 Introduction

The conditions for star formation are related to the physical conditions of the molecular gas, such as temperature, density, velocity dispersion and chemical composition. In particular, temperature and velocity dispersion contribute support against gravity, whereas the distribution of densities determines which parts of the medium are able to become gravitationally unstable. Star formation feedback in turn affects the molecular gas properties, making it essential to study molecular cloud properties in various local environments to disentangle causes and effects.

Physical conditions of molecular gas on a galactic scale have been studied by comparing the intensity of ^{12}CO($J = 1 \rightarrow 0$) with multiple transitions such as ^{13}CO($J = 1 \rightarrow 0$) and ^{12}CO($J = 2 \rightarrow 1$). Such comparisons could reveal detailed variations of the gas conditions. The ^{12}CO($J = 1 \rightarrow 0$)/ ^{13}CO($J = 1 \rightarrow 0$) intensity ratio $\mathcal{R}$ is sensitive to variations in CO opacity due to the changes of physical properties. Opacity variations, however, can arise for many reasons, from simple geometry (e.g., an edge-on perspective leading to high column densities) to changes in gas properties (e.g., colder, denser, or more quiescent gas absorbing more effectively). In addition, changes in isotope abundance can also affect $\mathcal{R}$. The additional line ratio ^{12}CO($J = 2 \rightarrow 1$)/ ^{12}CO($J = 1 \rightarrow 0$) (r_{21} hereafter) can be used to further constrain temperature, density, and line opacity. Combining two or more ratios thus provides the most useful constraints on physical conditions. Besides, unlike ^{13}CO emission which is mostly confined in the bright, central regions, ^{12}CO($J = 2 \rightarrow 1$) emission can also be detected in outer disk regions. The r_{21} value will give additional information for the less dense regions without detectable ^{13}CO emission.

The line ratio r_{21} has been used to study changes of physical conditions in the Milky Way and some nearby galaxies. In general, r_{21} greater than unity (very high ratio) indicates optically thin

gas. Under unity, high r_{21} (> 0.7) may be due to a steep density gradient or higher temperature of the molecular gas, and could be an indicator of massive star formation (Hasegawa, 1997). Low r_{21} (< 0.7) may occur in low density regions. When both ^{12}CO($J = 2 \rightarrow 1$) and ^{12}CO($J = 1 \rightarrow 0$) lines are optically thick, the ratio could also help us derive the excitation temperature, and determine whether the gas is in local thermal equilibrium (LTE) or not. Radial variations of r_{21} have been detected in the Galaxy, and high ratios appeared in the spiral arms (Sakamoto et al., 1997b). Spatial variations of ratio are also detected in nearby galaxies (e.g. Koda et al., 2012; Crosthwaite et al., 2002; Crosthwaite & Turner, 2007). Higher r_{21} values are often attributed to warmer gas in the region.

Recently, we have obtained measurements of the $\mathcal{R}$ ratio across the disks of 11 spiral galaxies in the CARMA STING sample (Rahman et al., 2011, 2012; Wong et al., 2013; Cao et al., 2017). Previous single-dish measurements have found that this ratio varies from values of ~ 6 in Galactic molecular clouds to values of $\sim 10 - 15$ for starburst nuclei (Polk et al., 1988; Aalto et al., 1995). Consistent with these findings, Paglione et al. (2001) found indications of a weak gradient in the ratio from $\sim$ 12 near the centers of spiral galaxies to $\sim$ 10 outside 2 kpc, possibly due to a modest increase in temperature near the nucleus leading to a decrease in optical depth. Strong local variations in $\mathcal{R}$ have been measured with interferometers, particularly in barred galaxies, for example, NGC 7479 in Hüttemeister et al. (2000) and IC 342 in Hirota et al. (2010). These variations have been interpreted as due to varying ratios of diffuse to dense gas. However, both of these $\mathcal{R}$ studies do not have well constrained physical conditions; additional line ratios such r_{21} are needed to break the degeneracy of temperature and density in $\mathcal{R}$.

We select NGC 4254 and NGC 5713 for this study as both are bright in ^{12}CO($J = 1 \rightarrow 0$) but they exhibit very different star formation activity and $\mathcal{R}$. NGC 4254 is located at a distance of 17 Mpc in the Virgo cluster. The asymmetric distribution of gas in it suggests that the galaxy could have gone through a minor merger. Its star formation across the disk is normal (Koopmann & Kenney, 2004). NGC 5713 is at a distance of 24 Mpc. The gas in NGC 5713 is also disturbed, possibly by interactions with a nearby spiral galaxy. Compared to NGC 4254, it has relatively active star formation. Besides well measured resolved $\mathcal{R}$ in the central regions, averaged $\mathcal{R}$ values at galactocentric radius beyond $0.2R_{25}$ are available for these two galaxies. Detailed molecular

gas conditions on kpc scales can be constrained from $\mathcal{R}$ and r_{21}, and their relations to local star formation activity and galactocentric radius can be investigated in the sample galaxies.

In this study, we present the ^{12}CO($J = 2 \rightarrow 1$) observations in NGC 4254 and NGC 5713. In Section 4.2, we describe the observations and data reduction. The ^{12}CO($J = 2 \rightarrow 1$) maps and the multi-line analysis are presented in Section 4.3. In Section 4.4, we summarize the current results and describe the future work of this study.

4.2 Observation

4.2.1 CARMA observation of ^{12}CO($J = 2 \rightarrow 1$)

Observations of ^{12}CO($J = 2 \rightarrow 1$) in this project were carried out in 2014 December by CARMA in the E array, with integration time of 24 hr per galaxy. We used a 21-point mosaic for NGC 4254 and a 17-point mosaic for NGC 5713. The correlators were tuned to ^{12}CO($J = 2 \rightarrow 1$) frequency at 230.538 GHz in the upper sideband. ^{12}CO($J = 2 \rightarrow 1$) was observed in 4 bands with bandwidth of 250 MHz, yielding a velocity coverage of $\sim$ 1300 km s^{-1}. The remaining spectral windows were used to measure the dust continuum. We used Uranus, Mars, Neptune, or MWC349 as the primary flux calibrators. The gain and bandpass calibrators are 3C279 for NGC 4254 and 1512-090 for NGC 5713. The visilibity data were calibrated in MIRIAD.

Imaging has been performed using tasks INVERT and MOSSDI in MIRIAD with natural weighting. The synthesized beam sizes are $5.4'' \times 4.73''$ and $7.2'' \times 4.5''$ for NGC 4254 and NGC 5713 respectively. The spectral resolution has been smoothed to 5 km s^{-1}. The cubes have been transformed to match the spatial and velocity frames of ^{12}CO($J = 1 \rightarrow 0$) and ^{13}CO($J = 1 \rightarrow 0$) observations from the CARMA STING survey.

4.2.2 Observations of ^{12}CO($J = 1 \rightarrow 0$) and ^{13}CO($J = 1 \rightarrow 0$) from the CARMA STING

The ^{12}CO($J = 1 \rightarrow 0$) and ^{13}CO($J = 1 \rightarrow 0$) data used in this study are from the CARMA STING survey. Full details of the survey, data reduction, and masking techniques are presented in Cao et al. (2017). The spectra resolution is 10 km s^{-1}. The FWHM beam sizes for NGC

4254 and NGC 5713 are $3.3'' \times 2.7''$ and $5.1'' \times 4.6''$. We convolved the ^{12}CO($J = 1 \rightarrow 0$) and ^{13}CO($J = 1 \rightarrow 0$) cubes to match the resolution of ^{12}CO($J = 2 \rightarrow 1$).

Table 4.1. Observation Summary

Galaxy	$\theta_{\rm maj} \times \theta_{\rm min}$ [a] ($'' \times ''$)	RMS (mJy beam^{-1})	ΔV [b] (km s^{-1})	$F(^{12}$CO(2-1)) [c] (Jy km s^{-1})	$\frac{F(2-1)}{F(1-0)}$ [d]	$\langle r_{21} \rangle$ [e]
NGC4254	5.40×4.73	25.7	5	1924.95 ± 7.17	0.21	0.26 ± 0.09
NGC5713	7.19×4.51	27.2	5	1185.01 ± 8.14	0.48	0.35 ± 0.16

[a] FWHM of the major and minor axes of the common Gaussian beam of ^{12}CO($J = 2 \rightarrow 1$) cubes.

[b] Channel width of the observation.

[c] Total flux of ^{12}CO($J = 2 \rightarrow 1$) from Figure 4.1, using smoothed ^{12}CO($J = 1 \rightarrow 0$)mask.

[d] Total flux ratio of ^{12}CO($J = 2 \rightarrow 1$) to ^{12}CO($J = 1 \rightarrow 0$).

[e] Mean and standard deviation of intensity ratio of ^{12}CO($J = 2 \rightarrow 1$) to ^{12}CO($J = 1 \rightarrow 0$) obtained from Figure 4.2

4.3 Results

4.3.1 Maps of ^{12}CO($J = 2 \rightarrow 1$) and ^{12}CO($J = 2 \rightarrow 1$)/ ^{12}CO($J = 1 \rightarrow 0$)

We generate ^{12}CO($J = 1 \rightarrow 0$) masks in the same manner as Cao et al. (2017). The ^{12}CO($J = 1 \rightarrow 0$) cubes are firstly smoothed to a spatial resolution twice as large as the original cubes. Pixels with S/N$>$ 4 in two adjacent channels are then selected as the core mask. Finally, the core masks are expanded to include neighboring pixels with S/N$>$ 3. The same ^{12}CO($J = 1 \rightarrow 0$) mask are used to generate all the intensity maps for each galaxy. Figure 4.1 shows the ^{12}CO($J = 2 \rightarrow 1$) integrated intensity maps for NGC 4254 and NGC 5713.

Figure 4.2 presents the resolved r_{21} maps derived from the ^{12}CO($J = 1 \rightarrow 0$) and ^{12}CO($J = 2 \rightarrow 1$) maps. The uncertainties of r_{21} are calculated by error propagation. We cut the maps with a threshold of 3σ. The typical r_{21} in NGC 4254 is smaller than in NGC 5713. In addition, NGC 5713 shows more variations of r_{21} than NGC 4254. In NGC 4254, higher r_{21} are usually found in regions where ^{12}CO($J = 1 \rightarrow 0$) (shown as black contours) is also strong. However, the peaks of r_{21} shift away from the peaks of ^{12}CO($J = 1 \rightarrow 0$) in NGC 5713; r_{21} are distributed asymmetrically and

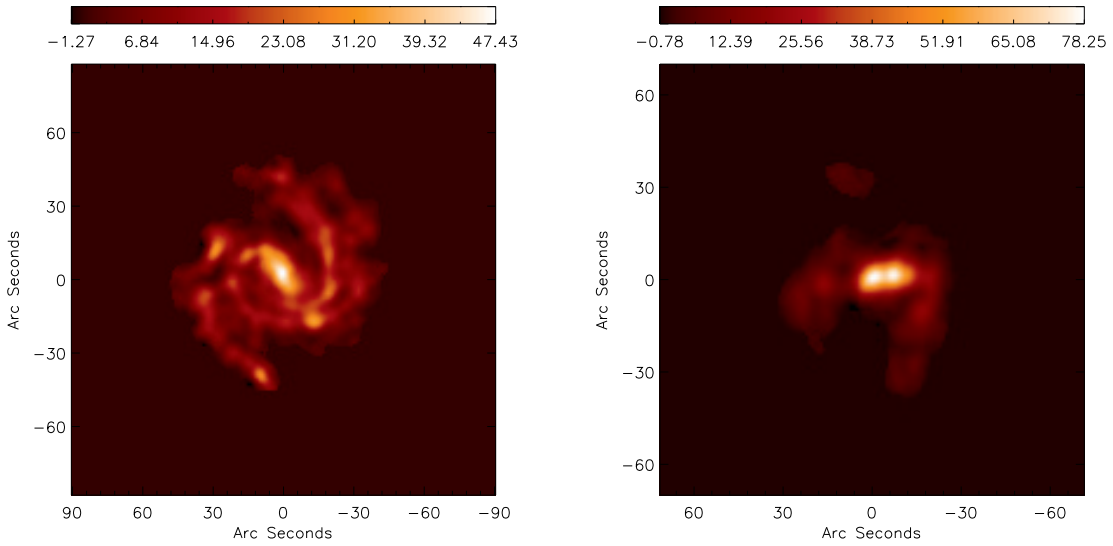

Figure 4.1. ^{12}CO($J = 2 \rightarrow 1$) integrated intensity maps of NGC 4254 and NGC 5713 observed by CARMA. Maps of the ^{12}CO($J = 2 \rightarrow 1$) are derived using the smoothed ^{12}CO($J = 1 \rightarrow 0$)mask.

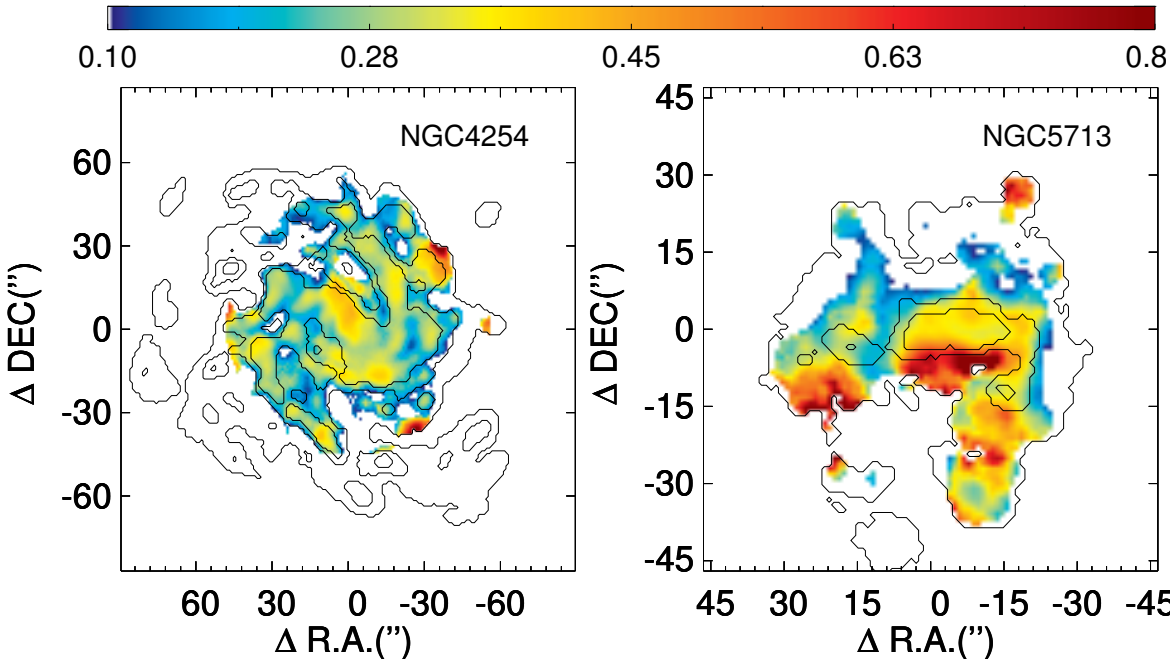

Figure 4.2. Maps of the ^{12}CO($J = 2 \rightarrow 1$) to ^{13}CO($J = 1 \rightarrow 0$) intensity ratio (r_{21}), derived from ^{12}CO($J = 2 \rightarrow 1$) and ^{13}CO($J = 1 \rightarrow 0$) maps using the smoothed ^{12}CO($J = 1 \rightarrow 0$) mask. Black contours show ^{12}CO($J = 1 \rightarrow 0$) intensity with contour levels of $[3, 21, 39]$ times the ^{12}CO($J = 1 \rightarrow 0$)$\sigma_{\rm rms}$.

increase from the North to the South.

We also calculate total fluxes of ^{12}CO($J = 1 \rightarrow 0$) and ^{12}CO($J = 2 \rightarrow 1$) to obtain the flux ratios. The flux ratios and mean values of resolved r_{21} are listed in Table 4.1. In both of

the galaxies, the flux ratios are slightly smaller than the mean values of the resolved $r_{21}(\langle r_{21}\rangle)$, implying that the r_{21} is smaller in places where one or both lines fall below the detection threshold.

4.3.2 Non-LTE analysis of multiple lines

When additional spectral lines other than ^{12}CO($J = 1 \rightarrow 0$) and ^{13}CO($J = 1 \rightarrow 0$) are also available, more constraints on physical conditions can be obtained from non-LTE radiative transfer analysis. One popular method of modeling multiple CO lines is the Large Velocity Gradient (LVG) method (Goldreich & Kwan, 1974). The LVG method assumes that the molecular cloud has a large velocity gradient compared to the local velocity variations. The line emission in a certain region only affects the local region due to the differences in velocity between adjacent regions.

For multi-line studies of NGC 4254 and 5713, we use the radiative transfer code RADEX (van der Tak et al., 2007) for the LVG modeling. RADEX is a program that calculates line intensities from a uniform medium through statistical equilibrium. The radiative transfer is simplified by using a geometrically averaged escaped probability (β) that only depends on the local optical depth. For an expanding spherical shell under the LVG approximation, $\beta = (1 - e^{-\tau})/\tau$ is used in the code. Given kinetic temperature, molecular hydrogen volume density, column density of the molecule and line width, RADEX calculates the intensity of a molecular line.

With measured line ratios of ^{12}CO(2−1)/ ^{12}CO($J = 1 \rightarrow 0$) and ^{12}CO(1−0)/ ^{13}CO($J = 1 \rightarrow 0$), we run a series of RADEX programs to estimate physical conditions in the molecular gas. In the models, we adopt a constant ^{13}CO abundance $[^{13}\mathrm{CO}/\mathrm{H_2}] = 8.5 \times 10^{-5}$, and the velocity gradient is set to $dV/dr = 3$ km s^{-1}. We choose a typical line width $\delta V = 20$ km s^{-1}. ^{12}CO and ^{13}CO at all levels are modeled on grids of the kinetic temperature (T_{kin}) and volume density of molecular gas ($n_{\mathrm{H_2}}$). For ^{13}CO lines, we also run RADEX with various fractional abundances [^{13}CO/^{12}CO].

4.3.2.1 Constraints from total flux ratios

In Figure 4.3, we show the results with [^{12}CO/^{13}CO] = 40 and [^{12}CO/^{13}CO] = 80 for NGC 4254 and NGC 5713. The flux ratios from Table 4.1 are used to constrain the solutions in the parameter space. If [^{12}CO/^{13}CO] is normal $\sim$ 40 in both the galaxies, T_{kin} in NGC 5713 is higher than in NGC 4254. The molecular gas in NGC 5713 is also slightly less dense than in NGC 4254. The

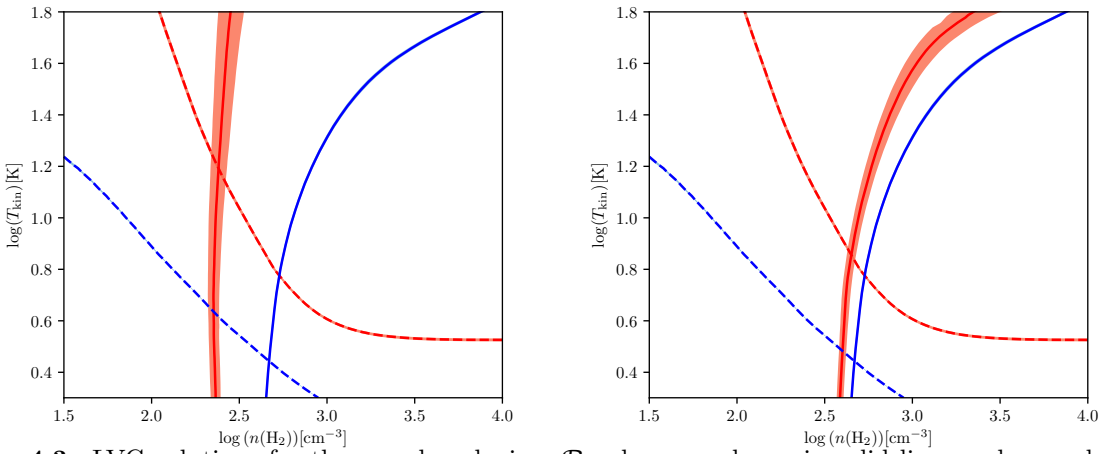

Figure 4.3. LVG solutions for the sample galaxies. $\mathcal{R}$ values are shown in solid lines and r_{21} values are dashed lines; the boundaries of shaded regions show the measurement uncertainty of $\mathcal{R}$. The cross of the solid line and dashed line represents solution space of the galaxy. Blue lines show solution for NGC 4254 and red lines show NGC 5713. Left: solutions for both NGC 4254 and NGC 5713 are calculated from LVG model assuming $[^{12}\mathrm{CO}/^{13}\mathrm{CO}] = 40$. Right: the solution for NGC 4254 is the same as the left panel, assuming $[^{12}\mathrm{CO}/^{13}\mathrm{CO}] = 40$, while the solution for NGC 5713 calculated with a boosted $[^{12}\mathrm{CO}/^{13}\mathrm{CO}] = 80$.

higher $\mathcal{R}$ in NGC 5713 is therefore mainly due to the reduced opacity of $^{12}\mathrm{CO}(J = 1 \rightarrow 0)$ in the warmer, less dense gas. On the other hand, the differences of $\mathcal{R}$ in these two galaxies can be explained by the variations in $[^{12}\mathrm{CO}/^{13}\mathrm{CO}]$. The right panel of Figure 4.3 shows that with a higher $[^{12}\mathrm{CO}/^{13}\mathrm{CO}] = 80$ assumed in NGC 5713, the molecular gas density is similar to NGC 4254.

4.3.2.2 Constraints from resolved line ratios

We compare the physical conditions in the center of the galaxies with the conditions in the outer disks. We select the pixels within 1 kpc and use the mean values of resolved $\mathcal{R}$ and r_{21} of these pixels to constrain the gas properties in the central region. In the outer regions with $r > R_{25}$, not all the pixels with detected $^{12}\mathrm{CO}(J = 1 \rightarrow 0)$ are also detected with $^{13}\mathrm{CO}(J = 1 \rightarrow 0)$ and $^{12}\mathrm{CO}(J = 2 \rightarrow 1)$ lines; the resolved $\mathcal{R}$ and r_{21} are thus biased samples of the line ratios at large radii. We therefore use stacked spectra of $^{13}\mathrm{CO}(J = 1 \rightarrow 0)$, $^{12}\mathrm{CO}(J = 2 \rightarrow 1)$and $^{12}\mathrm{CO}(J = 1 \rightarrow 0)$ to determine the averaged line ratios in outer disk regions. $^{12}\mathrm{CO}(J = 1 \rightarrow 0)$ masks are applied to the resolved spectra. The three masked spectra of each pixel with $^{12}\mathrm{CO}(J = 1 \rightarrow 0)$ detected are then shifted to the rest frame using weighted mean velocity (moment 1) from $^{12}\mathrm{CO}(J = 1 \rightarrow 0)$. In both NGC 4254 and NGC 5713, the stacked $\mathcal{R}$ are higher in the outer disks, while the stacked r_{21} at larger radii are lower than the typical r_{21} in the central 1 kpc of each galaxy. The stacked line ratios are shown in Table 4.2.

Table 4.2. Stacked Line Ratios

Galaxy	r_{21} [a] ($r < 1$kpc)	$\mathcal{R}$[b] ($r < 1$kpc)	r_{21} [c] ($r > 0.2R_{25}$)	$\mathcal{R}$[d] ($r > 0.2R_{25}$)
NGC4254	0.32 ± 0.001	4.85 ± 0.36	0.26 ± 0.001	8.15 ± 0.27
NGC5713	0.42 ± 0.001	14.67 ± 3.56	0.34 ± 0.001	20.43 ± 3.78

[a]Stacked ^{12}CO($J = 2 \rightarrow 1$)/ ^{12}CO($J = 1 \rightarrow 0$) ratio within central 1 kpc.

[b]Stacked ^{12}CO($J = 1 \rightarrow 0$)/ ^{13}CO($J = 1 \rightarrow 0$) ratio within central 1 kpc.

[c]Stacked ^{12}CO($J = 1 \rightarrow 0$)/ ^{13}CO($J = 1 \rightarrow 0$) ratio outside $0.2R_{25}$.

[d]Stacked ^{12}CO($J = 1 \rightarrow 0$)/ ^{13}CO($J = 1 \rightarrow 0$) ratio outside $0.2R_{25}$.

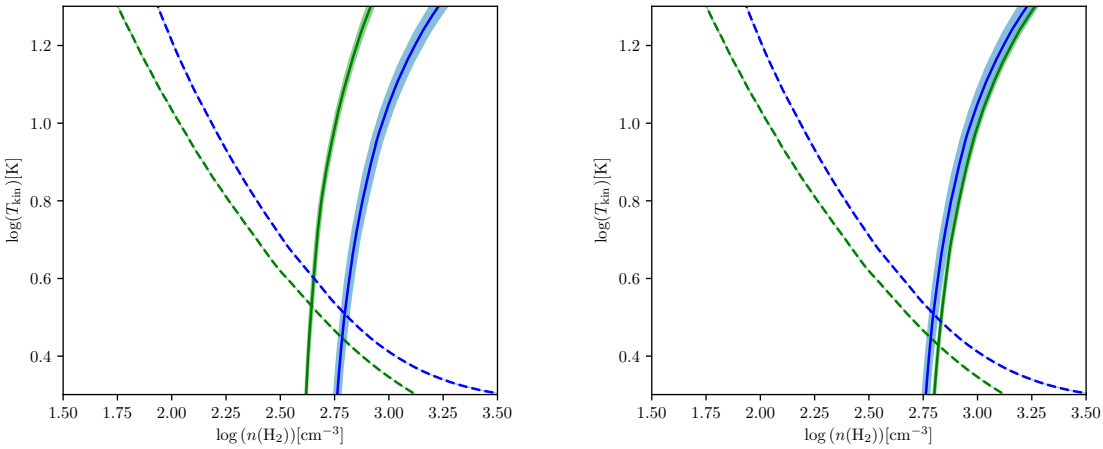

Figure 4.4. LVG solutions for NGC 4254. Stacked $\mathcal{R}$ values are shown in solid lines and r_{21} values are dashed lines. The boundaries of the shaded region show the uncertainty of stacked $\mathcal{R}$. Blue lines show the solution for central 1 kpc, and the green lines show the solution for $r > 0.2R_{25}$. Left panel: [^{12}CO/^{13}CO] = 40 is assumed for both central and disk regions. Right panel: [^{12}CO/^{13}CO] = 40 is used for central region as in the left panel, while a larger [^{12}CO/^{13}CO] = 80 is assumed for disk regions.

Figure 4.4 presents the results from the LVG models of NGC 4254 at different radii. If there is no radial gradient of [^{12}CO/^{13}CO], the gas in the outer disk is more diffuse than the gas in the central regions. Alternatively, without changes in $T_{\rm kin}$ and $n_{\rm H_2}$, increased [^{12}CO/^{13}CO] at $r > 0.2R_{25}$ can also explain the differences in the observed line ratios from the central regions (right panel).

Similar results are also seen in NGC 5713 (Figure 4.5). The volume densities in both central and outer regions of NGC 5713 with [^{12}CO/^{13}CO] = 40 are lower than $\sim$ 300 cm^{-3}; with such lower density, even ^{12}CO($J = 1 \rightarrow 0$) is sub-thermally excited and the emission is expected to be

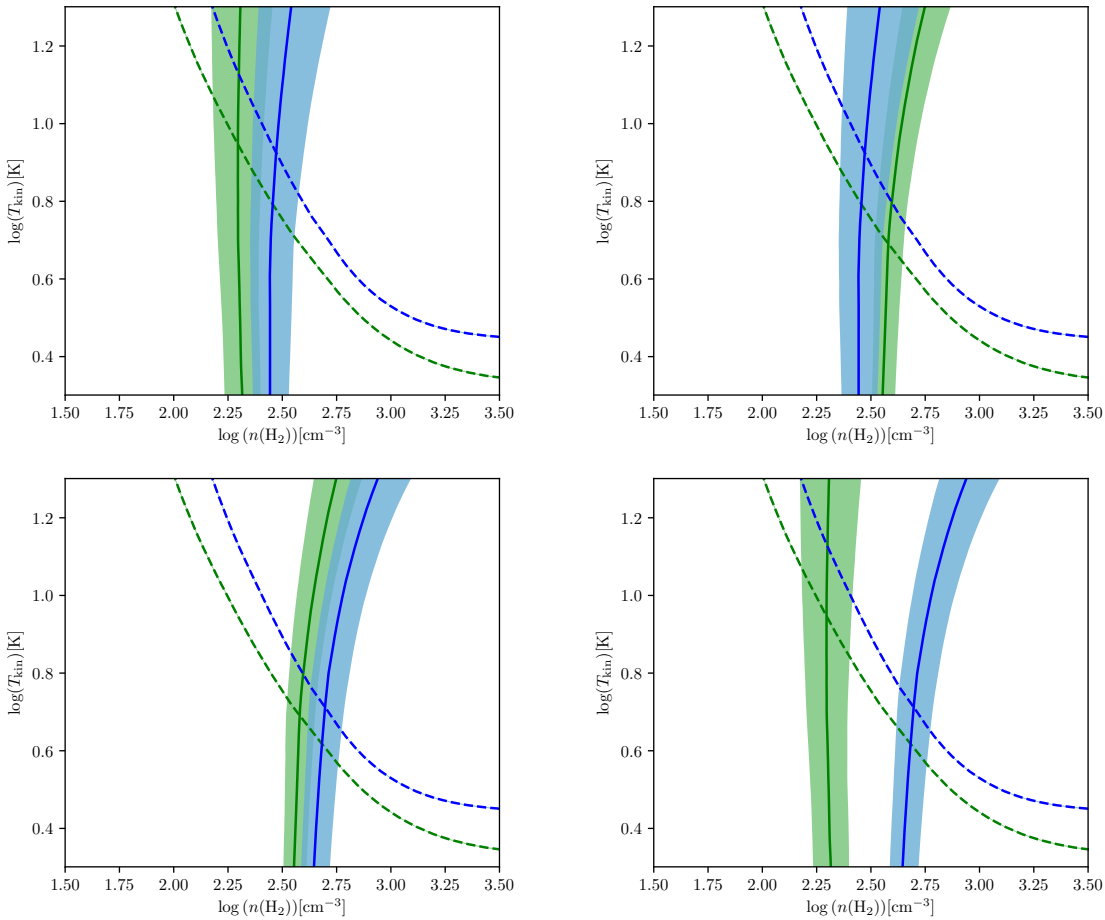

Figure 4.5. LVG solutions for NGC 5713. Stacked $\mathcal{R}$ values are shown in solid lines and r_{21} values are dashed lines. The boundaries of the shaded region show the uncertainty of stacked $\mathcal{R}$. Blue lines show the solution for central 1 kpc, and the green lines show the solution for $r > 0.2R_{25}$. *Top left panel*: [^{12}CO/^{13}CO] = 40 is assumed for both central and outer regions. *Top right panel*: [^{12}CO/^{13}CO] = 40 is used for central region as in the left panel, while a higher [^{12}CO/^{13}CO] = 80 is assumed for outer disk regions. *Bottom left panel*: [^{12}CO/^{13}CO] = 80 is assumed for both central and outer regions. *Top right panel*: [^{12}CO/^{13}CO] = 80 is used for central region as in the left panel, while a lower [^{12}CO/^{13}CO] = 40 is assumed for outer disk regions.

rather weak. However, we observed bright ^{12}CO($J = 1 \rightarrow 0$) in the central regions of NGC 5713, suggesting [^{12}CO/^{13}CO] in the galaxy could be different from the typical assumed abundance of 40.

LVG models for NGC 5713 assuming a higher abundance [^{12}CO/^{13}CO] = 80 are shown in bottom left panel of Figure 4.5. The volume densities resulting from the higher abundance are higher than those resulting from normal abundance [^{12}CO/^{13}CO] = 40. Moreover, due to the redistribution of gas during the interacting process, the radial trend of fractional abundance in NGC 5713 could be the opposite to the increasing trends in normal spiral galaxies like the Milky Way. In such case, the LVG results show that the gas in the outer disk is more diffuse than the solutions assuming no abundance gradients.

4.4 Summary and Future Work

We present ^{12}CO($J = 2 \rightarrow 1$) observations from CARMA in NGC 4254 and NGC 5713. Combining previous observations of ^{12}CO($J = 1 \rightarrow 0$) and ^{13}CO($J = 1 \rightarrow 0$) from the CARMA STING survey with matched resolution, we estimate physical conditions best fitted to the two observed line ratios, $\mathcal{R}$ and r_{21}, using the the radiative transfer code RADEX. We find that both $\mathcal{R}$ and r_{21} are higher in NGC 5713 than in 4254, and the results from the LVG models suggest this is because the molecular gas in NGC 5713 is warmer and less dense, or the fraction abundance [^{12}CO/^{13}CO] is higher. In both galaxies, the averaged r_{21} from spectral stacking is lower in the outer regions than the typical resolved r_{21} in the galaxy center. As the stacked $\mathcal{R}$ values are also elevated in outer regions of these two galaxies, the LVG solutions from the two line ratios suggest that the volume density of molecular gas is lower in outer disks than in the central regions. Moreover, the differences in the physical conditions between central and disk regions are smaller if [^{12}CO/^{13}CO] increases with radius.

Our current results show that the new ^{12}CO($J = 2 \rightarrow 1$) observations are useful to constrain the physical conditions in molecular gas with non-LTE models. We will continue to derive molecular gas properties using resolved r_{21} and $\mathcal{R}$ for regions where both the line ratios are well measured, and investigate how the temperature and volume density of molecular gas are related to star formation activities on kpc scales. In addition, stacked line ratios will be calculated to expand the analysis

to regions where the resolved line ratios are not available. Variations in [^{12}CO/^{13}CO] and velocity dispersion would also be considered in the investigation. This study will help us to understand how molecular gas properties vary across the galaxy generally.

Chapter 5

Conclusions and Future Directions

Observations of ^{13}CO are important for probing physical conditions in molecular ISM where emission is often optically thick. The line intensity ratio $\mathcal{R}$ can be used to trace variations in optical depths determined by physical conditions or chemical processes. Because the emission of ^{13}CO is weaker and more difficult to observe, high resolution interferometric studies of ^{13}CO usually deal with one galaxy each time. Meanwhile, the resolution of single dish extragalactic ^{13}CO surveys is inadequate to capture spatial variations within galaxies. A thorough study of ^{13}CO for a wide variety of nearby galaxies on kpc scales would be an important first step for a systematic study of the molecular gas and its relation to galaxy evolution.

In Chapter 2, we present the first careful systematic study of (sub)kiloparsec-scale ^{13}CO emission in a variety of nearby galaxies. Using 12 galaxies with high-resolution interferometric ^{13}CO($J = 1 \rightarrow 0$) observations from the CARMA STING survey, we investigated the ^{13}CO emission and $\mathcal{R}$ variations within each galaxy and among different galactic systems. Contrary to previous single dish surveys, we find that $\mathcal{R}$ is insensitive to the galactocentric distance or star formation rate on (sub)kiloparsec scales for I_{12} bright regions. We find significant differences in global line ratios among the 11 galaxies. However, there are no strong correlations between $\mathcal{R}$ and global galaxy parameters.

In Chapter 3, we extend the study of resolved $\mathcal{R}$ in 42 galaxies from the EDGE–CALIFA survey. With this larger sample, we still do not find strong dependence of $\mathcal{R}$ on global properties such as morphology, total stellar mass, or galaxy size. The optical spectroscopy data for the EDGE–CALIFA survey with matched resolution enables us to investigate the dependence of $\mathcal{R}$ on the properties of stellar and ionized gas on kpc scales. Our findings show that resolved $\mathcal{R}$ is not very sensitive to the any of the local properties we investigated. We find that roughly half of the galaxies show increased $\mathcal{R}$ beyond $0.25R_{25}$, suggesting more optically thin gas in the disks relative to the

centers. Interacting process tends to elevate $\mathcal{R}$ systemically, and it may also change radial trends of $\mathcal{R}$.

We have seen that sensitivity biases largely hamper interpretation of resolved, low signal-to-noise ^{13}CO observations. The resolved correlations between $\mathcal{R}$ and local environments can only be investigated in the I_{12} bright regions where the sensitivity bias is not dominant. We show that spectral stacking techniques and Monte Carlo simulations could help infer the $\mathcal{R}$ and its relations to other properties for the biased sample including the weak I_{12} regions. Advanced statistical methods taking into account censored data might also be a potential avenue for better investigation of ^{13}CO. Meanwhile, higher sensitivity of ^{13}CO is required to ultimately understand the relations between $\mathcal{R}$ and local properties in nearby galaxies, especially in outer disks where both I_{12} and I_{13} are weak and the less dense gas may be more prevalent given the low stellar mass surface density. Moreover, a synthesized beam on kpc scales includes a number of molecular clouds and the resolved $\mathcal{R}$ is the averaged value over these clouds. Therefore, a comprehensive, unbiased study of resolved $\mathcal{R}$ in nearby galaxies will help link the cloud-scale properties of molecular gas and evolution of entire galaxies on kpc scales and beyond.

Our results from the STING and EDGE surveys suggest that $\mathcal{R}$ on kpc scales are not very sensitive to local environments or the global galaxy properties. We discussed a complex picture of how gas conditions can influence observed line ratios. Additional line ratios are needed for better constraints on gas properties through multi-line diagnostics. An example of a multi-line non-LTE analysis using ^{12}CO and ^{13}CO lines is presented in Chapter 4. The additional ^{12}CO$(2-1)$ line helps better constrain of molecular gas properties using non-LTE radiative models, although there are still large uncertainties due to the unknown chemical abundance. Therefore, direct measurement of ^{12}C/^{13}C abundance is desired to reduce the uncertainties in multi-line studies.

The ^{13}CO observations in nearby galaxies presented in this study would be a starting point of future detailed multi-line studies of physical conditions in molecular gas and their relation to star formation and galaxy evolution. The results in this dissertation suggest a number of follow up observations and future research:

- Higher-J transition lines of ^{12}CO and ^{13}CO may help better constrain molecular gas properties. Applying Large Velocity Gradient (LVG) modeling, these lines will allow us to estimate

the density and temperature on kpc scales across nearby galaxy disks to a large extent. With a well-defined galaxy sample culled from a large survey such as the EDGE-CALIFA survey, we can address the physical conditions in molecular gas and their connections to global galaxy properties on large scales, stellar and ionized components on kiloparsec scales, and star formation activity on all scales. This study will help us understand how large scale properties of galaxies and galactic features (e.g. bars, spiral arms, and bulges) set the density distribution of the molecular gas, and how the gas conditions could be affected by star formation and feedback. A further step will include observing isotopologues of dense gas tracers such as $H^{13}CN$, $H^{13}CO^{+}$, and ^{13}CS. For resolved observations in nearby galaxies, both the dense, star-forming gas and diffuse gas are included in the large beam. Combining these dense gas tracer line ratios with the results from ^{12}CO transitions will give insights into the density structure within a beam. This research will help link the molecular cloud properties and star formation on ~ 50 pc to processes on kpc scales and beyond.

- Single dish ^{12}CO observations and interferometric ^{13}CO measurements with better sensitivity could help locate the the diffuse molecular gas. While the less abundant ^{13}CO may only trace relatively dense molecular gas, ^{12}CO also traces diffuse, unbound gas that is not directly involved in star formation. Therefore, in extragalactic studies, high values of $\mathcal{R}$ can signify regions where the diffuse gas makes a large contribution to the total gas. Our stacking analysis of ^{13}CO in the STING and EDGE surveys suggests that the average density of molecular gas is lower at large radii. However, direct mapping of the diffuse molecular gas on scales of kiloparsecs requires high resolution ^{13}CO images with better brightness sensitivity in the outer disks. Using ALMA to target regions beyond $0.25R_{25}$ with faint ^{12}CO previously detected, the resulting $\mathcal{R}$ maps can be used to accurately locate the diffuse gas, and determine how the diffuse gas relates to the other components of the galaxy. In addition, without short spacing, our interferometric observations cannot identify the presence of extended diffuse gas on large scales. Single-dish ^{12}CO images combined with the existing interferometric data can help identify the diffuse gas distribution on large scales. A better understanding of the extended emission distribution in a large sample of galaxies will also benefit the recovery of total flux for interferometric observations in general.

- Direct measurement of $[^{12}C/^{13}C]$ abundance in nearby galaxies will complement studies using isotopologue observations. In multi-line studies of molecular gas, $[^{12}C/^{13}C]$ has a direct impact on optically thin isotopologues that are required to determine the physical conditions. Moreover, the $[^{12}C/^{13}C]$ ratio is related to the nucleosynthetic history and is therefore important to understanding the chemical evolution of galaxies. $[^{12}C/^{13}C]$ can be measured through $N = 1 \rightarrow 0$ transitions of ^{12}CN and ^{13}CN given high sensitivity, because CN has hyperfine line structure that enables the accurate estimation of opacity effects. The sample to be observed should span a range of stellar mass and metallicity, including both normal isolated and interacting galaxies. These measurements of $[^{12}C/^{13}C]$ could also be used to constrain chemical evolution models and the initial mass function. A better understanding of how $[^{12}C/^{13}C]$ changes with galaxy evolution will also benefit the high redshift ^{13}CO observations. Furthermore, these observations will aid the systematic examination of the molecular properties in different nearby galaxies using LVG models, distinguishing effects of global chemical abundance from the physical conditions of molecular gas on kpc scales.

References

Aalto, S., Beswick, R., & Jütte, E. 2010, A&A, 522, A59

Aalto, S., Booth, R. S., Black, J. H., & Johansson, L. E. B. 1995, A&A, 300, 369

Aalto, S., Johansson, L. E. B., Booth, R. S., & Black, J. H. 1991, A&A, 249, 323

Anderson, J. P., Covarrubias, R. A., James, P. A., Hamuy, M., & Habergham, S. M. 2010, MNRAS, 407, 2660

Bally, J., Stark, A. A., Wilson, R. W., & Henkel, C. 1987, ApJS, 65, 13

Barrera-Ballesteros, J. K., García-Lorenzo, B., Falcón-Barroso, J., et al. 2015, A&A, 582, A21

Bigiel, F., Leroy, A., Walter, F., et al. 2008, AJ, 136, 2846

Blitz, L., Magnani, L., & Mundy, L. 1984, ApJL, 282, L9

Bolatto, A. D., Wolfire, M., & Leroy, A. K. 2013, ARA&A, 51, 207

Bolatto, A. D., Wong, T., Utomo, D., et al. 2017, ApJ, 846, 159

Bryant, P. M., & Scoville, N. Z. 1999, AJ, 117, 2632

Calzetti, D., Wu, S.-Y., Hong, S., et al. 2010, ApJ, 714, 1256

Cao, Y., Wong, T., Xue, R., et al. 2017, ApJ, 847, 33

Cardelli, J. A., Clayton, G. C., & Mathis, J. S. 1989, ApJ, 345, 245

Casoli, F., Dupraz, C., & Combes, F. 1992, A&A, 264, 55

Casoli, F., Dupraz, C., Combes, F., & Kazes, I. 1991, A&A, 251, 1

Catalán-Torrecilla, C., Gil de Paz, A., Castillo-Morales, A., et al. 2015, A&A, 584, A87

Chemin, L., Balkowski, C., Cayatte, V., et al. 2006, MNRAS, 366, 812

Chu, Y.-H., & Watson, W. D. 1983, ApJ, 267, 151

Cid Fernandes, R., Stasińska, G., Mateus, A., & Vale Asari, N. 2011, MNRAS, 413, 1687

Cormier, D., Bigiel, F., Jiménez-Donaire, M. J., et al. 2018, MNRAS, 475, 3909

Crocker, A., Krips, M., Bureau, M., et al. 2012, MNRAS, 421, 1298

Crosthwaite, L. P., & Turner, J. L. 2007, AJ, 134, 1827

Crosthwaite, L. P., Turner, J. L., Buchholz, L., Ho, P. T. P., & Martin, R. N. 2002, AJ, 123, 1892

Daigle, O., Carignan, C., Amram, P., et al. 2006, MNRAS, 367, 469

Danielson, A. L. R., Swinbank, A. M., Smail, I., et al. 2013, MNRAS, 436, 2793

Davies, R. I., Sugai, H., & Ward, M. J. 1997, MNRAS, 291, 314

Davis, T. A. 2014, MNRAS, 445, 2378

de Blok, W. J. G., Walter, F., Brinks, E., et al. 2008, AJ, 136, 2648

Di Teodoro, E. M., & Fraternali, F. 2015, MNRAS, 451, 3021

Dicaire, I., Carignan, C., Amram, P., et al. 2008, MNRAS, 385, 553

Eckart, A., Downes, D., Genzel, R., et al. 1990, ApJ, 348, 434

Engelbracht, C. W., Rieke, G. H., Gordon, K. D., et al. 2008, ApJ, 678, 804

Epinat, B., Amram, P., Marcelin, M., et al. 2008, MNRAS, 388, 500

Evans, A. S., Solomon, P. M., Tacconi, L. J., Vavilkin, T., & Downes, D. 2006, AJ, 132, 2398

Gao, Y., & Solomon, P. M. 2004, ApJ, 606, 271

Goldreich, P., & Kwan, J. 1974, ApJ, 189, 441

Goldsmith, P. F., Heyer, M., Narayanan, G., et al. 2008, ApJ, 680, 428

Haan, S., Schinnerer, E., Emsellem, E., et al. 2009, ApJ, 692, 1623

Hasegawa, T. 1997, in IAU Symposium, Vol. 170, IAU Symposium, ed. W. B. Latter, S. J. E. Radford, P. R. Jewell, J. G. Mangum, & J. Bally, 39

Heikkilä, A., Johansson, L. E. B., & Olofsson, H. 1999, A&A, 344, 817

Henkel, C., & Mauersberger, R. 1993, A&A, 274, 730

Henkel, C., Asiri, H., Ao, Y., et al. 2014, A&A, 565, A3

Hirota, A., Kuno, N., Sato, N., et al. 2010, PASJ, 62, 1261

Hüttemeister, S., Aalto, S., Das, M., & Wall, W. F. 2000, A&A, 363, 93

Kennicutt, R. C., & Evans, N. J. 2012, Annual Review of Astronomy and Astrophysics, 50, 531

Kennicutt, Jr., R. C. 1998, ARA&A, 36, 189

Kewley, L. J., Dopita, M. A., Sutherland, R. S., Heisler, C. A., & Trevena, J. 2001, ApJ, 556, 121

Knapp, G. R., & Bowers, P. F. 1988, ApJ, 331, 974

Koda, J., Scoville, N., Hasegawa, T., et al. 2012, ApJ, 761, 41

König, S., Aalto, S., Muller, S., et al. 2016, A&A, 594, A70

Koopmann, R. A., & Kenney, J. D. P. 2004, ApJ, 613, 866

Leroy, A. K., Walter, F., Brinks, E., et al. 2008, AJ, 136, 2782

Leroy, A. K., Walter, F., Bigiel, F., et al. 2009, AJ, 137, 4670

Leroy, A. K., Walter, F., Sandstrom, K., et al. 2013, AJ, 146, 19

Liszt, H. S., Pety, J., & Lucas, R. 2010, A&A, 518, A45

Makarov, D., Prugniel, P., Terekhova, N., Courtois, H., & Vauglin, I. 2014, A&A, 570, A13

Marino, R. A., Rosales-Ortega, F. F., Sánchez, S. F., et al. 2013, A&A, 559, A114

Martin, C. L., Walsh, W. M., Xiao, K., et al. 2004, ApJS, 150, 239

Meier, D. S., & Turner, J. L. 2004, AJ, 127, 2069

Milam, S. N., Savage, C., Brewster, M. A., Ziurys, L. M., & Wyckoff, S. 2005, ApJ, 634, 1126

Moustakas, J., Kennicutt, Jr., R. C., Tremonti, C. A., et al. 2010, ApJS, 190, 233

Mühle, S., Klein, U., Wilcots, E. M., & Hüttemeister, S. 2005, AJ, 130, 524

Paglione, T. A. D., Wall, W. F., Young, J. S., et al. 2001, ApJS, 135, 183

Papadopoulos, P. P., van der Werf, P., Xilouris, E., Isaak, K. G., & Gao, Y. 2012, ApJ, 751, 10

Pety, J., Schinnerer, E., Leroy, A. K., et al. 2013, ApJ, 779, 43

Pineda, J. E., Caselli, P., & Goodman, A. A. 2008, ApJ, 679, 481

Polk, K. S., Knapp, G. R., Stark, A. A., & Wilson, R. W. 1988, ApJ, 332, 432

Prantzos, N., Aubert, O., & Audouze, J. 1996, A&A, 309, 760

Prieto, J. L., Stanek, K. Z., & Beacom, J. F. 2008, ApJ, 673, 999

Rahman, N., Bolatto, A. D., Wong, T., et al. 2011, ApJ, 730, 72

Rahman, N., Bolatto, A. D., Xue, R., et al. 2012, ApJ, 745, 183

Rickard, L. J., & Blitz, L. 1985, ApJL, 292, L57

Roman-Duval, J., Heyer, M., Brunt, C. M., et al. 2016, ApJ, 818, 144

Roman-Duval, J., Jackson, J. M., Heyer, M., Rathborne, J., & Simon, R. 2010, ApJ, 723, 492

Romano, D., Matteucci, F., Zhang, Z.-Y., Papadopoulos, P. P., & Ivison, R. J. 2017, MNRAS, 470, 401

Rosa-González, D., Terlevich, E., & Terlevich, R. 2002, MNRAS, 332, 283

Rosolowsky, E., & Blitz, L. 2005, ApJ, 623, 826

Sage, L. J., & Isbell, D. W. 1991, A&A, 247, 320

Sakamoto, S., Handa, T., Sofue, Y., Honma, M., & Sorai, K. 1997a, ApJ, 475, 134

Sakamoto, S., Hasegawa, T., Handa, T., Hayashi, M., & Oka, T. 1997b, ApJ, 486, 276

Sánchez, S. F., Kennicutt, R. C., Gil de Paz, A., et al. 2012, A&A, 538, A8

Sánchez, S. F., García-Benito, R., Zibetti, S., et al. 2016a, A&A, 594, A36

Sánchez, S. F., Pérez, E., Sánchez-Blázquez, P., et al. 2016b, RMxAA, 52, 21

Sánchez-Menguiano, L., Sánchez, S. F., Pérez, I., et al. 2016, A&A, 587, A70

Sanders, D. B., Mazzarella, J. M., Kim, D.-C., Surace, J. A., & Soifer, B. T. 2003, AJ, 126, 1607

Sault, R. J., Teuben, P. J., & Wright, M. C. H. 1995, in Astronomical Society of the Pacific Conference Series, Vol. 77, Astronomical Data Analysis Software and Systems IV, ed. R. A. Shaw, H. E. Payne, & J. J. E. Hayes, 433

Sliwa, K., Wilson, C. D., Matsushita, S., et al. 2017, ApJ, 840, 8

Tan, Q.-H., Gao, Y., Zhang, Z.-Y., & Xia, X.-Y. 2011, Research in Astronomy and Astrophysics, 11, 787

Taniguchi, Y., & Ohyama, Y. 1998, ApJL, 507, L121

Thronson, Jr., H. A., & Shull, J. M., eds. 1990, Astrophysics and Space Science Library, Vol. 161, The interstellar medium in galaxies; Proceedings of the 2nd Teton Conference, Grand Teton National Park, WY, July 3-7, 1989

Tosaki, T., Hasegawa, T., Shioya, Y., Kuno, N., & Matsushita, S. 2002, PASJ, 54, 209

Turner, J. L., & Hurt, R. L. 1992, ApJ, 384, 72

van der Tak, F. F. S., Black, J. H., Schöier, F. L., Jansen, D. J., & van Dishoeck, E. F. 2007, A&A, 468, 627

van Zee, L., Salzer, J. J., Haynes, M. P., O'Donoghue, A. A., & Balonek, T. J. 1998, AJ, 116, 2805

Vila-Vilaro, B., Cepa, J., & Zabludoff, A. 2015, ApJS, 218, 28

Walcher, C. J., Wisotzki, L., Bekeraité, S., et al. 2014, A&A, 569, A1

Watanabe, Y., Sorai, K., Kuno, N., & Habe, A. 2011, MNRAS, 411, 1409

Watson, W. D., Anicich, V. G., & Huntress, Jr., W. T. 1976, ApJL, 205, L165

Wilson, C. D., & Walker, C. E. 1994, ApJ, 432, 148

Wilson, T. L., Rohlfs, K., & Hüttemeister, S. 2009, Tools of Radio Astronomy (Springer-Verlag)

Wolfire, M. G., Hollenbach, D., & McKee, C. F. 2010, ApJ, 716, 1191

Wong, T., & Blitz, L. 2002, ApJ, 569, 157

Wong, T., Xue, R., Bolatto, A. D., et al. 2013, ApJL, 777, L4

Wu, J., Evans, II, N. J., Gao, Y., et al. 2005, ApJL, 635, L173

Young, J. S., & Sanders, D. B. 1986, ApJ, 302, 680

Young, J. S., & Scoville, N. 1982, ApJ, 258, 467

Young, J. S., & Scoville, N. Z. 1984, ApJ, 287, 153